SYNTHESIS AND PROCESSING OF MATERIALS FOR DIRECT THERMAL-TO-ELECTRIC ENERGY CONVERSION AND STORAGE

by

Travis Thompson

A DISSERTATION

Submitted
to Michigan State University
in partial fulfillment of the requirements
for the degree of

Materials Science and Engineering—Doctor of Philosophy

2014

ABSTRACT

SYNTHESIS AND PROCESSING OF MATERIALS FOR DIRECT THERMAL-TO-ELECTRIC ENERGY CONVERSION AND STORAGE

by

Travis Thompson

Currently, fossil fuels are the primary source of energy. Mechanical heat engines convert the chemical potential energy in fossil fuels to useful electrical energy through combustion; a relatively low efficiency process that generates carbon dioxide. This practice has led to a significant increase in carbon dioxide emissions and is contributing to climate change. However, not all heat engines are mechanical. Alternative energy generation technologies to mechanical heat engines are known, yet underutilized. Thermoelectric generators are solid-state devices originally developed by NASA to power deep space spacecraft, which can also convert heat into electricity but without any moving parts. Similar to their mechanical counterparts, any heat source, including the burning of fossil fuels, can be used. However, clean heat sources, such as concentrated solar, can alternatively be used. Since the energy sources for many of the alternative energy technologies is intermittent, including concentrated solar for thermoelectric devices, load matching is difficult or impossible and an energy storage technology is needed in addition to the energy conversion technology. This increases the overall cost and complexity of the systems since two devices are required and represents a significant barrier for mass adoption of an alternative energy technology. However, it is possible to convert heat energy to electrical energy *and* store excess charge for use at a later time when the demand increases, in a single device. One such of a device is a thermogalvanic generator and is the electrochemical analog of electronic thermoelectric devices. Essentially, a thermogalvanic device represents the combination of thermoelectric and galvanic systems. As such, the rich history of strategies developed by both the thermoelectric community to better the performance of thermoelectric devices and by the electrochemical community to better traditional galvanic devices (i.e. batteries) can be applied to thermogalvanic devices. Although thermogal-

vanic devices are known, there has been little exploration into the use of thermogalvanic devices for power generation and energy storage.

First, this work formalizes the energy problem and introduces the operating principles of thermoelectric, galvanic, and thermogalvanic devices. Second, oxide based thermoelectric materials are explored from a synthetic and processing standpoint. Out of necessity, a new synthetic technique was invented and a novel hot-press technique was developed. Third, a solid Li-ion conducting electrolyte, based on the garnet crystal structure, is identified for the use in a thermogalvanic cell. In order to better understand the conductivity behavior, an in-depth exploration into the variables that control the ionic transport is performed on the electrolyte. Third, a thermogalvanic cell is constructed using this garnet based Li-ion conducting solid electrolyte and the first demonstration of such a cell is presented. Finally, strategies to improve the performance of thermogalvanic cells based on garnet type solid electrolytes are outlined for future work.

The purpose of this work is to use an interdisciplinary approach to marry together the electrochemistry of galvanic systems with the strategies used to better semiconductor based thermoelectric materials and ceramics processing techniques to fabricate these systems. This dissertation will explore the interplay of these areas.

I dedicate this dissertation to all those who like to argue, to discuss, and give a part of themself to follow their passions. To those that are passionate, so that they might look into the past and find ideas that have lain forgotten, worth exploring.

ACKNOWLEDGMENTS

I would like to thank the present and past members of Dr. Jeff Sakamoto's group, including Ryan Maloney, Ezhiyl Rangasamy, Dan Lynam, and others, who always provided great moments both in and outside the laboratory. I especially would like to thank Tom Heuser, who assisted me for several years as an undergraduate student. Without Tom, only a small fraction of this work would have been possible. It is obvious to me that Tom will do great things and I am glad to have had him been apart of my journey as much as I hope I have been apart of his.

I would also like to thank the people outside of our group including Gloria Lehr, Steve Boona, Winston Carr, Per Askland, and others, who helped me collect data, intrept results, and engage in discussion.

I am grateful for my parents, Kim and Kirk Thompson, who instilled a strong work ethic and high confidence in my abilities. I strongly believe that I am the person I am today because of them.

I am appreciative for all our collaborators: Jeff Wolfenstine and Jan L. Allen at the Army Research Labs, Michelle Johannes at the Naval Research Labs, Nancy Dudney at Oak Ridge National Lab, Ashfia Huq at the Spallation Neutron Source, and others elsewhere. I feel that their thoughts and input on our work together have helped me to grow as a researcher and member of the community. Truly, collaboration, and not competition, is the driver of change and much more is possible when people work together.

I'd like to acknowledge the funding for this research from the DOE Office of Science, Basic Energy Sciences, Energy Frontier Research Centers (EFRC) Program Revolutionary Materials for Solid State Energy Conversion (RMSSEC). This EFRC, again, represented the essence of scientific collaboration.

Finally, I would like to thank my advisor, Dr. Jeff Sakamoto, who helped me to grow into the researcher I always wanted to be and accomplish more then I thought I could. Jeff gave me a strong, stable base and independence, from which I was able to truly flourish. His ability to foster an environment which enables growth in his students is truly amazing. I look forward to being a part of the research community with him and our continued interaction throughout my career.

TABLE OF CONTENTS

LIST OF TABLES

LIST OF FIGURES

CHAPTER 1

AIMS AND OBJECTIVES

This dissertation discusses materials synthesis and processing of materials for direct thermal-to-electric energy conversion and storage including thermoelectric materials, solid Li-ion conducting electrolytes, and thermogalvanic materials. The half century old concept of thermogalvanic systems, which can directly convert thermal energy to electrical energy and store this energy when not needed, is reintroduced and explored. Essentially, these devices can perform the operation of a thermoelectric generator and a battery in a single, solid-state device. Recent research advances from both the thermoelectric and battery communities are applicable to these systems. Since the construction of such a device involves complex, multi-cationic ceramic solids, new synthesis and consolidation techniques have been developed. As such, the purpose of this work was to:

> use an interdisciplinary approach to marry together the electrochemistry of galvanic systems with the strategies used to better semiconductor based thermoelectric materials and ceramics processing techniques to fabricate these systems.

1.1 Background and Introduction

Chapter 2 will introduce background information and the problem being addressed. The concepts and operating principles of mechanical heat engines, direct thermal-to-electric energy converters,

faradaic electrochemical energy storage, and thermogalvanic systems are discussed. The concept of a solid-state dual purpose thermal-to-electric energy conversion and storage device is introduced.

1.2 Experimental Methodology

Chapter 3 will detail the experimental methodology and metrology used to characterize the materials presented in this dissertation. Since no procedure is established in the literature for the measurement of thermogalvanic properties, an emphasis is placed on the explanation of cell assembly for thermogalvanic materials properties measurements.

1.3 Oxide Thermoelectric Materials

Chapter 4 will discuss thermoelectric systems based on alkali and alkaline earth cobalt oxide materials. The challenges associated with synthesizing these phases and consolidating the powder into dense compacts for thermoelectric materials characterization initiated the invention of a new synthetic technique and the development of a novel hot-pressing method. These techniques enabled the materials studies discussed throughout this dissertation.

1.4 Garnet Based Li-Ion conducting Solid Electrolytes

Chapter 5 will discuss the recently discovered Zirconium based stuffed garnet as a Li - ion conducting solid electrolyte. A detailed materials characterization study was conducted to correlate phase stability with formulation and the atomic structure with ionic conductivity. Parallels will be

drawn between the garnet like solid electrolyte and AgI, the archetypal superionic conductor. This work will demonstrate that the carrier concentration in cationic conductors is not well defined and presents evidence so that the community can begin a conversation on properly defining the carrier concentration.

1.5 Thermogalvanic Operation of a Solid-State Cell with a Garnet Electrolyte

Chapter 6 will evaluate the feasibility of using zirconium based garnet materials as a thermogalvanic solid electrolyte. A thermogalvanic cell based garnet solid electrolyte and Li metal electrodes was fabricated to demonstrate proof of concept of thermogalvanic operation employing an all solid-state energy conversion and energy storage technology in one device.

1.6 Conclusions and Future Work

Chapter 7 will summarize the work presented in this dissertation and offer directions for future explorations of garnet based solid electrolytes for thermogalvanic operation. The goal of this work was to develop a novel solid-state dual-purpose energy conversion and energy storage device.

CHAPTER 2

BACKGROUND AND INTRODUCTION

Over the course of the past decade it has become evident that the Earth's climate is changing as manifested by globally increasing temperatures. Several reports have predicted severe negative consequences for unmitigated climate change scenarios (Figure 2.1) [1–10]. The change in the climate is primarily being driven by the increase in carbon dioxide gas (CO_2) levels (Figure 2.2) [1, 2, 10].

It is difficult to unequivocally prove that anthropomorphic activity is solely responsible for the increase in CO_2 levels. Certainly human activity is at least partially contributing to the increase in CO_2 levels. As such, any and all efforts to reduce CO_2 emission would only be beneficial. Although energy rich hydrocarbon based sources (so called fossil fuels such as oil and coal) are still abundant there are many issues associated with the extraction of these energy sources and the conversion to electrical energy. Thus, they are not sustainable. Sustainable energy sources have been identified and devices to convert these energy sources to electrical energy are being developed. However, the amount of energy currently produced from alternative energy sources is relatively small.

Figure 2.3 is an energy tributary diagram for the United States in 2013 produced by the Lawrence Livermore National Laboratory. Figure 2.3 quantifies the amount of energy used from each source and shows how it flows through the energy landscape to final end uses. It can be seen

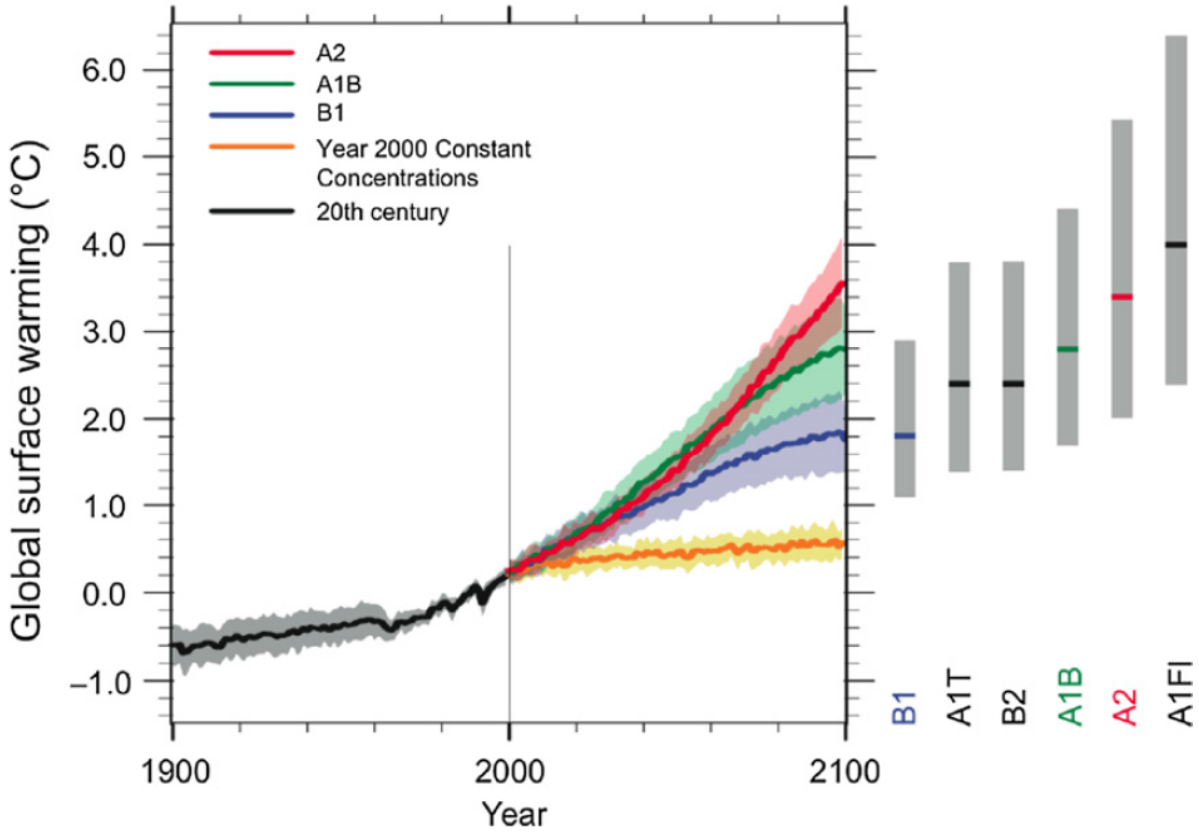

Figure 2.1: Projections of the temperature rise in the 21st century. The various curves shown are different models used to make the predictions [1].

from Figure 2.3 (left most column) that approximately 80 percent of the energy used was generated from unsustainable, hydrocarbon based energy sources (petroleum, coal, and natural gas), 8 percent from nuclear, and the remaining 12 percent from sustainable alternative energy sources such as solar, hydroelectric, and wind. Figure 2.3 (right most column) also shows that regardless of the end use, approx. 60 percent of the energy used was rejected. That is to say that no useful work was performed by 60 percent of the energy that was used.

If climate change is a known problem, and a solution to address that problem has been identified (i.e. the reduction of CO_2 emissions), then why has the practice of burning hydrocarbon fuels (and

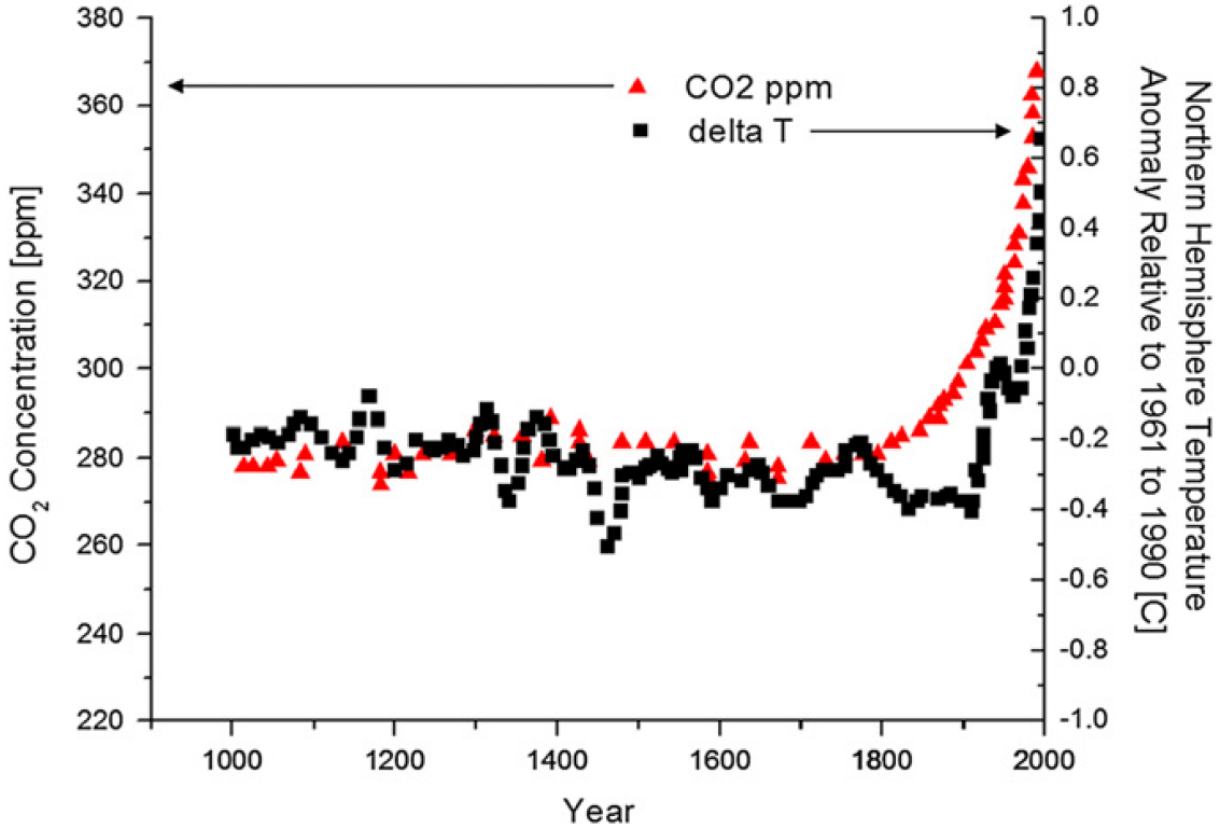

Figure 2.2: The rise in atmospheric carbon dioxide concentration and Northern Hemispheric temperature over the past 1000 years [1].

thus emitting CO_2 gas) continued? The answer must be that the burning of hydrocarbon fuels has some utility such that the opportunity cost of ending this practice is too great. Thus, in order to understand how to transition away from the use of hydrocarbon fuels, it must first be understood how they have been useful for humanity. Once this baseline is established, it can be used as a benchmark for alternative technologies.

Hydrocarbon fuels are primarily utilized in heat engines. Heat engines, powered by hydrocarbon fuels, enabled the industrial revolution and continue to be the backbone of modern society. The more then 150 years of experience that humanity has with heat engines is responsible for the

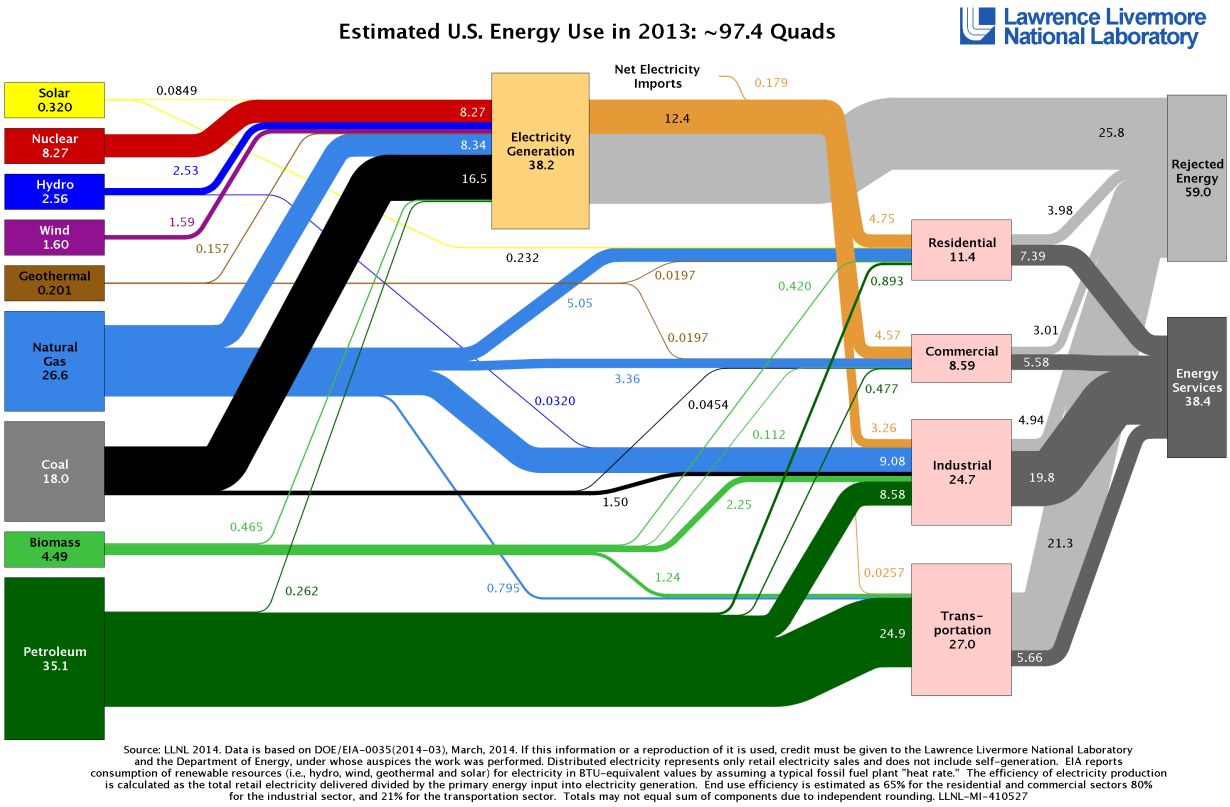

Figure 2.3: An energy tributary diagram for the United States in 2013 produced by the Lawrence Livermore National Laboratory.

resistance in moving away these technologies. Thus, in order to understand the benefits of hydrocarbon fuels, heat engines will be briefly discussed. The discussion of heat engines will also be beneficial for future sections in this report since some alternative energy conversion and storage devices (such as thermoelectric and thermogalvanic devices) are heat engines.

2.1 Heat engines

A heat engine is defined as:

> "a device that attempts to mimic thermodynamic cycles to convert heat to work" [11]

A thermodynamic cycle is made of linked thermodynamic processes that involve the transfer of heat and work in and out of a system. This is made possible because state variables, such as temperature, pressure and entropy are varied for a working substance. The substance is most often, though not exclusively, a fluid and a change in phase can be involved. The cycle is completed by the system returning to the initial state. Thus, the whole process (cycle) can be repeated. If in the process of performing the cycle, the device converts heat from a source to work and then disposes of the remaining heat to a sink, then the device is acting as a heat engine. Conversely, work can be used to move heat from a source to a sink, thus acting as a heat pump. Although heat pumps are intimately related to heat engines, they are beyond the scope of this work and are only included for completeness.

In 1824, Sadi Carnot advanced the field of thermodynamics by proposing what would become known as Carnot's principle [12]. The principle consists of the following propositions:

1. No engine can be more efficient than a reversible engine operating between the same high temperature and low temperature reservoirs. Here the term heat reservoir is taken to mean either a heat source or a heat sink.

2. The efficiencies of all reversible engines operating between the same constant temperature reservoirs are the same.

3. The efficiency of a reversible engine depends only upon the temperatures of the heat source and heat receiver.

The implication of Carnot's principle is the efficiency of the conversion of heat to work for all heat engines has an upper bound, determined by the difference in temperature between the heat reservoirs. This efficiency is known as the Carnot efficiency and is defined as:

$$\eta_{Carnot} = 1 - \frac{T_{cold}}{T_{hot}} \tag{2.1}$$

Although the Carnot efficiency represents the upper bound, real devices cannot achieve this level of efficiency. This is reflected in Figure 2.3 by the approx. 60 percent rejected energy that does not perform useful work mentioned previously. For example, The Otto cycle which is utilized by automobiles offers a 20 - 30 percent efficiency in converting the chemical energy stored in gasoline into mechanical work to propel the vehicle forward. The remaining 70 - 80 percent of the chemical energy is lost, primarily in the form of heat, to the environment.

Thus heat engines convert heat into work. This work can be used to turn a turbine and create electricity. The heat input for a heat engine conventionally comes from the combustion of a hydrocarbon fuel. Therefore, the overall energy transformation process can be schematically represented as: Chemical energy in fuel is used to generate heat energy –> this heat energy is then used in a heat engine and is converted to mechanical energy –> this mechanical energy is converted to electrical energy by a generator, such as a turbine. Therefore, a heat engine, when paired with an electrical generator, only converts energy from one type to another: chemical to heat to mechanical to electrical. No energy is stored in this process. As such, the energy must be used as it is created. This is problematic when the load, for example the electrical grid, is variable as is indeed the case.

However, since the heat generated to power the heat engine is often from the burning of a fuel, as the demand (i.e. load) is reduced, the amount of fuel fed into the engine can be proportionally reduced. This is known as load matching and is the primary advantage of a heat engine. The inability of alternative energy technologies to load match is a significant barrier preventing mass adoption. For example, at night, photovoltaics cannot generate electricity. However, lighting loads are still present. As such, an energy storage system in addition to the energy conversion technology is needed for load matching. Since an energy storage system is needed in addition to the alternative energy technologies, these combination systems are more expensive and complex.

Utilization of sustainable energy sources requires new enabling technologies. Heat is ubiquitous and new advanced direct energy conversion *and* storage devices which can utilize heat to perform work must be developed. Since these systems are not mechanical in nature, advances will be driven by fundamental materials exploration. However, even with the successful development of a direct energy converter and storage system, two devices will still be required. What if a single device existed that performed both functions: something that could directly convert thermal energy to electricity, store excess energy when not needed, and deliver it as needed to a load at a later time? Devices such as this are not only theoretically possible but have been demonstrated as proof of concept and subsequently, seemingly forgotten. Thus thermal-to-electric energy conversion and storage is the goal of this work. Before these types of devices are discussed in depth, more time will be spent discussing direct thermal-to-electric energy converters and storage systems separately as these two approaches (combined and separate generation/storage) are interrelated.

2.2 Direct thermal-to-electric energy conversion and faradaic electrochemical energy storage systems

One of the sustainable means to use solar energy is by direct solar thermal-to-electric energy conversion. Sunlight can be concentrated and the heat generated can be used to perform work. When the thermal energy from the solar spectrum is used, the device is again a heat engine but not a mechanical heat engine as discussed above. Moreover, the heat source does not need to be from the sun. These types of direct thermal-to-electric converters and energy storage systems are discussed more below.

2.2.1 Faradaic electrochemical energy storage

A Faradaic electrochemical energy storage device is one which involves a charge transfer event at the electrodes. Non-Faradic means of storing energy such as capacitors are available, but faradaic devices such as galvanic cells (batteries) offer a better trade-off between power and capacity. A galvanic cell is comprised of three components: a cathode, an anode, and an electrolyte. The cell is constructed such that a chemical driving force exists between the anode and the cathode. The electrolyte selectively allows ions to pass though but blocks the transport of electronic species. Since the electrolyte will not pass electrons,when in the open circuit condition, the electrochemical reaction between the two electrodes (anode and cathode) does occur. An external circuit is needed to allow the electrochemical reaction to occur. Thus, the circuit can be closed, an electrical current will flow, a chemical reaction between the anode and cathode will occur, the cell will discharge,

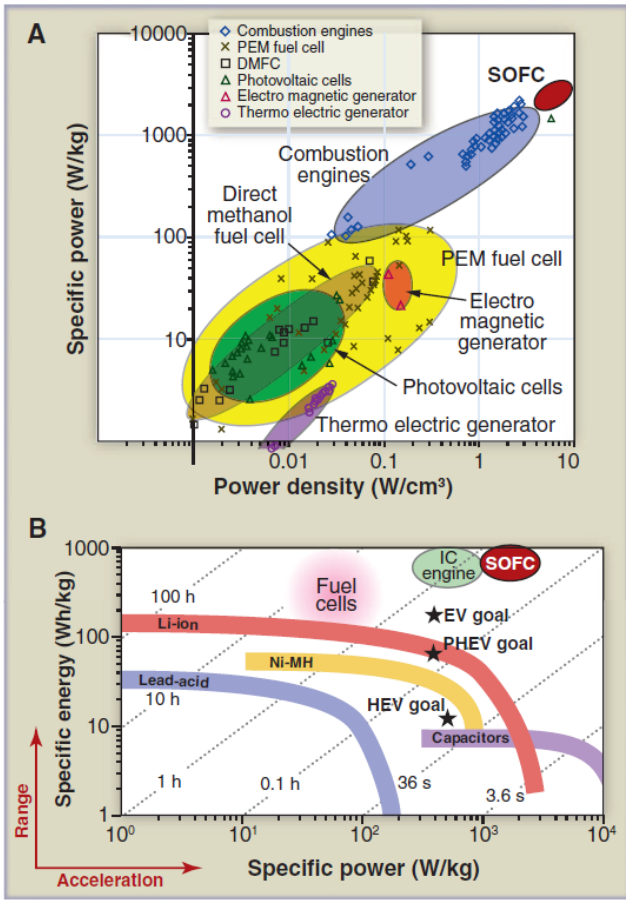

Figure 2.4: A) Comparison of the specific power of various devices as a function of power density and B) Ragone plot for various devices [13].

and work can be performed. If the chemical reaction is reversible, this process can be reversed and the galvanic cell can be recharged. In this manner, charge can be stored for use at a later time. Figure 2.4 compares various faradaic and non-faradaic devices in terms of gravimetric $(\frac{W}{kg})$ and volumetric $(\frac{W}{cm^3})$ power densities (Figure 2.4 A) as well as the specific power $(\frac{W}{kg})$ and the specific energy $(\frac{Whr}{kg})$ [13]. A plot of the specific energy vs the specific power (Figure 2.4 B) is known as a Ragone plot.

Faradaic energy storage systems could provide the means to store excess electrical energy

produced by a heat engine for delivery at later times. It is illustrative to discuss energy storage devices in terms of automobiles because of wide scale adoption and popular familiarity. In the Ragone plot shown in Figure 2.4 B, the energy density represents driving range on a charge while the power density represents acceleration. It can be seen then that fuel cells offer the best in terms of capacity but not power, while capacitors offer the best in terms of power but not capacity. Batteries (galvanic cells) offer a compromise between power and capacity. It could be argued that more advanced fuel cells or ultra-capacitors can offer the same, or better, performance as battery systems but that discussion is beyond the scope of this work.

2.2.2 Direct thermal-to-electric energy conversion

As mentioned above, direct thermal-to-electric energy conversion uses a heat source and converts this thermal energy to electricity and is therefore a heat engine. Thermoelectric materials for power generation are a solid state direct thermal-to-electric energy conversion device that utilizes the Seebeck effect. Thermoelectric devices are attractive because heat sources are ubiquitous. A particularly interesting application is in waste heat recovery from conventional mechanical heat engines such as automobiles. Although not a solution to the problems associated with the use of hydrocarbon fuels, waste heat devices could help reduce their consumption. These devices do not have moving parts like mechanical heat engines but the efficiency is limited by the Carnot efficiency just the same.

The conversion efficiency of these devices is given by:

$$\eta = \eta_{Carnot} \frac{\sqrt{1+zT_{avg}} - 1}{\sqrt{1+zT_{avg}} + \frac{T_{cold}}{T_{hot}}} \tag{2.2}$$

Where η_{Carnot} is the Carnot efficiency, zT is the dimensionless figure of merit, T_{cold} is the cold side temperature, and T_{hot} is the hot side temperature.

The dimensionless figure of merit, zT, is given by:

$$zT = \frac{\alpha^2 \sigma}{\kappa} \tag{2.3}$$

Where α is the thermopower (Seebeck coefficient in the case of thermoelectric materials), σ is the electrical conductivity (electronic in the case of thermoelectric materials) of the material, and κ is the total thermal conductivity from charge carriers and lattice phonons in the material.

Figure 2.5 is a plot of the various thermoelectric materials properties for a simulated Bi_2Te_3 material [14]. Several things can be observed from this figure. First, the materials properties are contraindicative. This means that one property, such as the electronic conductivity, optimizes at the expense of another property, such as the thermal conductivity. Second, because of this contraindicative nature, the zT normally maximizes with a carrier concentration in the range of 10^{19} to 10^{21} carriers per cm^3. This falls into the heavily doped semi-conductor regime. As such, state of the art thermoelectric devices consist of n-type and p-type semiconductor legs connected together electrically in series and thermally in parallel. Because two dissimilar materials are connected together electrically, the thermal gradient along the length of the leg generates a current.

Figure 2.6 is a plot of the zT as a function of temperature for several thermoelectric materials.

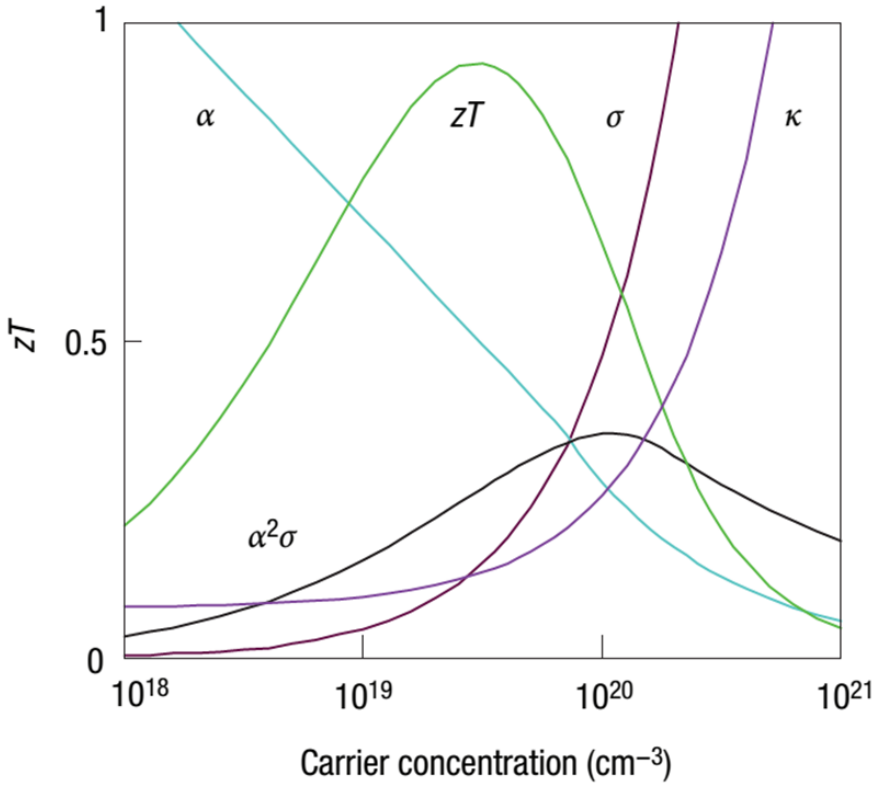

Figure 2.5: Plot showing how the various thermoelectric materials properties vary with the carrier concentration. The data presented is for a simulation of Bi_2Te_3 [14].

Although there is no theoretical limit, zT values of 1 are common for commercial thermoelectric materials and zT values as high as 2 have been reported for bulk materials in the laboratory [16]. There is large body of work in the literature for strategies to improve the figure of merit for thermoelectric materials [17]. Among them are: 1) nanostructuring the microstructure so that phonons can preferentially be scattered over charge carriers, thus decreasing the thermal conductivity without decreasing the electronic conductivity [18], 2) engineering the band structure so that the Seebeck coefficient is increased without changing the carrier concentration [19], and 3) forming solid solutions so that mass fluctuations act as scattering sites for phonons [14].

Indeed, steady progress has been made in improving zT values through the methods mentioned

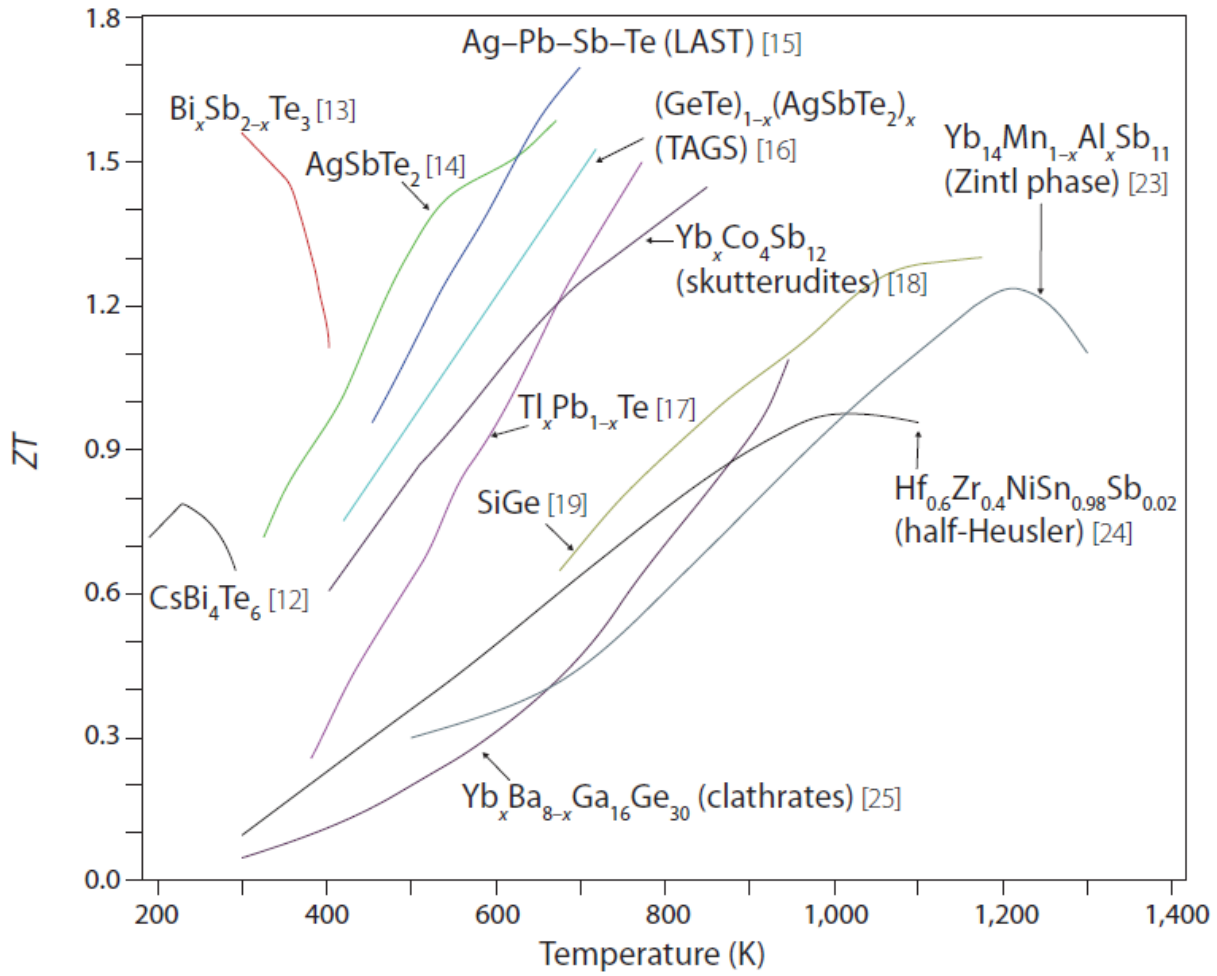

Figure 2.6: Figure of Merit (zT) of various state of the art thermoelectric materials [15]. The citations in the figure correspond to the source from which it was taken and not this work.

above. Recent development of related materials is enabling the development of technologies related to thermoelectric devices. Thermally regenerative electrochemical systems (TRES) are another class of direct thermal-to-electric energy converter that could make use of some of the same strategies used to better thermoelectric materials but operate using electrochemical principles.

2.3 Thermally regenerative electrochemical systems (TRES)

TRES are electrochemical systems which take advantage of thermal energy in electrochemical systems. TRES systems fall into seven broad categories as identified by Osteryoung and Chum from SERI (now NREL) in an extensive review in 1981 [20]. These systems use a thermal gradient to establish a chemical potential gradient between the anode and cathode of the electrochemical cell. The various types of TRES are different ways of actualizing this and a full discussion is considered beyond the scope of this work.

Thermally regenerative electrochemical systems are not a new idea. Alkali Metal Thermal to Electric Converters (AMTECs) are one type of TRES device and are the most mature [21–24]. AMTECs were studied in the 1970's and 1980's at Ford and NASA JPL [25]. In these devices, an alkali metal such as sodium is melted and separated form the vapor phase by an electrolyte. The molten sodium is isothermally expanded through the electrolyte to the vapor form and electrons are forced through an external circuit. The sodium vapor is condensed and then pumped back to the liquid side, thus completing the cycle. Very high efficiencies for this process are possible but there are significant engineering challenges associated with the condensation and pumping of alkali metals which have not been overcome.

Thermogalvanic materials, studied in the 1950's at General Electric [26], are another type of TRES and are the direct electrochemical analog of thermoelectric materials. Just like thermoelectric generators, thermogalvanic generators are a heat engine. Phenomenologically, these devices

can be thought of as using a thermal gradient to pump ions from the hot electrode, through the electrolyte, to the cold electrode while electrons pass through an external circuit. Conventionally, they have the same configuration of a conventional galvanic cell where an inert Pt or Cu anode and cathode are separated by an electrolyte with a redox couple in solution but, unlike a conventional galvanic cell, the thermogalvanic cell is not isothermal. These devices have been mostly explored from the theoretical viewpoint of irreversible thermodynamics [20]. Most experimental investigations have been to measure Soret coefficients so that entropies can be calculated. The Soret effect is the ionic analog of the Seebeck effect where separation of charged ions in an electrolyte can occur due to a thermal gradient [27–29]. As an example, Figure 2.7 is a plot of the Soret coefficient for a series of $AgBr$ samples doped with $CdBr_2$ as a function of temperature.

Ag halide based solid electrolytes including AgI, AgBr and solid solutions were investigated as a part of the original work done at GE [26, 31, 32] . However, little emphasis has been placed on exploring these systems from a power generation point of view [33] and has only begun in the early 1990's for aqueous based electrolyte solutions [34]. Most of the work has focused on finding redox couples in the solution phase with higher thermopowers. More recently, ionic liquids have been investigated as electrolytes for thermogalvanic systems [35, 36]. There has been one report of a gel electrolyte from a theoretical perspective [37].

Since thermogalvanic materials are a direct analog to thermoelectric materials, the same figure of merit is used to evaluate a material. For power generation, the measurement should be performed on a whole cell. However, just as in the thermoelectric community where individual

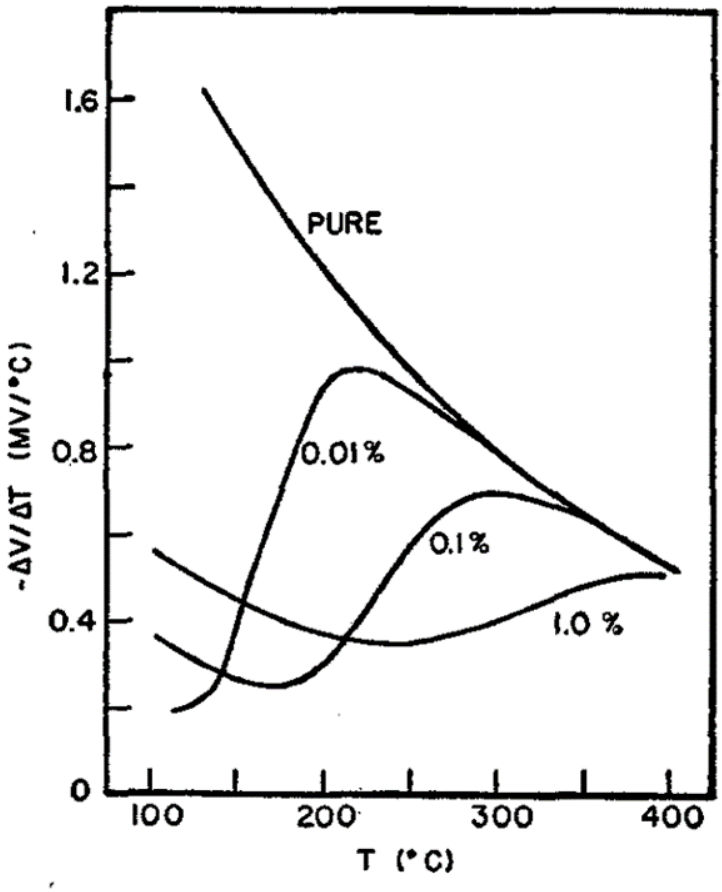

Figure 2.7: Soret coefficient for a series of $AgBr$ samples doped with $CdBr_2$ as a function of temperature [30].

materials for each leg are often evaluated separately, anode, cathode, and electrolyte materials for thermogalvanic applications can be evaluated separately. The dimensionless figure of merit is still represented as zT. Performance of thermogalvanic systems are mostly driven by the electrolyte and the following discussion is held in that context. Instead of Seebeck coefficient, the total thermopower is substituted which can be a combination of Seebeck and Soret effects. The electronic conductivity is replaced by the ionic conductivity. The thermal conductivity for thermogalvanic materials has the same meaning as that for thermoelectric materials.

So far, the description of thermogalvanic systems presented can only offer power generation but not storage. However, galvanic systems, such as Li-ion batteries, can offer charge storage if intercalation electrodes are used instead of inert electrodes such as Pt. The report by Osteryoung and Chum, written in 1981, reviewed work done prior to the development of intercalation electrodes for Li-ion batteries in the early 1990's. If these types of electrodes were used in a thermogalvanic cell, then charge storage as well as power generation is possible. This configuration represents the dual purpose device mentioned previously. Two reports exist in the literature where Li_xTiS_2 intercalation electrodes were used in liquid electrolyte based cells [33, 38]. In one of those reports, charge/discharge cycles were report by the application and removal of a thermal gradient to a symmetric cell [38] . No reports in the literature could be found where two different intercalation electrodes were used or where a solid electrolyte was used with an intercalation electrode.

2.3.1 Solid-state Thermogalvanic systems

Thermogalvanic systems for energy generation and charge storage have been demonstrated but relatively little work has been done from this context. Electrolytes for these systems seem to be the most important component and most of the work has been exploring liquid aqueous electrolytes. However, from a thermoelectric standpoint, there are some fundamental issues associated with the use of a liquid electrolyte in a thermogalvanic cell.

First, since the electrolyte is liquid, the thermal gradient which can be established between the two electrodes will be limited due to convective heat transfer. The investigations with ionic

liquids mentioned previously might lead to higher a thermopower but since the systems is still a liquid, the convective heat transfer mode will still be present. Second, the net ionic conductivity is impacted by the transference number of the liquid systems because of the counter flow of anions. This is also true for isothermal galvanic cells. Third, the boiling point of the liquid limits the operating temperature. Replacing the liquid electrolyte with a solid electrolyte could address all of these issues. Figure 2.8 is a schematic showing the proposed solid-state thermogalvanic power generation cycle. The thermogalvanic cell is first non-isothermally charged (A). Next, charge can be stored in the cathode for use at a later time for load matching (B). Finally, the thermogalvanic cell can be discharged similarly to a traditional galvanic cell (C). In contrast to a galvanic cell, since thermal energy is used during charging, electrical work can be performed during both charging *and* discharging.

All solid thermogalvanic systems with solid electrolytes have been investigated by GE in the 1950's [26]. There, cells consisting of Ag/AgI/Ag were constructed but were limited by silver dendrite growth through the solid electrolyte from the hot anode. Even when a porous alumina disk was impregnated with AgI, the dendrite growth was slowed but not eliminated.

What seems to be missing the most from the thermogalvanic research investigations thus far is perspective from thermoelectricians. Thermogalvanic systems, by their nature, are multidisciplinary. So far, the investigations have been: 1) from a theoretical perspective and 2) from a traditional electrochemical perspective. Thermogalvanic systems seem to have real promise but there needs to be more investigation done from a materials science and thermoelectric perspective.

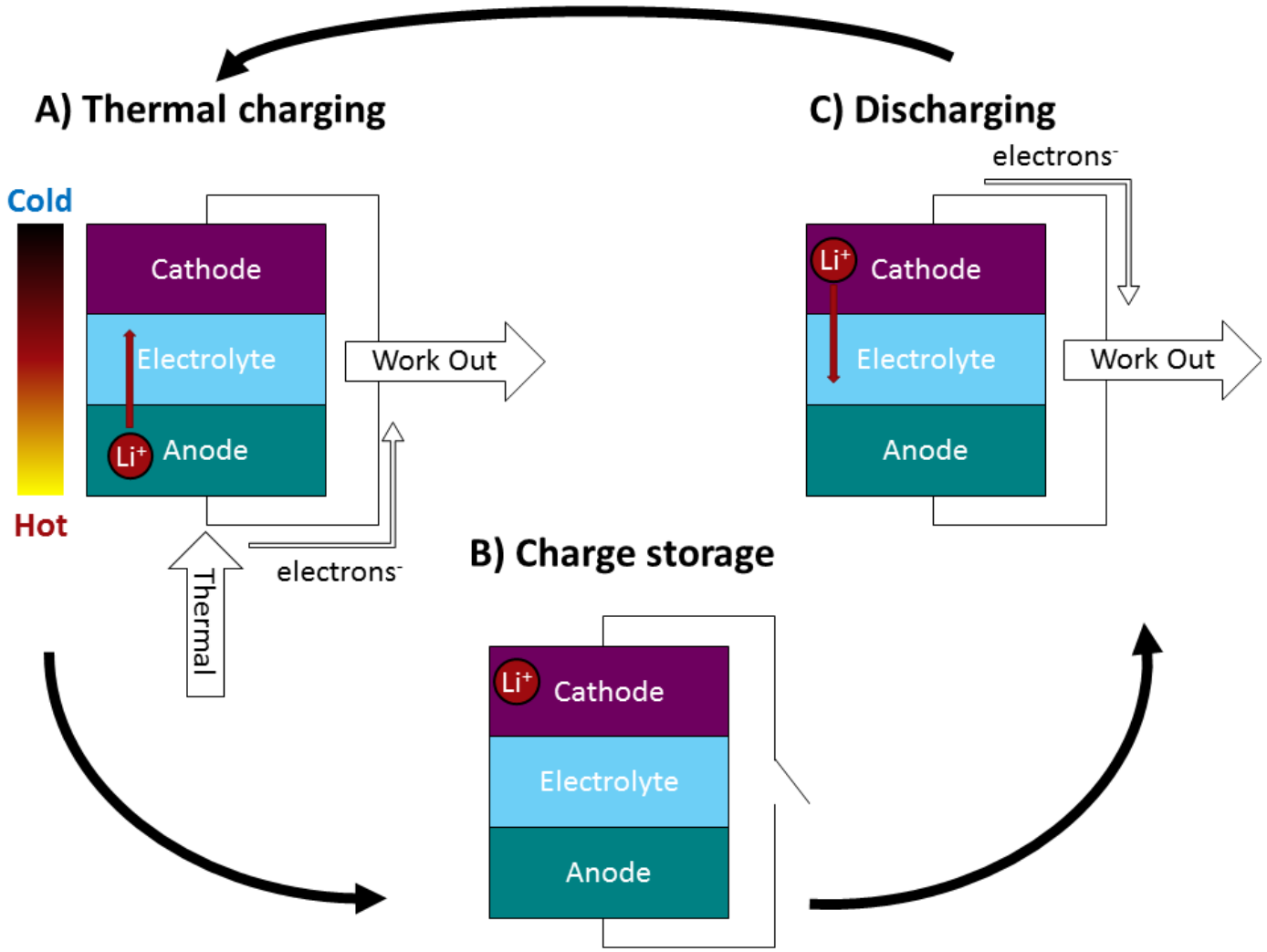

Figure 2.8: Schematic of the proposed solid-state thermogalvanic power generation cycle. A) Non-isothermal charging of the solid-state thermogalvanic cell. B) Charge storage *via* the use of electrodes which can store ions such as intercalation electrodes. C) Discharge of the thermogalvanic cell just as would normally be done with a galvanic cell.

From a thermoelectric perspective solid electrolytes present the most opportunity for optimization based on the strategies developed for solid TE materials. Thermogalvanic systems offer a new platform for the same fundamental materials science investigations which have been done on semiconductor thermoelectric materials including: heat and charge transport in solids, band structure engineering, and the nature of Soret/Seebeck effect in ionic conductors.

From a practical perspective, high temperatures can be achieved by concentrating solar energy. If an all oxide system consisting of intercalation electrodes and a solid electrolyte could be fabricated, large temperature gradients would be possible from a heat source such as this and the cell could be operated at high temperatures. A material science perspective is required to synthesize these complex oxides and ceramics processing techniques can be utilized control the microstructure enabling fundamental studies. Thus, thermogalvanic systems also offer a novel platform for materials engineering including: synthesis of complex, multi-cationic solids and processing of these materials to maintain nanostructures.

Before thermogalvanic materials are explored in Chapter 5 and a thermogalvanic material properties are measured in Chapter 6, oxide based thermoelectric materials are discussed first. Since thermoelectric materials and thermogalvanic materials are directly related, it is seen as worthwhile to spend some time exploring the oxide based thermoelectric materials. As will be shown, synthetic and powder processing techniques developed for work with thermoelectric materials were valuable for thermogalvanic materials as well. Furthermore, the results from Chapter 4 were also useful in interpreting and discussing the results presented at the end of this dissertation in Chapter

6.

CHAPTER 3

EXPERIMENTAL METHODOLOGY

Before the results of the studies discussed above are presented, the experimental methodology used to collect the data is reviewed. This is significant since no procedure is established in the literature for the determination of thermogalvanic materials properties.

3.1 Oxide Thermoelectric Materials

In Chapter 4, samples of composition Na_xCoO2 and $Ca_3Co_4O_9$ were synthesized by a novel solution based technique, named Hydrogel Templed synthesis. Since the development of this method is central to the discussion in Chapter 4, a full description of the method is presented there. For calcination of the sample powders, the "rapid heat up" technique, adopted from the literature [39] was used. In this method, the furnace is first preheated to the calcination temperature without the sample present. Once at the desired temperature, the sample is quickly dropped into the furnace. This helps to minimize the loss of volatile constituent elements such as Na. Using this technique, calcination as a function of temperature was performed to determine the phase formation temperature.

Similarly to the synthesis method, a novel hot-pressing technique was developed for the consolidation of the powders after calcination. The technique is named Rapid Induction Hot-pressing (RIHP) and a full description and rationalization of the technique can be found in Chapter 4. A

study was performed where the consolidation time and temperature were varied. Although some conditions were variables, all samples were consolidated at 62 MPa in graphite dies in air under argon shielding gas. The density of each sample was calculated using the bulk geometry and the mass.

Powder X-ray diffraction data were collected at room temperature on a Rigkau MiniFlex 300 using Cu Kα radiation over 10 - 80 degrees 2θ range with a 0.04 degrees step size and 3 seconds per point.

SEM was performed on a Carl Zeiss EVO LS25 Variable Pressure SEM in backscatter and secondary electron imaging modes.

Raman spectra were collected with a Renishaw inVia Raman microscope using a 532 nm laser, 2400 lines/mm holographic grating and 50x magnification.

Low temperature thermal conductivity, electronic conductivity, and Seebeck coefficient measurements were performed on a custom fabricated cryostat in the Morelli laboratory at Michigan State University over the temperature range 80 - 350K. Cu electrodes adhered with Ag paste were used to make contact with the sample for the measurements. Correction to the thermal conductivity for heat loss due to radiation was performed.

3.2 Garnet Based Li-Ion conducting Solid Electrolytes

In Chapter 5, samples of composition $Li_{7-x}La_3Zr_{2-x}Ta_xO_{12}$ (x = 0.25, 0.5, 0.75, and 1.5) were prepared using a co-precipitation process by collaborators at the Army Research Labs. Li_2CO_3,

$La(OH)_3$, $[ZrO_2]_2CO_2xH_2O$ (zirconium carbonate, basic hydrate; equivalent ZrO_2 content determined from thermogravimetric analysis) weighed in the desired stoichiometry were dissolved in 1.4 M HNO_3 (aq). A 6 wt. percent excess of Li was used to compensate for Li volatilization during synthesis. The stoichiometric amount of $TaCl_5$ was first dissolved in anhydrous ethanol and then added to the Li, La and Zr containing precursor solution. The resulting solution was evaporated to dryness in a microwave oven contained inside a fume hood. Evolution of NO_x was observed during this step. The dried co-precipitate was lightly ground with a mortar and pestle and pressed into a pellet using a Carver laboratory die and press. The pellet was placed on a ZrO_2 plate and heated in air at 1173 K for 3-4 h. The furnace was turned off and the sample was removed.

The powders were consolidated by RIHP at 1323 K and 62 MPa for 1 hr in graphite dies in air under argon shielding gas. The density of each sample was calculated using the bulk geometry and the mass.

Powder X-ray diffraction data were collected at room temperature on a Rigkau MiniFlex 300 using Cu Kα radiation over 10 - 120 degrees 2θ range with a 0.03 degrees step size and 12 seconds per point. A reference pattern for the cubic structure was taken from the ICSD database [40], which had a Ta content of Ta = 0.55.

SEM was performed on a Carl Zeiss Auriga Cross-Beam FIB-FESEM at an accelerating voltage of 15 kV and a working distance of 6.9 mm. 5nm of Pt was sputtered to prevent charging because it is not reactive with Li. The grain size was estimated from the SEM micrographs of the fracture surface using the linear intercept method.

Raman spectra were collected with a Renishaw inVia Raman microscope using a 532 nm laser, 2400 lines/mm holographic grating and 50x magnification. The intensities were normalized to the maximum value. Raman spectroscopy is spot analysis. With the optics used in this experiment, the laser spot size was approximately 5 microns while the average grain size (see SEM analysis below) was approximately 1.4 microns. Since each scan samples a few grains, spectra were collected at 5 random locations several millimeters apart on the RIHPed pellet and the normalized intensities averaged together so that the result was more representative of the bulk sample. The uncertainty in the averaged intensity values was estimated using the standard error of the mean. An undoped tetragonal composition with the nominal formula $Li_7La_3Zr_2O_{12}$ was prepared for reference.

Electrochemical impedance spectroscopy (EIS) was performed with a Bio-Logic SP200 from 7MHz to 10Hz with a 100mV perturbation amplitude and sputtered Pt blocking electrodes. Nyquist plots of EIS data are often modeled using the brick-layer model. In the brick-layer model, it is common to add in parallel combinations of a resistor and a capacitor to represent each semi-circle observed in the Nyquist plot of the impedance spectra. Thus, three parallel combinations are often used, one for the bulk, a second for the grain boundaries, and a third for the electrolyte/electrode interface. This, however, is not a physical representation of the system. For this work, the EIS data were modeled using a modified equivalent circuit proposed by Huggins [41]. Although this model is similar to the conventional brick-layer model, it specifically treats the arrangement of capacitive elements differently. Instead, Huggins placed the capacitive element for bulk transport in parallel with all the other elements in the model since it is a better representation of the physical

arrangement of the system. For a detailed development of the model, the reader is directed to reference [41].

For this study, the model developed by Huggins was modified in three ways. First, the leg of the circuit which corresponds to electronic leakage through the electrolyte was removed since DC measurements have confirmed the electronic portion to be negligible and a low frequency tail was always observed in the impedance spectra. Second, a mass transport element was added in parallel to the capacitor which corresponds to the blocking electrodes since there is some solubility of Li in Pt. This non-ideal blocking behavior of the inert electrodes has been observed in most of the reports of EIS data for LLZO in the literature, regardless of the noble metal used [42–46]. Huggins mentions the use of a Warburg type element to model the mass transport in the blocking electrodes. For this work, an element corresponding to anomalous diffusion was chosen since the electrodes are thin sputtered Pt films. For a full discussion of the impedance response of anomalous diffusive type elements, the reader is directed to reference [47].

Lastly, the capacitors in the Huggins model were replaced with constant phase elements (CPEs) to account for any dispersion to the time constants. The complex impedance response of a single CPE is given by:

$$Z(\omega) = \frac{1}{Q(j\omega)^{\alpha}} \tag{3.1}$$

The ideality of the CPE is represented by the coefficient α. When α is zero, the element is behaving as a resistor and when α is 1 it is behaving as an ideal capacitor. The values for the

ideality coefficient α were allowed to freely refine and settled to values near or exactly 1 after convergence. The values of Q should be on the order of 10^{-12} $\frac{F}{cm^2}$ for the bulk and 10^{-9} $\frac{F}{cm^2}$ for the grain boundaries.

Time of flight neutron powder diffraction data were collected at 300K at the POWGEN beamline at the Spallation Neutron Source (SNS), Oak Ridge National Laboratory (ORNL) with center wavelengths of 1.066Å and 2.655Å at 300K to obtain diffraction patterns that spans from d-spacing of 0.3Å to 6.2Å. High resolution synchrotron powder diffraction data were collected using beamline 11-BM at the Advanced Photon Source (APS), Argonne National Laboratory using an average wavelength of 0.414Å. Discrete detectors covering an angular range from -6 to 16 degrees 2θ are scanned over a 34 degrees 2θ range, with data points collected every 0.001 degrees 2θ and scan speed of $0.01\frac{degrees}{s}$. Rietveld structural refinements of the synchrotron X-ray and neutron diffraction data were performed using GSAS with EXPGUI [48, 49] for the cubic compositions. The synchrotron x-ray source was able to resolve the presence of more than one cubic phase where the neutron beamline, let alone lab scale X- ray diffractometers, was not. This is significant because the POWGEN beamline is a high resolution neutron diffraction facility. Because of this, the Ta and Zr concentrations were first determined with the x-ray histogram and a reasonable estimation at the Li concentration. The neutron histograms were then treated as a single cubic phase and the refined Ta and Zr contents were left fixed so that the Li site distribution could be determined. This process was iterated once where the newly found Li contents were used to again determine the Ta and Zr concentrations. There was no considerable change, the iterations were stopped, and the

structure considered solved. Since the weight fraction of each cubic phase was approximately 50 percent and the differences between them were small (Ta = 0.42 vs 0.57 mols and a = 13.0134 vs 12.9529 Å respectively; Ta = 0.74 vs 0.834 mols and a = 12.9918 vs 12.9317 Å respectively), the refinement of the diffraction data in this manner was seen as reasonable.

3.3 Thermogalvanic Operation of a Solid-State Cell with a Garnet Electrolyte

In Chapter 6, samples of composition $Li_{6.1}Al_{0.3}La_2Zr_2O_{12}$ were prepared using a solid state reaction. Li_2CO_3 (Alpha Aesar, Ward Hill, MA), $La(OH)_3$ (Alpha Aesar), Al_2O_3 (Mager Scientific Inc, Dexter, MI), and ZrO_2 (Inframat Advanced Materials, Manchester, CT) were weighed in the stoichiometric amounts and combined in a 250 ml agate vial with agate grinding media. This precursor mixture was dry-milled in a Retsch PM 100 planetary mill for 4 h at 350 rpm, then pressed into pellets in a 1 inch diameter stainless steel die and calcined at 1273 Kelvin for 4 h under air. The final powder was obtained by grinding the calcined pellets with a mortar and pestle and the powder was stored in a glove box under an argon atmosphere before hot pressing.

The powders were consolidated by Rapid Induction Hot-pressing (RIHP) at 1323 K and 62 MPa for 1 hr in graphite dies in air under argon shielding gas. The density of each sample was calculated using the bulk geometry and the mass.

Electrochemical impedance spectroscopy (EIS) was performed with a Bio-Logic SP200 from 7MHz to 10Hz with a 100mV perturbation amplitude and sputtered Pt blocking electrodes as a

function of temperature. The impedance spectra were modeled using a modified equivalent circuit proposed by Huggins [41] as explained above. The ionic conductivity was measured in the range of 293 - 373K and was fitted to an Arrhenius relationship so that the conductivity could be extrapolated to higher and lower temperatures for the determination of the zT.

Low temperature thermal conductivity and Soret coefficient measurements were performed on two samples on a custom fabricated cryostat in the Morelli laboratory at MSU over the temperature range 200 - 350K. Cu electrodes adhered with Ag paste were used to make contact with the sample for the measurements. Ag paste electrodes is generally considered blocking in the literature [50, 51]. However, it should be noted that investigation of the Ag-Li equilibrium phase diagram reveals considerable Li solubility in Ag [52]. This equipment is commonly used for the measurement of thermoelectric materials. The same procedure was followed with the exception that no DC current was passed through the sample. The temperature difference between the hot and cold ends of the parallelepiped during the Soret coefficient measurement was 1 - 2K. Correction to the thermal conductivity for heat loss due to radiation was performed.

High temperature thermal diffusivity measurements were performed on two samples on a Netzsch LFA 457 MicroFlash from 300 - 750K. The average of three shots was used for each data point. A Pyroceram 9606 sample was also measured for reference. The thermal conductivity was found using the following relationship: $\kappa = DC_p\rho$ where κ is the thermal conductivity in $\frac{W}{cmK}$, D is the thermal diffusivity in $\frac{cm^2}{s}$, C_p is the heat capacity in $\frac{J}{gK}$, and ρ is the density in $\frac{g}{cm^3}$. The C_p was estimated using the Dulong-Petit relationship and was found to be 0.69 $\frac{J}{gK}$. It was assumed

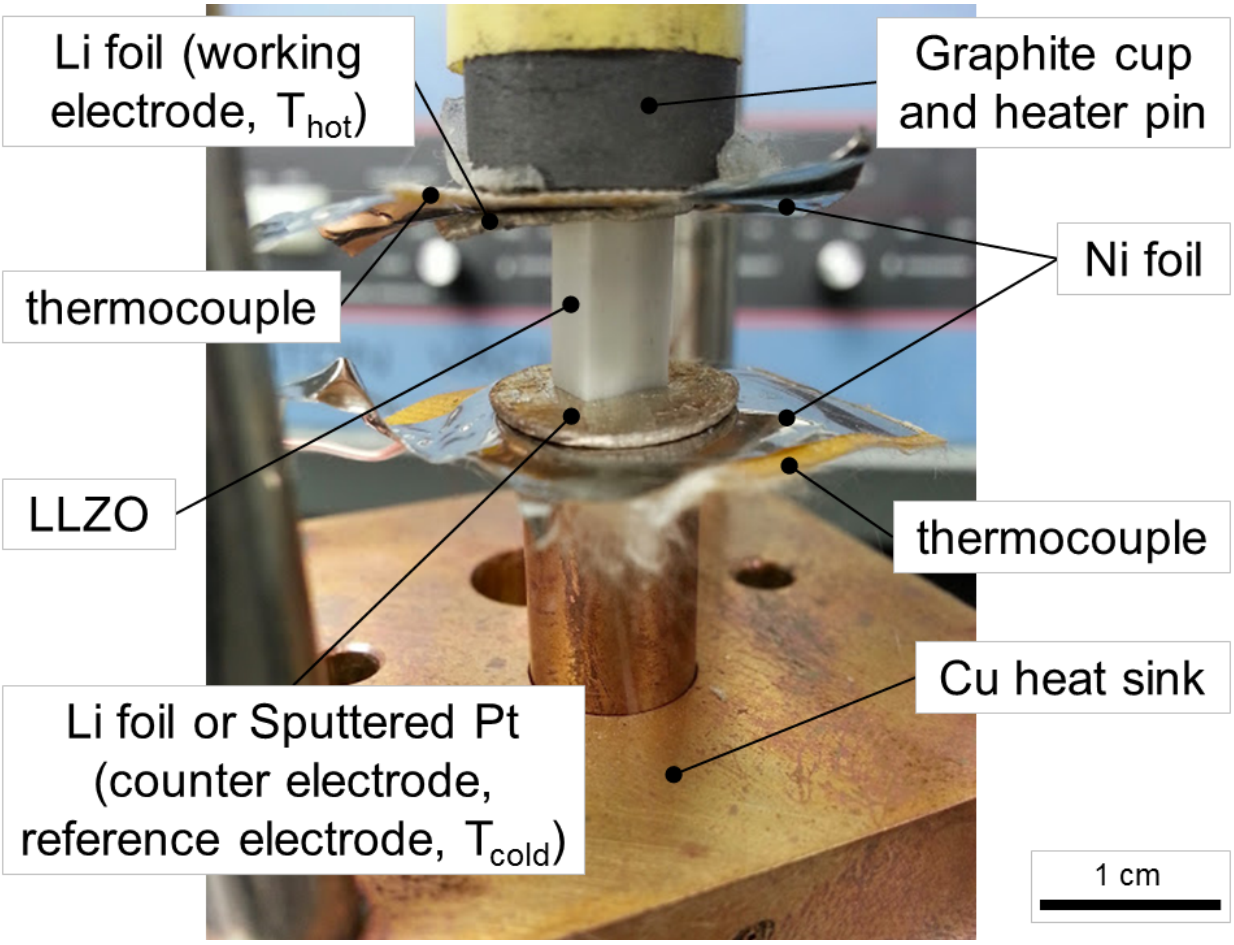

Figure 3.1: Annotated image of the cell used to perform the thermogalvanic measurements at elevated temperatures. The cell is shown prior to connection with the potentiostat.

that the density did not change from the value at room temperature with increasing temperature.

The Soret coefficient was estimated at an elevated temperature using a Li/LLZO/Pt(Li) cell. Since it is unclear if the use of blocking electrodes for the low temperature measurements is valid for the determination of a Soret coefficient, Li foil was used as the hot electrode and plated Li on a sputtered Pt current collector was used as the cold electrode. An annotated image of a typical cell is shown in Figure 3.1. A spring loaded 4-post fixture with a Cu thermal mass was placed on a hot plate and the cell was assembled. Glass fiber reinforced polyimide surface mounting Type-K

thermocouples (Omega SA1XL-K) on both ends of the cell were used to measure the temperature and electronically isolate the cell from the fixture. Ni foil was used as a current collector. Finally, either Li metal foil was used as electrodes on both ends of the LLZO parallelepiped (as shown in Figure 3.1) or one of the electrodes was a sputtered Pt film. The data presented in this report is for a cell which utilized a sputtered Pt film, however, the optional symmetric Li metal foil configuration is shown for completeness. A graphite cup held a resistive heater pin powered by a DC power supply so that a temperature gradient could be established. The Cu block on the cold side acted as a thermal mass and heat sink.

All electrochemical measurements were performed using a Bio-Logic SP200. The Li foil was used as the working electrode and the sputtered Pt film was used as the counter and reference electrode. All potential measurements were made vs the reference electrode. The open circuit potential of the cell was measured as assembled. Li metal was plated by stepping the cell voltage to +1V and performing a chronoamperometric measurement. Plating of Li metal was investigated by an open circuit potential measurement. After this, EIS was performed on the cell from 7 MHz to 10 Hz with a perturbation voltage of 20 mV to confirm the formation of a new Li metal/LLZO interface. The open circuit potential (OCV) was measured while a large temperature difference (55K) was established between the hot and cold electrodes. After the temperature difference stabilized, the temperatures of the electrodes and the OCV were recorded and a Soret coefficient was determined. A counter current was then applied incrementally until the cell reached short-circuit. This data was used to construct an I-V and an I-P curve so that the maximum power output for the cell cold be

determined.

CHAPTER 4

OXIDE THERMOELECTRIC MATERIALS

State of the art thermoelectric materials are based on heavily doped intermetallic semiconductors. This is the result of a rational incremental design approach assuming degenerate semiconductor physics. These assumptions point to covalently bonded materials which are comprised of heavy atoms. As such, systems like Bi_2Te_3 have been commercialized and proven strategies to increase the zT have been developed by the thermoelectric community. While these types of systems are platforms to explore the physics of thermoelectric systems, they have limitations for use in large scale device applications. Namely, these types of thermoelectric systems are often:

1. comprised of toxic elements such as tellurium, lead, or antimony
2. comprised of elements which are not abundant in the earth's crust
3. consist of phases which are not intrinsically stable at high operating temperatures

If a thermoelectric materials design strategy is, instead, approached from the standpoint of these limitations, then a different class of materials is identified. Oxide based materials seem to address all of the limitations identified in conventional thermoelectric materials if systems can be found which also exhibit sufficiently high figures of merit. Oxide materials were originally overlooked for exactly this reason. Since oxide materials are generally comprised of ionically bonded light elements, it was assumed that they would exhibit low electronic mobilities and high thermal

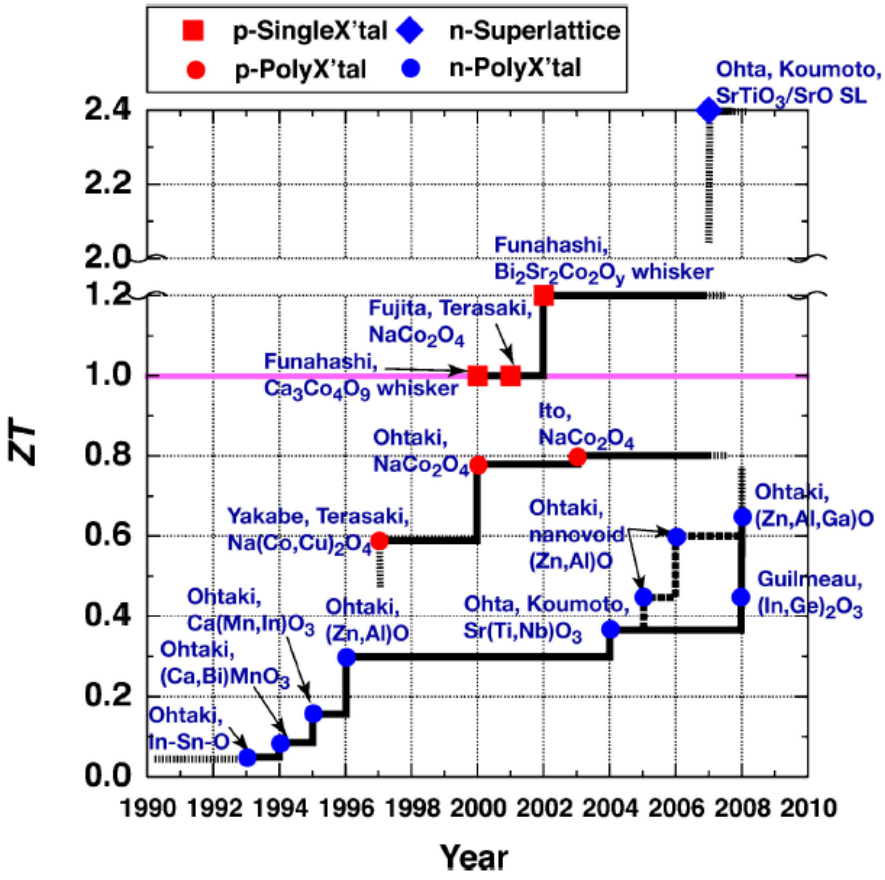

Figure 4.1: Figure of Merit (zT) of various oxide thermoelectric materials as a function of time [53].

conductivities. Indeed, oxides, for example aluminum oxide (Al_2O_3), are wide band gap insulators with relatively high thermal conductivities. However, in 1997, Terasaki *et al.* demonstrated simultaneously high electronic conductivity and a high Seebeck coefficient in a metal oxide, sodium cobalt oxide (Na_xCoO_2, NCO). This was not the first report on oxide thermoelectric materials but demonstration of a large Seebeck and high electronic conductivity was not thought possible prior to this report. Figure 4.1 shows a plot of the reported zT as a function of time for a variety of n- and p-type oxide thermoelectric systems.

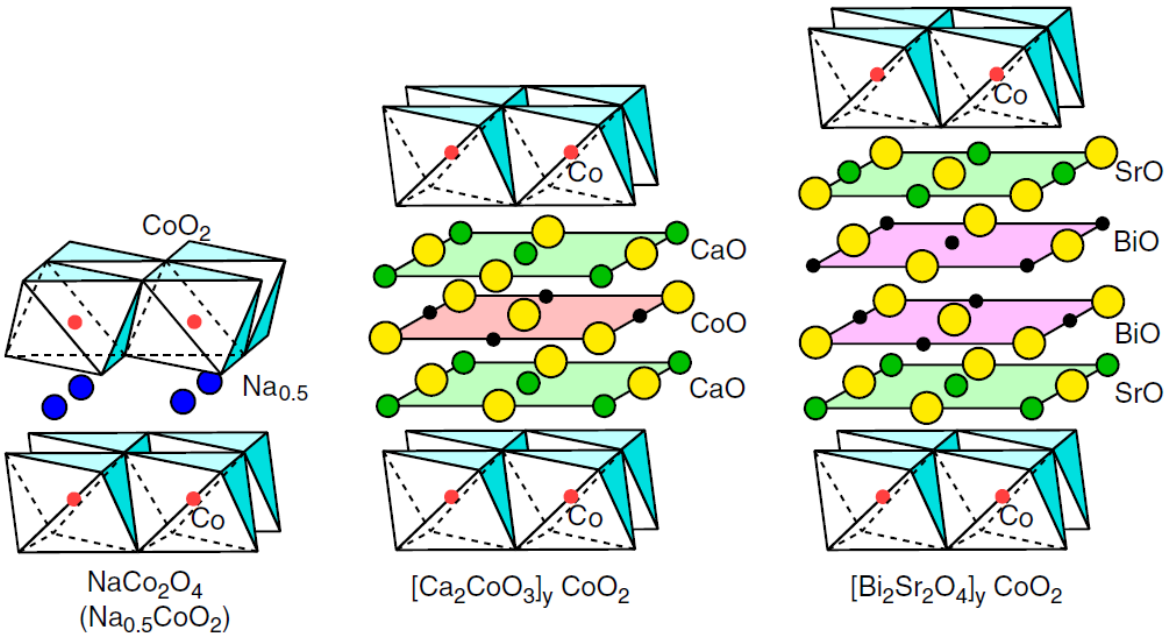

Figure 4.2: Schematic showing the generalization of the layered cobaltate structure including calcium cobalt oxide [53].

Since this first report on NCO, the cobaltate family of thermoelectric materials has been generalized as shown in Figure 4.2 and includes calcium cobalt oxide $(Ca_3Co_4O_9, CCO)$. Figure 4.2 also exemplifies another aspect of these oxide based materials. Since oxides are ceramic materials, the structure is formed from the assembly of coordination polyhedra. These polyhedra self-assemble into the layered phases, for example, and have different properties in each layer. This has lead to a new thermoelectric materials design approach, specific to ceramic materials but complementary to the hierarchical design approach already established in the field, known as nanoblock assembly [15, 54]. In this approach, the structure can be designed so that layers with different properties can be assembled and the properties of the resulting hybrid crystal can be tuned.

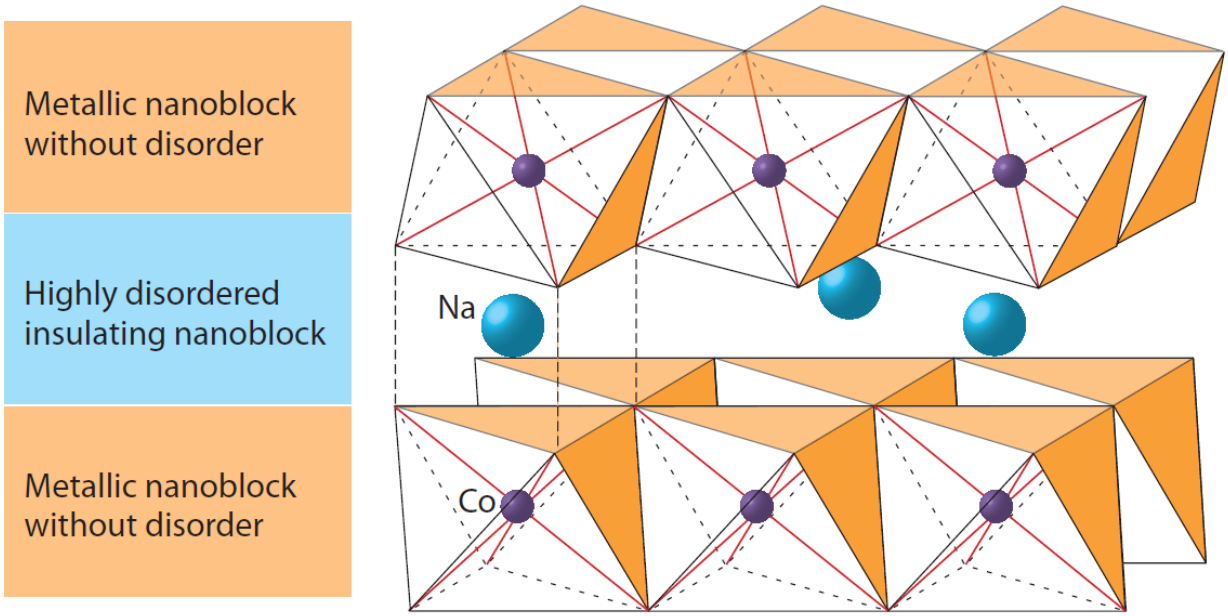

Figure 4.3: Schematic showing the concept of nanoblock assembly of ceramic thermoelectric materials [15].

For example, in NCO (Figure 4.3), the layer of CoO_2 can be thought of as a well connected, orderly, pathway for electronic transport to take place while the Na layer separating the CoO_2 layers is disordered and helps to lower the thermal conductivity. Furthermore, this nanoblock assembly approach can work to approximate superlattice structures, some of which are based on oxides, have exhibited figures of merit greater than 2 [53]. While the n-type systems tend to be based on strontium titanate with perovskite like structures, this work focuses on the p-type nanoblock assembled layered structures based on cobaltates.

While the family of layered cobaltate thermoelectric materials shown in Figure 4.2 offer several advantages, there are synthetic and microstructural issues associated with these systems. The composition of cobaltate thermoelectric materials includes alkali and alkaline earth elements. These

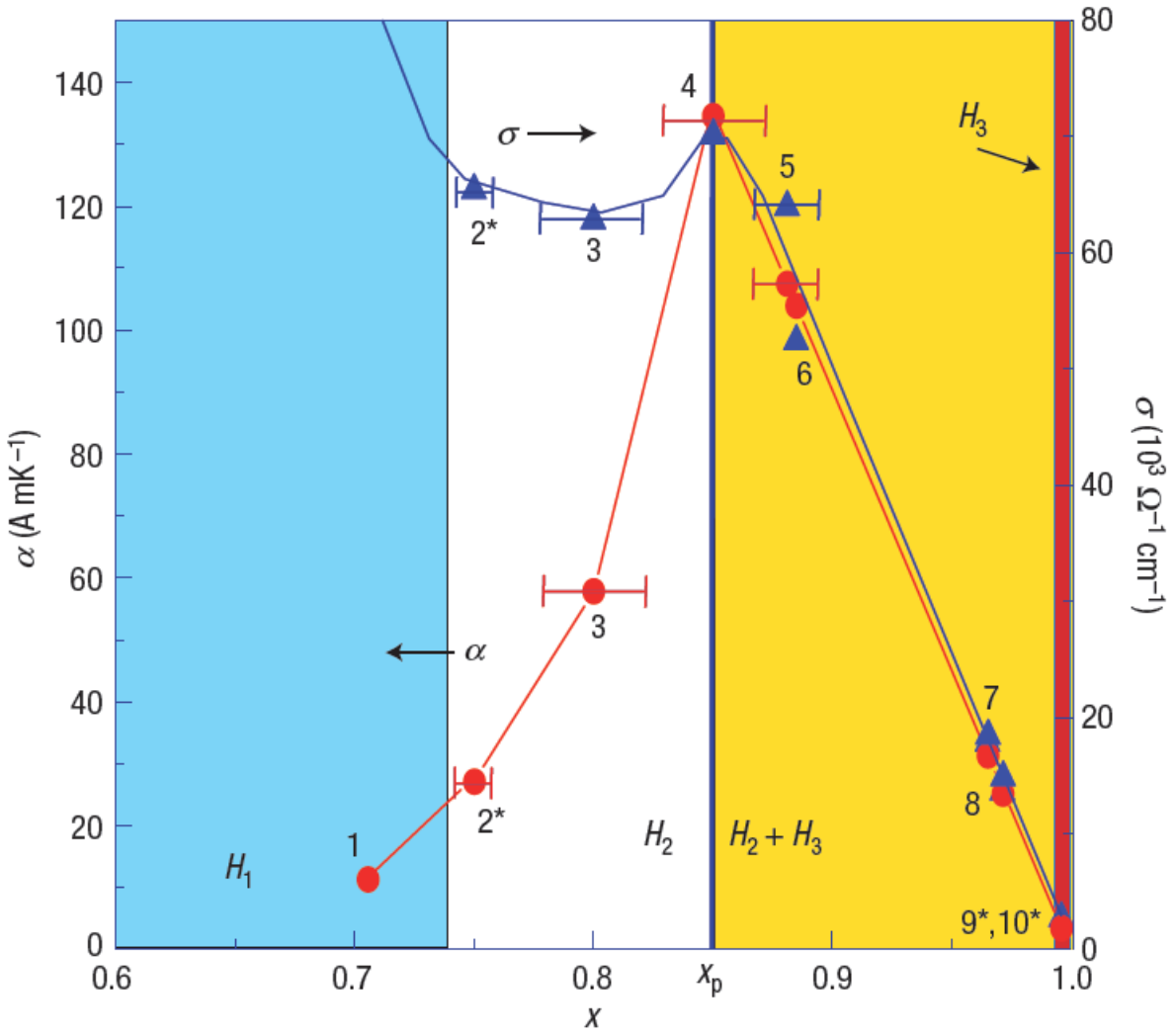

Figure 4.4: Plot of the electronic conductivity and Seebeck coefficient as a function of sodium stoichiometry for Na_xCoO_2 from $0.6 < x < 1$ [55].

elements are volatile, making control of the stoichiometry difficult during synthesis. Control of the stoichiometry is critical in these systems since the material properties change dramatically based on the composition. Figure 4.4 is a plot of the thermoelectric properties as a function of the sodium content in the Na_xCoO_2 $0.6 < x < 1$ system. As the sodium content is changed, a large increase in the electronic conductivity and Seebeck coefficient near x = 0.85 is observed.

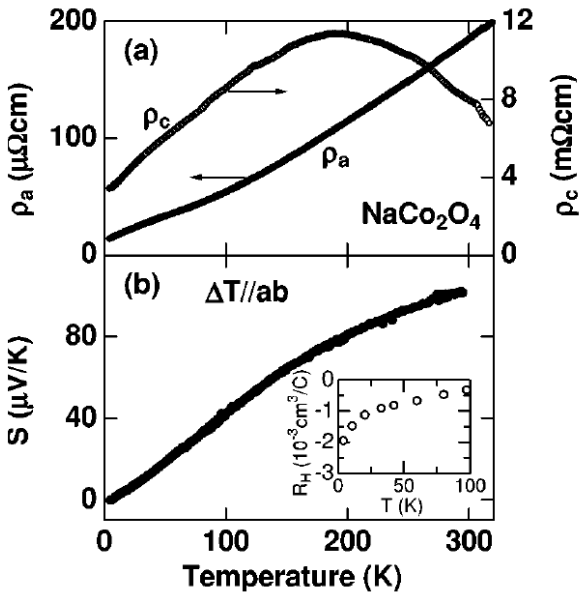

Figure 4.5: Plot of the electronic conductivity and Seebeck coefficient as a function for the material $NaCoO_2$ highlighting the anisotropic transport properties [56].

Since the thermoelectric properties optimize over a narrow compositional range, a high degree of compositional control is necessary when these materials are synthesized. Besides these synthetic issues, there are also microstructural issues present in this system. Using the nanoblock approach, the structure of these materials can be thought of as a disordered low thermal conductivity block layered with a high electronic conductivity block. Because of this layered structure, the transport properties are highly anisotropic. Figure 4.5 shows that the electronic resistivity for NCO varies by three orders of magnitude depending on the direction it was measured. Since a real device will be a sintered powder compact and not a single crystal, a high degree of crystallographic alignment is needed in bulk polycrystalline samples so that the anisotropic transport properties are aligned.

As such, the purpose of this work was to:

explore novel synthesis and powder consolidation techniques to allow for the sintering of a polycrystalline ceramic with a high degree of:

1. compositional control over volatile constituent elements
2. texturing of the microstructure to approximate an ensemble of oriented single crystals

4.1 Solution based synthetic approaches for cobaltate thermoelectric materials

Solid-state reaction (SSR) is the normal method used to synthesize these materials [39]. However, since the elements involved with NCO and (to a lesser extent) CCO are volatile and the level of mixing is on the scale of microns for SSR, impurity phases such as cobalt oxide, which represents the alkali deficient phase, are often present. Excess alkali precursor is normally included and calcination techniques such as "rapid heat up", where the sample is placed into the furnace after it has reached the desired calcination temperature, were developed to help to compensate for the evaporation at high temperature [39]. Still, since the properties are highly dependent on the stoichiometry, using this approach makes it difficult to synthesize a series of samples for investigation with a high degree of compositional control.

Solution based approaches provide better mixing (i.e. shorter diffusion distances) and thus help reduce the fraction of alkali that is lost as vapor. Solution based methods such as the newly developed epoxide addition sol-gel method are available for cobalt based systems [57]. However,

metal salts are used as the precursors in the epoxide addition method and water cannot be used as the solvent due to the gelation mechanism [58,59]. It is possible to find solvents which will dissolve cobalt salts, however, it is more difficult to find non-aqueous solvents for sodium and calcium salts. This solvation issue is exacerbated when many salts are present competing for dissolution with the solvent. Since it became evident that an aqueous solution based synthetic method was necessary, a new technique was developed.

This new method is known as the hydrogel templating method and arose from "cross pollination" with a biomaterials project. Hydrogels are polymeric organic structures which are up to 99 percent porous where the void space is filled with water. An example of a hydrogel material is agarose although several alternatives are available and beyond the scope of this work. Previously, it had been shown that proteins could be immobilize within hydrogels [60, 61]. Because of the similarity in size between proteins and solvated cations [62, 63], it was hypothesized that solvated metal salt precursors could also be entrapped within a hydrogel to prevent phase segregation. More specifically, this method can be thought of as a physical analog to the Pechini method (polymerized complex) or a templated co-precipitation method. It is believed that the micro- and meso-pores of the hydrogel template constrain the size of the salt crystallites as the wet gels containing the precursors are dried and precipitated out of solution. This means that the mechanism that maintains the mixing is physical rather then chemical as in the Pechini method.

Figure 4.6 shows a series of Raman spectra for different combinations of the components used in the synthesis of NCO. It can be seen that all the spectra are simple super-positions of the in-

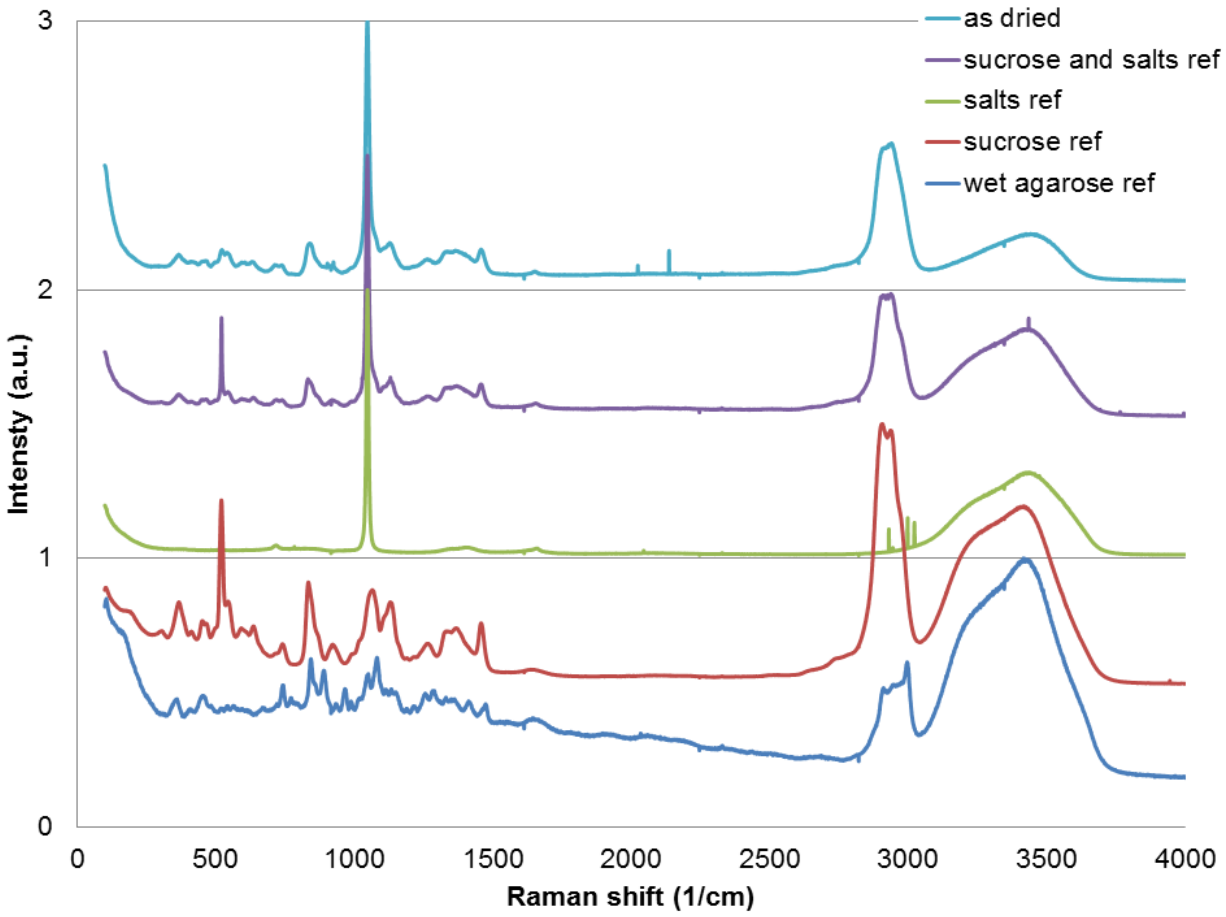

Figure 4.6: Raman spectra of several combinations of the precursors used in the hydrogel templated synthesis of NCO.

dividual components. This is taken as evidence that the template is physically constraining the precipitates in the pores of gel. The physical mechanism simplifies the synthesis of complex oxides with several cations since it is not necessary to form metal ion complexes and polymerize these complexes into a network. Furthermore, since the hydrogel template is organic and non-participatory in the system, it can easily be sacrificed by oxidation at a moderate temperature. After the template has been sacrificed, the method proceeds as a SSR would, however, with the precursors better mixed. In this way, evaporation of volatile elements at high temperature can

be suppressed. Since the development of this method, several phase pure oxide systems besides cobaltate thermoelectric materials have successfully been synthesized in gram scale yields.

To summarize, the new hydrogel method developed out of necessity for the synthesis of cobaltate thermoelectric materials has been generalized to other systems and offers several advantages such as:

1. environmentally friendly since water and naturally derived materials are used as the solvent and template respectively
2. cheap since the precursors are metal salts
3. scalability with batches on the tens of grams having been achieved
4. ease since many metal salts are soluble in water and the templates are easily formed by thermal- or photo- polymerization
5. the ability to form high phase purity complex metal oxides with several cations

Calcination studies to determine the optimal calcination temperate for both NCO and CCO was performed. An SEM micrograph of CCO synthesized using the hydrogel templating method, calcined at 1173 Kelvin is shown in Figure 4.7. High aspect ratio hexagonal crystals several hundred nm in diameter are observed. X-ray diffraction (XRD) was performed to primarily assess phase purity for each temperature (not shown).

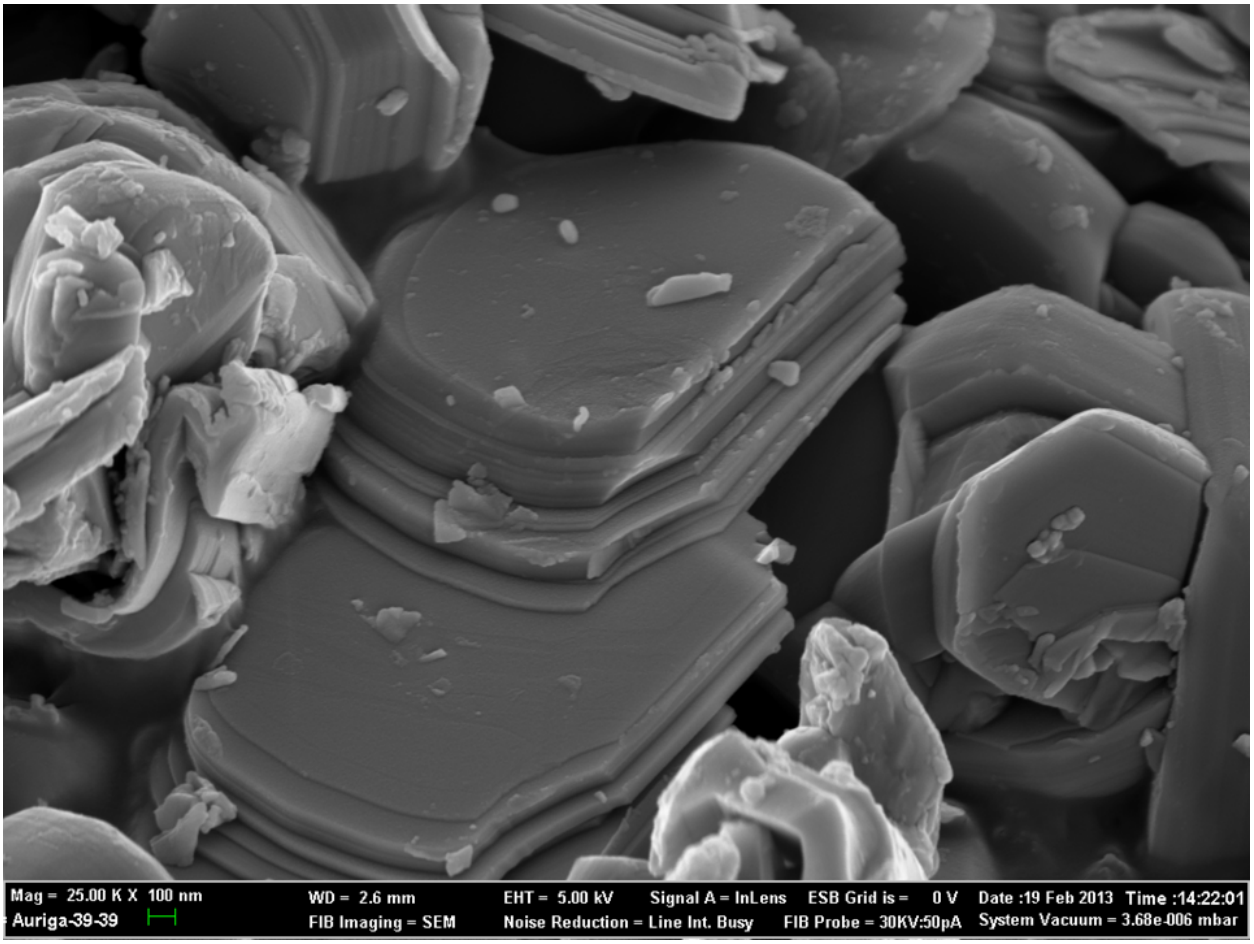

Figure 4.7: SEM micrograph of CCO synthesized using the hydrogel templating method calcined at 1173 Kelvin.

Having established a robust synthetic technique for oxide materials which contain volatile constituent elements, microstructural affects can be explored with less concern regarding the stoichiometry.

4.2 Microstructural investigation of cobaltate thermoelectric materials

There is a large discrepancy between the properties measured on single crystals and their polycrystalline counterparts. This discrepancy has been attributed to the highly anisotropic transport

processes. One approach to improve the properties of polycrystalline compacts is "grain wiring" where a phase with facile electronic transport can bridge grain boundaries and connect grains together which would otherwise be misaligned. It has been observed in this system [64,65] as well as in isotropic systems such as Skutterudite [66] that the inclusion of a second metallic nanophase, i.e. grain wiring, can improve the properties. If the metallic phase can be kept sufficiently nanoscopic, then the increase in electrical conductivity can offset the increase in thermal conductivity, resulting in an overall increase in the zT.

In order to investigate how changes to the microstructure, such as texturing and the inclusion of a metallic nanophase, affect the bulk properties of the material, a consolidation technique is needed which can:

1. provide crystallographic alignment of the grains in the polycrystalline material
2. limit growth of the primary phase to maintain nanoscopic dimensions
3. limit the growth of a secondary metallic nanoparticle so that grain wiring can be performed

Many studies in the literature uses pressureless sintering to densify thermoelectric cobaltate powder compacts [39, 65, 67]. In general, since there is no pressure there is little to no crystallographic alignment and the long times required for the sintering process results in grain/particle growth.

Pulsed electric current sintering (PECS or SPS) meets the requirements necessary outlined above because uniaxial loads can provide texturing in the microstructure and fast heating rates are

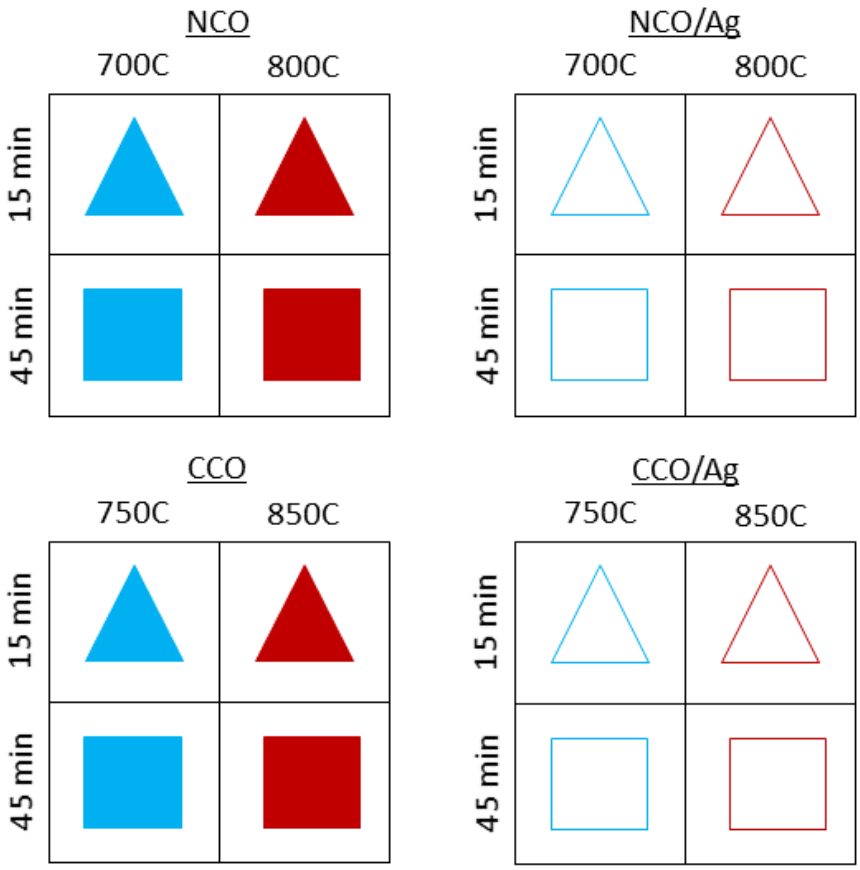

Figure 4.8: Summary of the RIHP conditions used in the texturing study and the symbols used to discuss the results when plotted.

possible which will limit grain growth. However, because a large DC current is used to provide joule heating in the sample, it is possible to strip mobile cations out of the structure. A decrease in properties has been observed in NCO samples which were densified using PECS [68].

Again, since a viable technique for consolidating the ceramic solids was not available, a new technique was developed. A custom apparatus was assembled consisting of an induction heating unit coupled with a hydraulic press. The technique has been named Rapid Induction Hot-pressing or RIHP. As with PECS, the uniaxial load can provide texturing in the microstructure. The induced current, which leads to joule heating in the die, is high frequency AC rather than DC as in PECS.

Ion stripping can be avoided in this manner since no net current flow occurs. Since the heating is localized within the induction coils, fast heating rates and versatility in the die architecture is possible. This enabled an attempt at sinterforging (which is similar to uniaxial hot-pressing but without constraint in the plane perpendicular to the direction of applied pressure) a sample, which will be discussed briefly later in the section. NCO and CCO powders synthesized *via* the hydrogel templating method as discussed above were blended with Ag nanoparticles. The powders were then consolidated with the RIHP technique. The temperature and time, with and without the inclusion of Ag nanoparticles, was varied for the RIHP conditions. The conditions and the symbols used in the plots (below) to discuss them are summarized in Figure 4.8.

4.2.1 Microstructural and thermoelectric Results of Sodium Cobalt Oxide with and without Ag nanoparticle grain wiring

4.2.1.1 Microstructural analysis for Sodium Cobalt Oxide without Ag nanoparticles

Figure 4.9 shows typical SEM micrographs of the polished cross-section after RIHP without the addition of Ag nanoparticles. Figure 4.10 shows x-ray diffraction patterns of the as-pressed pellets and of the as-calcined powders. The Lotgering factors as well as the relative density are shown for each sample in Figure 4.10 as well. The Lotgering factor is a means of estimating the fraction of crystallites which are crystallographically aligned in a particular direction. The intensity of the peaks corresponding to the plane of interest (basal plane of the CoO_2 in this case) are compared to the intensity assuming random distribution (the as calcined powders). The backscattered (BS) and secondary electron (SE) SEM images (Fig. 4.9) also support the calculated Lotgering factors since

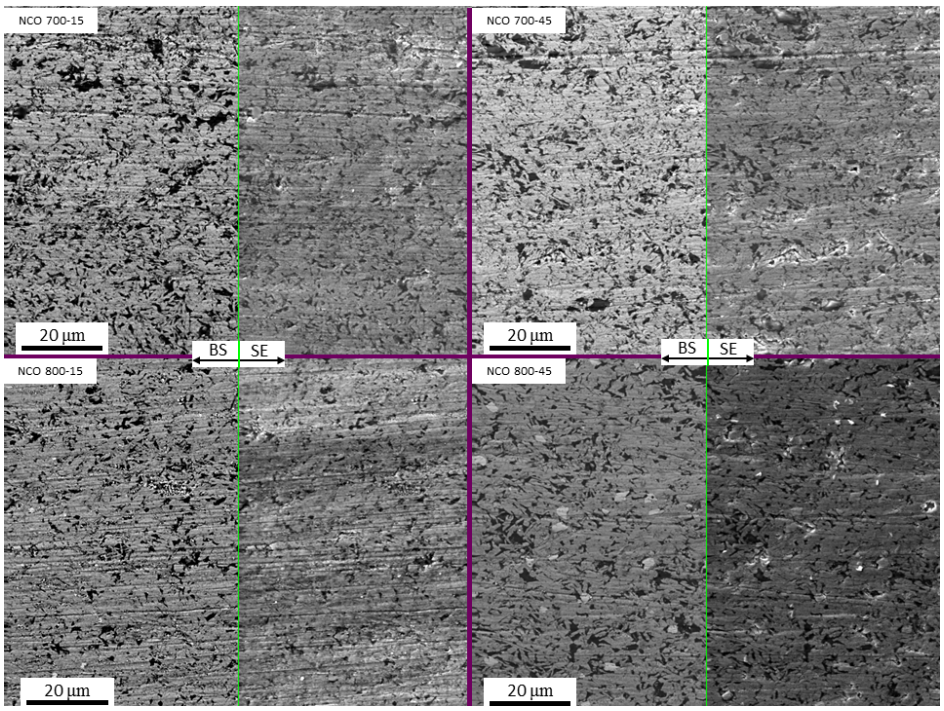

Figure 4.9: Secondary and back-scattered electron micrographs of NCO without the addition of Ag nanoparticles for each of the RIHP conditions used in the texturing study.

dense, apparently textured, regions in the microstructure are punctuated with less dense, randomly oriented regions.

The average relative densities (Fig. 4.10) are lower than would be expected for a hot-pressing technique, such as RIHP. It is possible that some of the volatile constituent elements sublimed and subsequently reacted with the atmosphere during sintering, forming impurity phases such as a carbonate and cobalt oxide (Co_3O_4). Although peaks corresponding to the (Co_3O_4) phase are observed in some of the samples, other impurity phases such as the carbonate could be amorphous and not visible in the diffraction patterns (Fig. 4.10). Comparison of the images shown in Figure 4.9 indeed shows regions which appear like dark pores in the BS images yet look to be filled with some phase in the SE images. This supports the assumption that a low average Z number

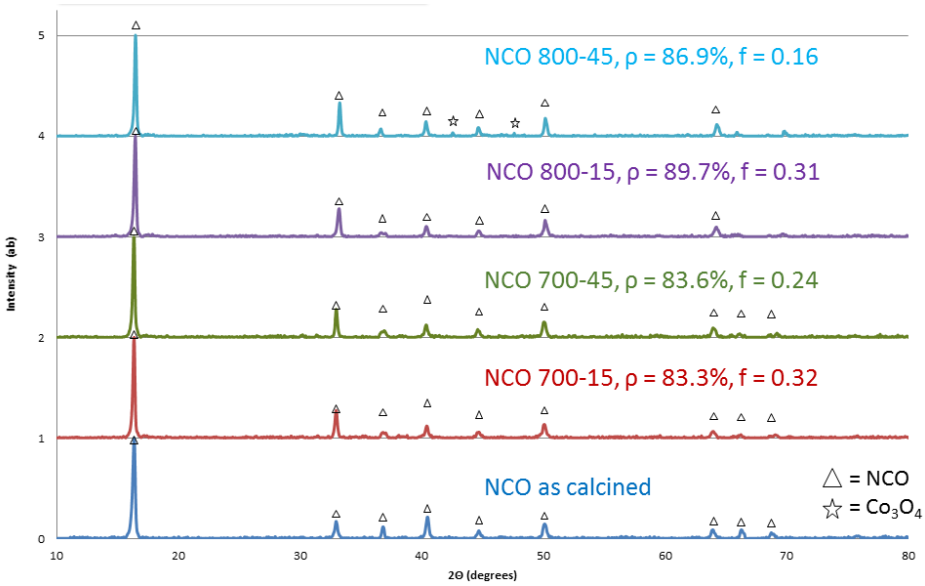

Figure 4.10: X-ray diffraction patterns of NCO without the addition of Ag nanoparticles for each of the RIHP conditions used in the texturing study. Each sample is annotated with their respective relative density and Lotgering factors.

phase, such as a carbonate, is formed during sintering, but is not visible in XRD. However, further work is needed to confirm the identity of the phase, such as Raman spectroscopy. Understanding and preventing the formation of an insulating phase such as a carbonate is important because the formation of an electronically insulating phase on the surface of a sample will impact the ability to make contact for thermoelectric measurements.

Sinterforging was also attempted to further increase the amount of texturing in the microstructure. Sinterforging is a technique similar to uniaxial hotpressing, such as RIHP, but the powder compact is not constrained circumferentially and is allowed to flow in the plane perpendicular to the direction of applied pressure [69]. This creep-like motion can allow for better crystallographic alignment since the basal plans will preferentially lie flat due to the shearing component. How-

ever, due to the reactivity of sodium, severe chemical reactions took place and the sample was bonded to the Pt foil used as a barrier after sinterforging. A small piece was recovered, XRD was performed, and a Lotgering factor of 0.64 was achieved. Perhaps with optimized conditions and a more effective barrier compared to Pt, sinterforging could be viable and more texturing can be achieved.

4.2.1.2 Microstructural analysis for Sodium Cobalt Oxide with Ag nanoparticles

Figure 4.11 shows typical SEM micrographs of the polished cross-section after RIHP with the addition of Ag nanoparticles. Figure 4.12 shows x-ray diffraction patterns of the as-pressed pellets and of the as-calcined powders. The Lotgering factors as well as the relative density are shown for each sample in Figure 4.12 as well.

Most importantly, it should be noted that the presence of Ag seems to promote decomposition of the NCO phase. This is evident by the presence of Co_3O_4 in the XRD patterns (Figure 4.12)and the mosaic of phases seen in the BS SEM images (Figure 4.11). However, since phase decomposition was not expected, NCO powders were not ball milled without the Ag nanoparticles. As such, either the ball milling or the Ag nanoparticles could be responsible for the decomposition. Since many phases are present, the Lotgering factor and the relative density should be treated with some caution and no conclusions are drawn from this data set regarding the NCO phase. However, it does appear that the Ag is well dispersed in the NCO matrix *via* ball milling. Some agglomerates are observed, however, as is often the case with commercially available nanoparticles, it is

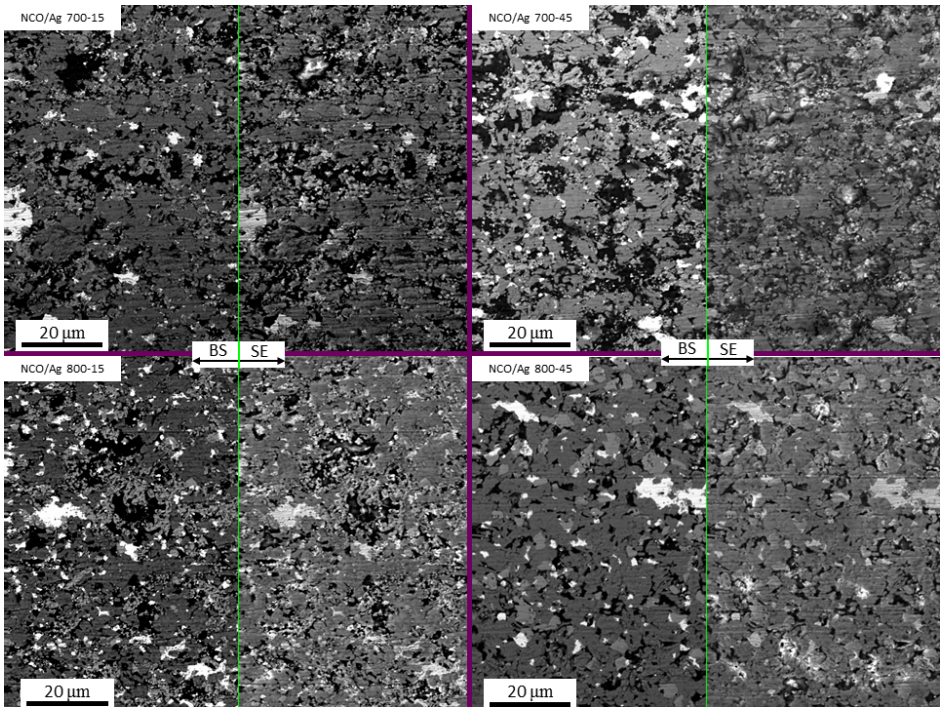

Figure 4.11: Secondary and back-scattered electron micrographs of NCO with the addition of Ag nanoparticles for each of the RIHP conditions used in the texturing study.

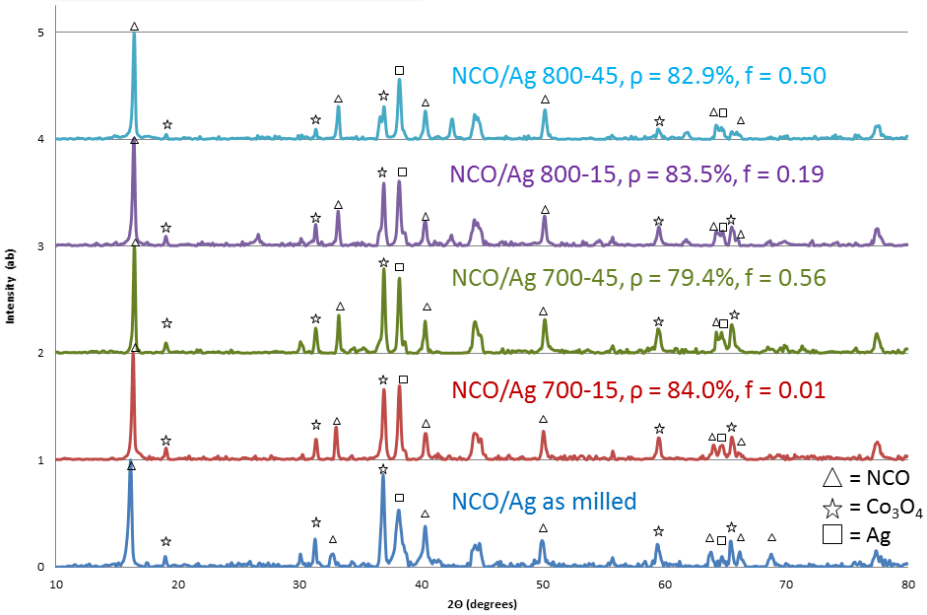

Figure 4.12: X-ray diffraction patterns of NCO with the addition of Ag nanoparticles for each of the RIHP conditions used in the texturing study. Each sample is annotated with their respective relative density and Lotgering factors.

likely that this agglomeration occurred before consolidation and is not a consequence of the RIHP procedure.

4.2.1.3 Sodium Cobalt Oxide Thermoelectric Results

Figure 4.13 shows the thermoelectric property measurements of parallelepipeds cut from the RIHPed pellets with and without the addition of Ag nanoparticles. Measurements were performed in the direction perpendicular to the applied load. Several things can be noted. First, for most of the compositions, there is considerable variation in the measurements where electrical contact is needed. Improved contact with the sample seems to correlate with either the lowest temperature/time for the RIHP procedure and with the addition of the Ag nanoparticles. It is possible that more aggressive RIHP conditions, such as longer time or higher temperature, evaporates more of the volatile constituent element thus forming more of an insulating phase at the grain boundaries. Conversely, the Ag nanoparticles could be increasing the electrical contact between particles as well as external contacts for measurements. This observation is consistent with the SEM images shown in Figure 4.10 and Figure 4.12. Since thermal contact, not electrical, is needed for the thermal conductivity measurement, there is considerably less variation in the data. However, the thickness of the insulating layer could still have an affect on the resistivity.

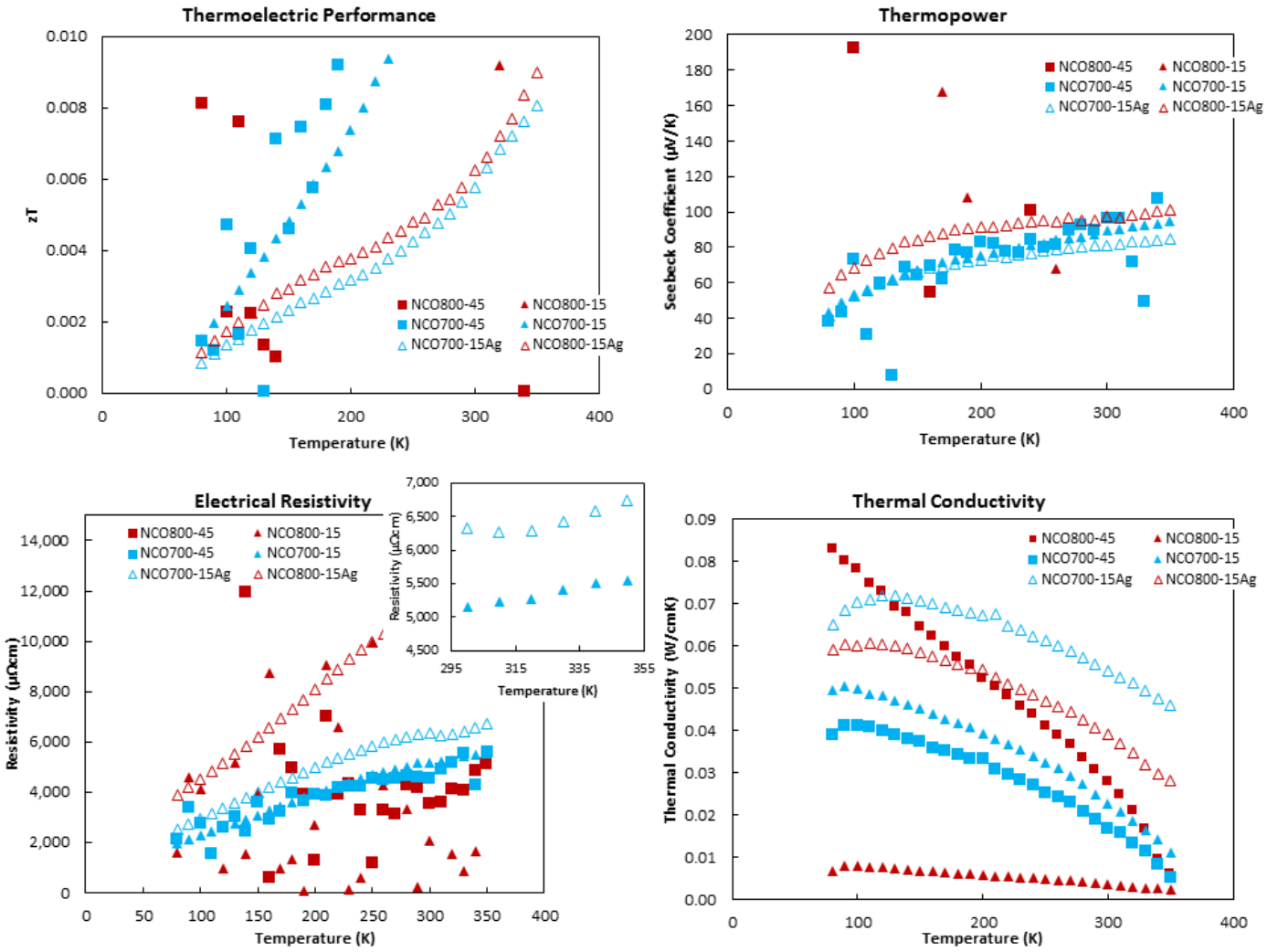

Figure 4.13: Thermoelectric property measurements for NCO with and without the addition of Ag nanoparticles.

Since there is considerable variation in the values, it is difficult to draw conclusions from most of the compositions. However, focusing on the open and filled blue triangles (Fig. 4.13), which correspond to the sample RIHPed at 973 Kelvin for 15 minutes with and without Ag nanoparticles, the various thermoelectric parameters follow what is expected from the results of the XRD and SEM analysis. Namely, the electrical resistivity increases, the thermal conductivity increases, and the thermopower is mostly unchanged. Since the thermal conductivity and the electrical resistivity both increase, the net affect is to lower the overall zT for the material after Ag nanoparticles are added. This is expected because the addition of the Ag particles led to the formation of a significant volume fraction of Co_3O_4, which is electronically insulating. Furthermore, since the Ag was agglomerated and conducts heat well, the particles did not act as scattering centers for phonons and thus the thermal conductivity increased. Since the Ag did not form a percolative network, the Seebeck coefficient was not effected. The affect of the Ag particles on the thermal conductivity could be mitigated if the Ag nanoparticles are more evenly dispersed in the matrix. Since the agglomeration is mostly likely present in the as-received materials and the ball milling used to disperse the nanoparticles into the matrix is already leading to phase decomposition, increasing the milling time or power to better disperse the nanoparticles will most likely no lead to an increase in the performance. Instead, a thermal decomposition reaction, of a silver nitrate for example, will most likely be a more promising route. It is unclear why the Ag promoted the phase decomposition observed in XRD.

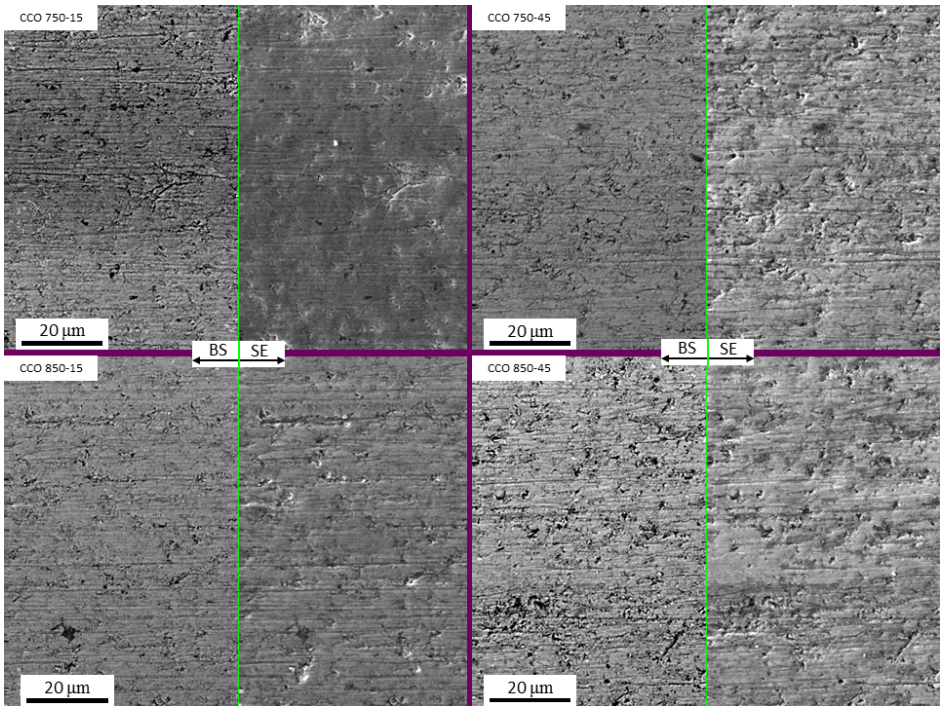

Figure 4.14: Secondary and back-scattered electron micrographs of CCO without the addition of Ag nanoparticles for each of the RIHP conditions used in the texturing study.

4.2.2 Microstructural and thermoelectric Results of Calcium Cobalt Oxide with and without Ag nanoparticle grain wiring

4.2.2.1 Microstructural analysis for Calcium Cobalt Oxide without Ag nanoparticles

Figure 4.14 shows typical SEM micrographs of the polished cross-section of CCO after RIHP without the addition of Ag nanoparticles. Figure 4.15 shows x-ray diffraction patterns of the as-pressed pellets and of the as-calcined powders. The Lotgering factors as well as the relative density are shown for each sample in Figure 4.15 as well.

Unlike the NCO, the CCO exhibits residual precursor phases (CaO and Co_3O_4) after calcination which finish reacting to form the CCO phase during powder consolidation. For consistency, the "rapid heat up" technique was also used during calcination. It is thought that this technique

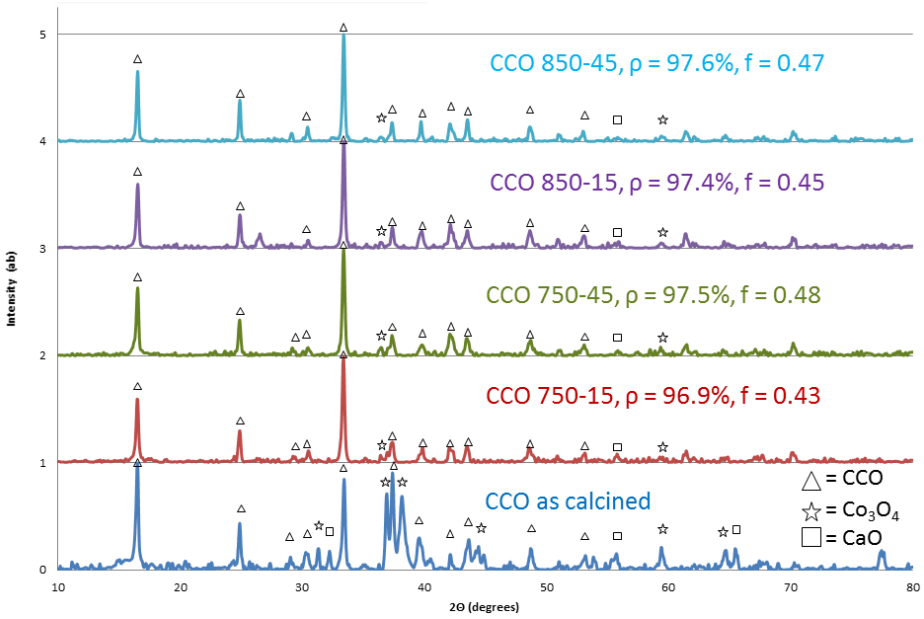

Figure 4.15: X-ray diffraction patterns of CCO without the addition of Ag nanoparticles for each of the RIHP conditions used in the texturing study. Each sample is annotated with their respective relative density and Lotgering factors.

is responsible for the unreacted precursors observed. The relative densities are much higher compared to the NCO and are what is expected for a technique such as RIHP. The Lotgering factors are also more consistent with values of approximately 0.4 or higher. Both the BS and SE SEM images support what is observed in the diffraction patterns. The SE images show little porosity and the BS images show little Z contrast. These results indicate that CCO is more stable compared to NCO. This is not unexpected since the Ca in the layer separating the Co_2 layers is a rocksalt structure with Co and O (Fig. 4.2), and thus more stable.

4.2.2.2 Microstructural Analysis for Calcium Cobalt Oxide with Ag nanoparticles

Figure 4.16 shows typical SEM micrographs of the polished cross-section after RIHP with the addition of Ag nanoparticles. Figure 4.17 shows x-ray diffraction patterns of the as-pressed pellets

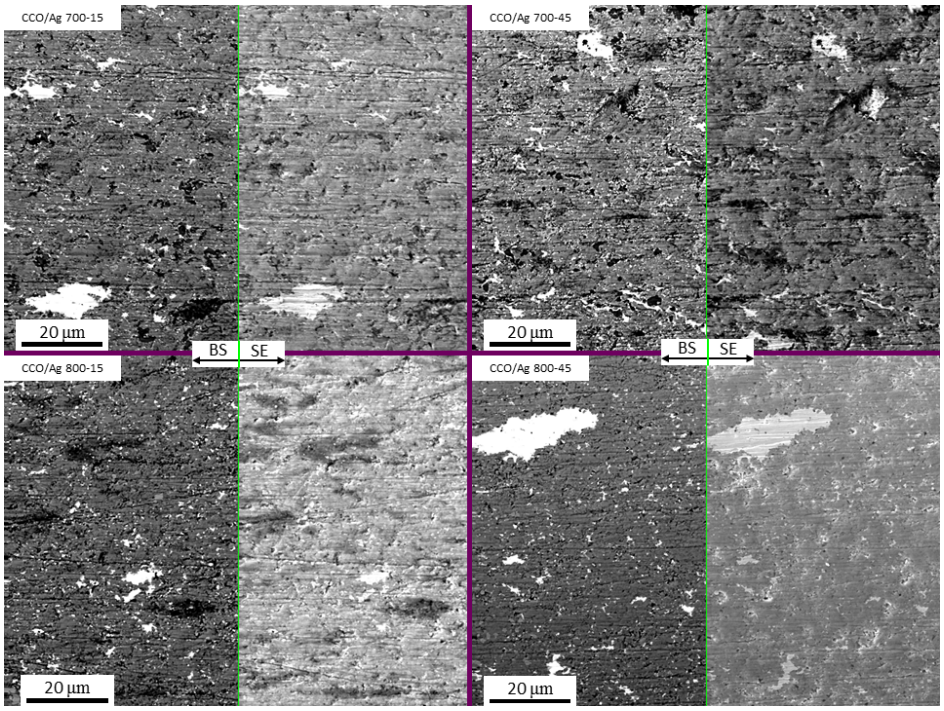

Figure 4.16: Secondary and back-scattered electron micrographs of CCO with the addition of Ag nanoparticles for each of the RIHP conditions used in the texturing study.

and of the as-calcined powders. The Lotgering factors as well as the relative density are also shown for each sample in Figure 4.17.

Unlike the NCO system, the addition of Ag nanoparticles seems to promote the completion of the synthesis reaction. Similar to the results without the addition of Ag nanoparticles, the phase purity increases upon consolidation. The SEM images supports the high relative density and phase purity observed in Figure 4.16. Again, large agglomerates of Ag are seen in the SEM micrographs and this agglomeration is likely present int he as-received commercially available Ag nanoparticles. Unlike the NCO system where the addition the nanoparticles *via* ball milling decomposed the phase, increasing the ball milling time or power may be an effective means to break up Ag agglomerates and better disperse the nanoparticles into the matrix.

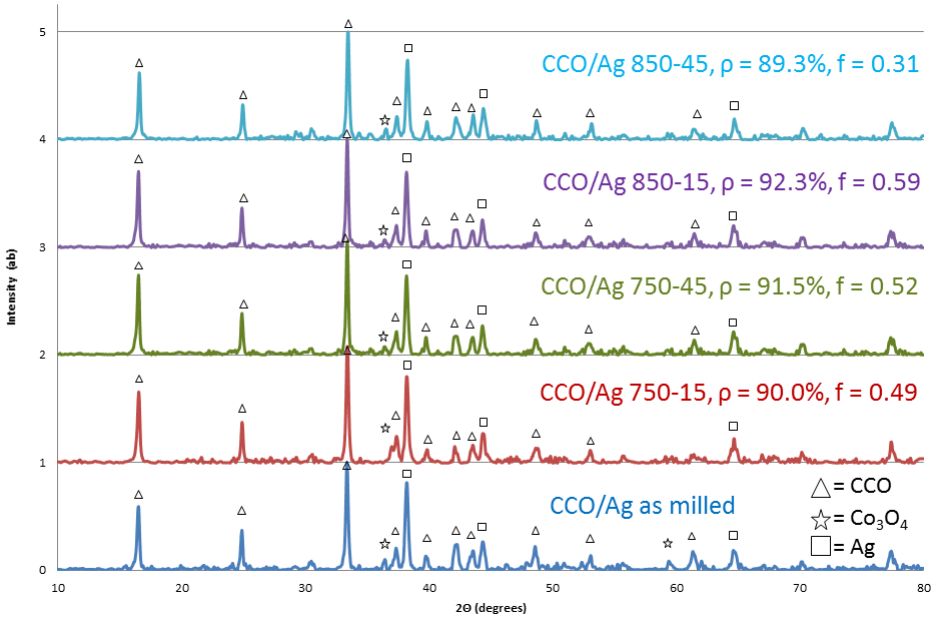

Figure 4.17: X-ray diffraction patterns of CCO with the addition of Ag nanoparticles for each of the RIHP conditions used in the texturing study. Each sample is annotated with their respective relative density and Lotgering factors.

4.2.2.3 Calcium Cobalt Oxide Thermoelectric Results

Figure 4.18 shows the thermoelectric property measurements of parallelepipeds cut from the RIH-Ped pellets with and without the addition of Ag nanoparticles. Measurements were performed in the direction perpendicular to the applied load.

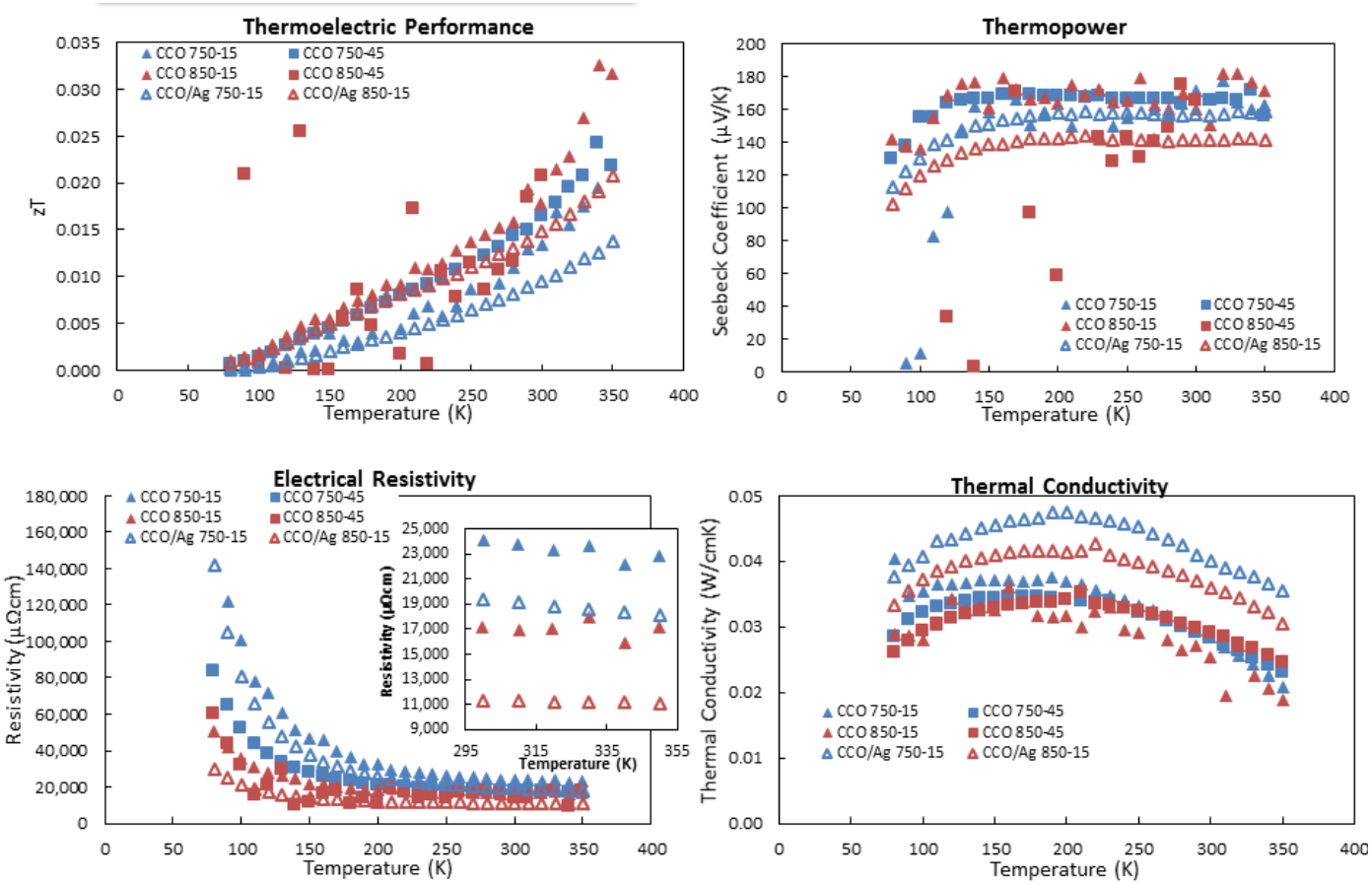

Figure 4.18: Thermoelectric property measurements for CCO with and without the addition of Ag nanoparticles.

Although the variation in the data is better compared to the NCO system, it is still appreciable for some compositions. It is apparent from this study that facile electrical contact with a semi-conducting oxide for measurements is not trivial, even when the system is more chemically stable. The trends observed when agglomerated Ag nanoparticles are added to the system are what is expected. The electrical resistivity decreases, the thermal conductivity increases, and the thermopower remains mostly unchanged. Since the thermal conductivity increases more than the electrical resistivity decreases, the result is that the over all zT is reduced. Like the NCO, if the Ag particles can be kept sufficiently nanoscopic, it is expected that a net increase in the zT would be observed.

4.3 Discussion

Oxide thermoelectric materials like these cobaltate systems are primarily limited by their electronic conductivities. The inherently low electronic conductivities can be further hampered by resistive phases, such as carbonates, residing at grain boundaries in a polycrystalline bulk ceramic material. As such, improving the electronic connection from one grain to another was attempted by the addition of silver nanoparticles. No improvement to the over all zT performance was observed over the temperature range investigated because the decrease in the electrical resistivity was more then offset by an increase in the thermal conductivity. This is most likely due to large Ag agglomerates which are likely present in the as-received commercial powders. A more effective approach would be to form the Ag nanoparticles in-situ on the surface of the cobaltate powders [64]. However, a

second heating step will likely exacerbate the volatility issue and carbonate formation discussed through out this chapter. Furthermore for this same reason (i.e. the formation of an insulating layer at the grain boundaries), even if a high degree of texturing of the microstructure is possible, it seems unlikely that polycrystalline powder compacts will ever match the performance of their single crystal counterparts. Since the growth of single crystals is likely impractical in large quantities and of sufficient size, this, then, suggests that the cobaltate thermoelectric oxides investigated here may be platforms for scientific investigations but will have many difficulties for commercialization of a device.

This is an unfortunate conclusion since oxide materials offer several advantageous discussed in the introduction to this chapter. This begs the question: Can the advantages that oxide based thermoelectric materials present still be utilized, but by some other means? Oxides are known conductors of ions. Is it possible to utilize ions as charge carriers in a thermoelectric device? Indeed this is possible and, as discussed in Chapter 2, such a device is known as a thermogalvanic. Thermogalvanic devices are the direct electrochemical analog to thermoelectric devices. Solid Li-ion conducting oxides will be investigated from this perspective in the next chapter.

CHAPTER 5

GARNET BASED LI-ION CONDUCTING SOLID ELECTROLYTES

Oxides offer several advantages compared to traditional thermoelectric materials. However, because of synthetic and microstructural problems discussed in the previous chapter, it is unlikely that polycrystalline layered cobaltate powder compacts will ever match the performance of their single crystal counterparts. As discussed in Chapter 2, thermogalvanic devices utilize ions as the charge carrier and are the direct electrochemical analog to thermoelectric devices. If an oxide material could be found that has sufficiently large ionic carrier mobility, large thermopower, and low thermal conductivity, then sustainable thermal-to-electric energy conversion could be achieved in a thermogalvanic device. Since the charge carriers are ions, then the oxide material is similar to an electrolyte in a galvanic cell. Furthermore, if the same oxide material is electrochemically stable with anode and cathode electrode materials, then the same device could be used for charge storage as well as thermal-to-electric energy conversion. Li metal anodes have been under development for high energy density galvanic cells. As such, Li metal should be targeted for thermogalvanic systems for the same reasons. Therefore, the necessary criteria for a thermogalvanic material with the capabilities for charge storage are:

1. is a solid

2. sufficiently high total ionic conductivity

3. negligible electronic conductivity

4. electrochemical stability with anode and cathode electrodes

5. sufficient mechanical properties to resist dendrite penetration

6. large thermopower (Soret coefficient)

7. low thermal conductivity

It is the opinion of the author that the first three criteria must first be met for a materials system before further exploration into the remaining properties in undertaken. As such, this chapter focuses on the ionic conductivity of potential solids for thermogalvanic devices. From the battery community, several solid electrolytes have been under development and this knowledge is applicable for thermogalvanic devices as well. In the following sections, the state of the art materials systems are briefly discussed and a candidate material, based on the garnet crystal structure, is selected and characterized in detail to understand the Li transport.

5.1 Introduction to Li-ion Conducting Solid Electrolytes

Figure 5.1 is an Arrhenius plot of the ionic conductivity vs temperature for several state of the art electrolytes [70, 71]. For bench marking purposes, conventional liquid electrolytes used in Li-ion batteries are also included [72]. Although beyond the scope of this work, other ionic conductors, such as Na β"-alumina (shown in Figure 5.1) or yttria stabilized zirconia (not shown) may also be viable thermogalvanic electrolytes and are mentioned for completeness.

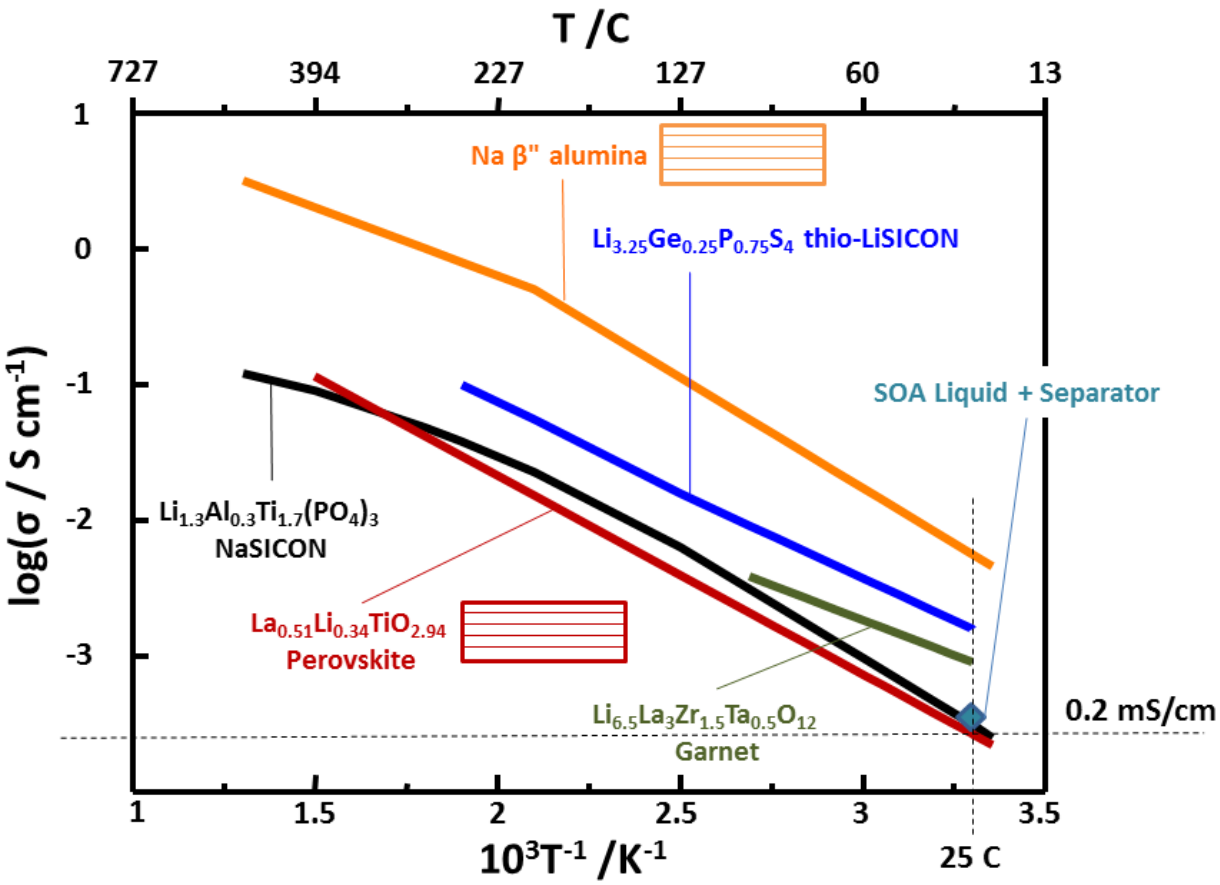

Figure 5.1: Arrhenius plot of the ionic conductivity of several state of the art electrolytes [70–72].

The liquid electrolyte used in conventional Li-ion galvanic cells is typically composed of a Li containing salt dissolved in a solvent. The salt primarily used is $LiPF_6$ and the solvent used is typically a blend of two or more carbonates such as propylene carbonate (PC) and ethylene carbonate (EC). Typical conductivities for a liquid solution such as this are near 10 - 100 $\frac{mS}{cm}$. This is usually the number quoted as the benchmark for an acceptable ionic conductivity. However, in a real galvanic cell, a separator is always used. Therefore, a more realistic estimation of an acceptable ionic conductivity should include the separator. The separator most commonly used is a porous polypropylene polymer film and, when soaked with liquid electrolyte, has a conductivity

near 0.4 $\frac{mS}{cm}$ [72]. When Figure 5.1 is viewed from this perspective, it can be seen that several solid systems have sufficient ionic conductivity to function as an electrolyte. However, fast ion conduction is not the only requirement for an electrolyte in a thermogalvanic cell.

Besides fast ion conduction, chemical and electrochemical stability of the electrolyte are important. As can be seen in Figure 5.1, many systems exhibit sufficient ion conductivity. However, several of these systems (such as the pervoskite LLTO and the NaSICON LATP), contain the element Ti. This is problematic because Ti can be chemically reduced by metallic Li, an anode material of great interest, making the electrolyte partially electronically conductive [73]. Therefore, systems which contain Ti and other elements which can be chemically reduced by metallic Li, are not chemically stable and will not be usable in a cell where metallic Li is used as the anode (unless some kind of protective barrier is deposited). Similarly, even if no chemical reduction/oxidation reaction occurs simply by contact with an electrode, systems may not be electrochemically stable upon cycling. For example, the thio-LiSICON system $Li_{3.25}Ge_{0.25}P_{0.75}S_4$ exhibits one of the highest reported conductivities and is chemically stable against metallic Li. However, upon cycling, a solid-electrolyte interphase (SEI) forms due to decomposition of the electrolyte and the overall cell impedance increases with increasing cycle number. Finally, microstructural affects may dominate the over all performance of the system. For example, the LLTO system (mentioned previously) exhibits bulk conductivities on the order of $10^{-3}\frac{S}{cm}$, however, due to high impedance at the grain boundaries, has a total conductivity on the order of $10^{-5}\frac{S}{cm}$.

Finally, the mechanical properties of thermogalvanic solid electrolytes cannot be ignored.

When AgI based materials were studied previously [26], the primary failure mechanism was Ag dendrite penetration upon thermal cycling. The dendrite penetration was slowed, but not stopped, when a porous alumina disk was impregnated with AgI [26]. Similarly, Na dendrite penetration has been observed in Na β"-alumina used in AMTEC devices [22,74]. Finally, Li dendrite penetration is a known failure mechanism in Li-ion galvanic cells [75,76]. Since this work is focusing on Li conducting solids, the discussion surrounding the mechanical properties will be held in that context. Theoretical models for Li dendrite penetration through solid electrolytes (namely polymers and polymer composites) have been developed by those working in the galvanic cell community. In these models, it is suggested that a solid material must posses a shear modulus of 1 - 4 times the shear modulus of Li metal, depending on the Poission's ratio of the material, in order to resist mechanical penetration by a Li dendrite [77,78]. Since Li metal has a shear modulus of 1.2 GPa [79], this corresponds to a critical shear modulus for a solid electrolyte of 1.2 - 4.8 GPa. As such, materials such as those based on polymers do not have sufficient mechanical properties [78]. However, it has been shown that LLZO has a shear modulus of 52 - 59 GPa [80]. This is an order of magnitude greater than the critical shear modulus and LLZO should have sufficient mechanical properties to resist dendrite penetration. However, it should be noted that this has yet to be validated experimentally.

It is evident from the above discussion that the simultaneous fulfillment of all these criteria (i.e. large total conductivity, chemical stability against a metallic Li anode, electrochemical stability at high and low potentials, and mechanical stability) in a single material is difficult. However,

recently a new materials system based on the garnet crystal structure has been identified which simultaneously meets the material selection criteria mentioned above.. The conductivity behavior of Garnet type Li-ion conducting solids are discussed in some detail next. Then, in Chapter 6, the remaining thermogalvanic properties (i.e. Soret coefficient and thermal conductivity) are discussed.

5.1.1 Garnet based materials

Garnet based Li-ion conductors are garnering interest because of the unprecedented combination of high ionic conductivity, low grain boundary resistance, moderate chemical stability in air, chemical stability at low voltages against Li metal, and electrochemical stability > 5V [81–84].

The term "Garnet" is a reference to a crystal structure and materials with this structure are referred to as "Garnets" for the remainder of this work. Garnets can have a variety of compositions, and thus, applications. Found naturally, garnets are gemstones but a widely researched application of garnets is as a lasing medium. Yttrium aluminum garnets (YAG) and yttrium iron garnets (YAG) lasers are beyond the scope of this work but are included to highlight the compositional versatility of the structure. For Li-ion conducting applications, the composition can be generalized as $Li_xRe_3M_2O_{12}$ where $Re =$ a rare earth atom in +3 oxidation state such as La^{3+}, Pr^{3+}, Nd^{3+}, Sm^{3+}, Eu^{3+}, Gd^{3+}, Tb^{3+}, Dy^{3+}, Ho^{3+}, Er^{3+}, Tm^{3+}, Yb^{3+}, and Lu^{3+} [85] and $M =$ a transition metal. The Li content can be changed depending on the oxidation state of the transition metal. Li contents as from $x = 3$ for $M = +6$ atoms such as Te^{6+} [85, 86] and W^{6+} [87], to $x = 5$ for

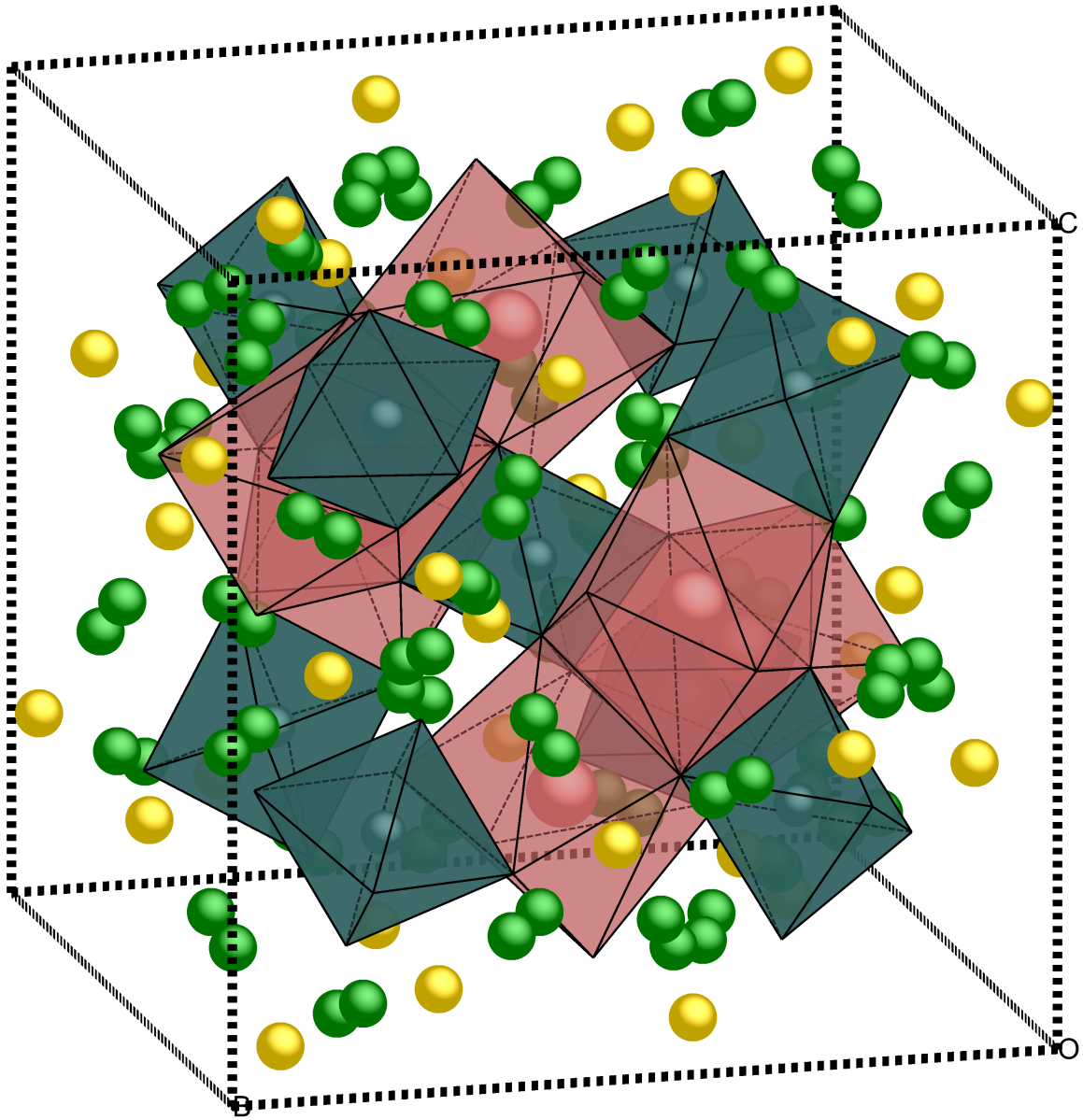

Figure 5.2: Garnet crystal structure.

$M = +5$ atoms such as Sb^{5+} [86–88], Nb^{5+} [81, 89–91] and Ta^{5+} [71, 88, 90, 92], to $x = 7$ for $M = +4$ atoms such as Zr^{4+} [71, 81, 91], Sn^{4+} [89] and Hf^{4+} [93] have been demonstrated. It is hypothesized that $x = 7.5$ is the maximum for the structure [94].

The garnet structure, shown in Figure 5.2, consists of edge-sharing MO_6 octahedra and ReO_8

dodecahedra forming an isotropic skeleton framework through which Li-ions and vacancies form a percolative sublattice of nearly energy equivalent tetrahedrally and distorted octahedrally coordinated Li sites with oxygen (Wycoff positions 24d and 96h respectively). The octaherdal sites are not normally populated in the garnet structure. As discussed later in the chapter, since these sites become more populated as the Li content increases, the formulations with $x > 3$ are also known as "stuffed" garnets. Initial work identified $Li_5La_3M_2O_{12}(M = Nb^{5+}, Ta^{5+})$ as a promising formulation having a total conductivity of 0.04 mS/cm at room temperature [84, 95–97]. Recently, Weppner *et al.* discovered a formulation exhibiting up to 1 mS/cm at room temperature [46]: $Li_7La_3Zr_2O_{12}$ (aka LLZO). It was later found that as the Li content approaches $x = 7$, a reduction of symmetry from the high conductivity cubic phase to a low conductivity tetragonal phase occurs. Thus, a dopant is needed to tune the Li content and stabilize the cubic phase.

Of the potential solid electrolytes, stuffed garnet materials are a complicated system but clearly exhibit many promising properties. As such, $Li_7La_3Zr_2O_{12}$ (LLZO) based materials were selected as a potential thermogalvanic material. However, before further thermogalvanic testing was performed, a detailed study to understand the Li ionic transport in these materials was performed.

5.2 Correlating the atomic structure and ionic transport in garnet-based superionic conductors

The general experimental approach for studying ceramic oxide electrolytes involves powder synthesis, sintering powders into dense polycrystalline specimens, and electrochemical impedance

spectroscopy (EIS) to measure the ionic transport properties. Among the numerous studies that used this general approach, it is known that Al from sintering in alumina crucibles can significantly affect the outcome of a study. First, it is known that adventitious Al is readily incorporated into the Li sub-lattice occupying the 24d site (see Figure 5.2for a graphical description of the Li sites) while creating two Li vacancies to maintain charge neutrality [42, 98, 99]. Interestingly, it is believed that the creation of approximately > 0.40 moles of Li vacancies is necessary to stabilize cubic LLZO, which is reported to have from a 17 to 37 fold higher bulk conductivity compared to the tetragonal phase [42, 45, 99, 100]. Thus, it is clear that Al acts as a dopant and can dramatically affect the bulk phase stability and, therefore, the ionic conductivity. Second, some reports in the literature believe that the presence of Al only affects sintering, which in turn affects grain boundary resistance [101]. Likewise, when EIS is used to characterize the ionic conductivity it is difficult to isolate the affect(s) of Al in the bulk and grain boundary conductivities.

It was hypothesized that stabilizing cubic LLZO by substituting Ta^{5+} for Zr^{4+} will mitigate the potential compounding affects caused by the Al, thus enabling a correlation between Li-ion site occupancy, phase stability, and bulk conductivity in LLZO. Although there have been numerous investigations involving Ta-doped LLZO, no studies have investigated these aspects over a broad range of Ta concentrations with no Al present. In this study, the degree of substitution was varied over a broad range to help establish trends in Li site occupancy/concentration and conductivity; $Li_{7-x}La_3Zr_{2-x}Ta_xO_{12}$ (x = 0.25, 0.5, 0.75, and 1.5).

A hot pressing technique was employed to rapidly heat LLZO powders while applying pres-

sure to reduce Li loss and maximize density without depending on Al to enhance sintering. The hot pressing technique achieved uniformly high relative densities (> 97 percent) to allow for the accurate measurement of the bulk and grain boundary conductivities. By accurately measuring the bulk conductivity, based on the Zr/Ta ratio, the relationship between Li site occupancy and ionic transport can be elucidated. The purpose of this work was to conduct a detailed study to understand the variables involved in maximizing bulk conductivity in LLZO based garnets with the compositional series $Li_{7-x}La_3Zr_{2-x}Ta_xO_{12}$ (x = 0.25, 0.5, 0.75, and 1.5).

The cubic to tetragonal phase transformation was first explored using the subcritically doped composition ($Li_{6.75}La_3Zr_{1.75}Ta_{0.25}O_{12}$) and the critically doped composition ($Li_{6.75}La_3Zr_{1.75}Ta_{0.25}O_{12}$). Table top x-ray diffraction, SEM analysis, Raman spectroscopy, Electrochemical Impedance Spectroscopy (EIS), and synchrotron x-ray and neutron diffraction were performed to confirm that 0.4 - 0.5 mols of Li vacancies are needed to stabilize the cubic phase, regardless of the doping site. Concurrently, the same characterization techniques were used with the remaining compositions so that compositional trends could be established. SEM analysis was used to confirm that the microstructures were comparable. Raman spectroscopy was used as a probe for the presence of the tetragonal phase an to confirm that the Ta^{5+} dopant is substituting for Zr^{4+} as assumed. EIS was performed and equivalent circuit modeling was used to separate the bulk and grain boundary conduction processes. The conductivity measurements were collected as a function of temperature and Arrhenius plots were constructed to extract the activation energy. In addition, Rietveld refinement of synchrotron X-ray and neutron powder diffraction were performed

for the cubic compositions. The refinement of the diffraction data allowed for determination of the Li site occupancy. Finally, the results from all of these data sets were used to holistically draw conclusions regarding the conductivity behavior of LLZO. In conjunction with these experiments, density functional calculations and molecular dynamic simulations were performed by others. The experimental results from this work were compared to the results in the literature, when available.

5.2.1 The cubic-to-tetragonal phase transformation in Ta doped LLZO

As mentioned above, LLZO based garnets can exist in two phases: cubic or tetragonal. The conductivity of the tetragonal phase at room temperature is approximately 2 orders of magnitude lower than that for the cubic phase [43, 100]. Thus, the challenge has been to stabilize the cubic phase of LLZO. It was found experimentally that 0.2 – 0.24 mols of Al substitution (0.4 – 0.48 Li vacancies) per formula unit in LLZO stabilized the cubic phase [42]. Subsequently, combination density functional and molecular dynamics computations suggested that a critical Li vacancy concentration in the range 0.4 – 0.5 per LLZO formula unit, regardless of how the vacancies are introduced, is required to stabilize the cubic phase [99]. One method to achieve the critical Li vacancy concentration and hence, stabilize cubic LLZO, is through the substitution of supervalent cations such as Al [42, 98], Ga [71, 102], Fe [103] for Li, and / or Nb [81, 91], Ta [40, 101], Sb [104] for Zr which results in the formation of Li vacancies to balance the extra positive charge of the supervalent cation. The critical Li vacancy concentration predicted by computation for cubic LLZO agrees well with experimental results required to obtain cubic LLZO when substitution is performed on

the Li sublattice, for $Li_{7-3x}M_xLa_3Zr_2O_{12}$ where the critical amount of M = Al (x = 0.2) [42], Ga (x = 0.2) [102] and Fe (x = 0.19) [103]. Since the dopant resides on the Li site, only two Li vacancies are created even though three Li atoms are expelled. In contrast for the case of Nb [81, 91], Ta [40, 101], Sb [104] , where the substitution is performed on the Zr site, it has been reported that the cubic phase is obtained for $Li_{7-y}La_3Zr_{2-y}M_yO_{12}$ (where M = Nb, Ta, Sb) for y as low as y = 0.2. This is about 2 times lower than the critical amount (y = 0.4 – 0.5) predicted computationally. Thus, there is agreement between predictions when supervalent cation substitution is performed for Li, while there is disagreement when the supervalent substitution is performed for Zr. One possible reason is that the heat-treatment was performed in alumina crucibles for samples where the supervalent cations (Nb, Ta, Sb) were substituted for Zr [40,81,91,101,104]. Thus, there is the possibility that Al entered the lattice [105] in addition to the intentional doped supervalent cation and hence, the actual Li vacancy concentration is higher than expected. Since Al substitution on a Li site creates twice as many lithium vacancies compared to substitution of a M^{5+} (such as Nb, Ta and Sb) on a Zr site, a small amount of extra Al can make a large difference on the actual vacancy concentration and the resulting phase. As a result this study was undertaken to determine if the previous experimental observations for Al substitution [42] and the computations of Bernstein *et al.* correctly predict the stability of tetragonal versus cubic phase for the case of supervalent doping on the Zr site without the presence of Al. In this work Ta^{5+} was selected as the supervalent dopant owing to its comparable ionic radius [106] and the creation of Li vacancies when substituting for Zr^{4+}. Al uptake into the LLZO samples was prevented since no alumina labware was used in any

of the processing steps. In this study, the nominal compositions $Li_{6.75}La_3Zr_{1.75}Ta_{0.25}O_{12}$ and $Li_{6.5}La_3Zr_{1.5}Ta_{0.5}O_{12}$ were investigated. The Ta = 0.25 composition was selected because it is less than the critical Li vacancy concentration predicted to stabilize the cubic phase (and thus will be referred to as the subcritically doped composition). This composition has been shown to be the composition with maximum conductivity in a related LLZO series where the Nb^{5+} ion was used [81, 91]. The Ta = 0.5 composition was selected because it is at or near the critical Li vacancy concentration predicted to stabilize the cubic phase [99] (and thus will be referred to as the critically doped composition).

5.2.1.1 X-ray diffraction

X-ray diffraction (XRD) was conducted on the two compositions and is shown in Figure 5.3. Both diffraction patterns exhibit the cubic garnet structure with trace impurities. As reported by other groups for Nb [81, 91], Ta [40, 101], Sb [104], both the critically doped $(Li_{6.5}La_3Zr_{1.5}Ta_{0.5}O_{12})$ and subcritically $(Li_{6.75}La_3Zr_{1.75}Ta_{0.25}O_{12})$ doped compositions appear to be cubic from the XRD. However, these reports likely had Al present as previously discussed. In this work, the observance of the cubic structure with XRD for the critically doped composition is in agreement with what is predicted. However, the observance of the cubic XRD pattern for the Al - free subcritically doped composition $(Li_{6.75}La_3Zr_{1.75}Ta_{0.25}O_{12})$ was unexpected since there should be insufficient Li vacancies. In order to further investigate the structure of Al - free sub- and critically doped LLZO garnet the sample powders were hot-pressed and further materials characterization

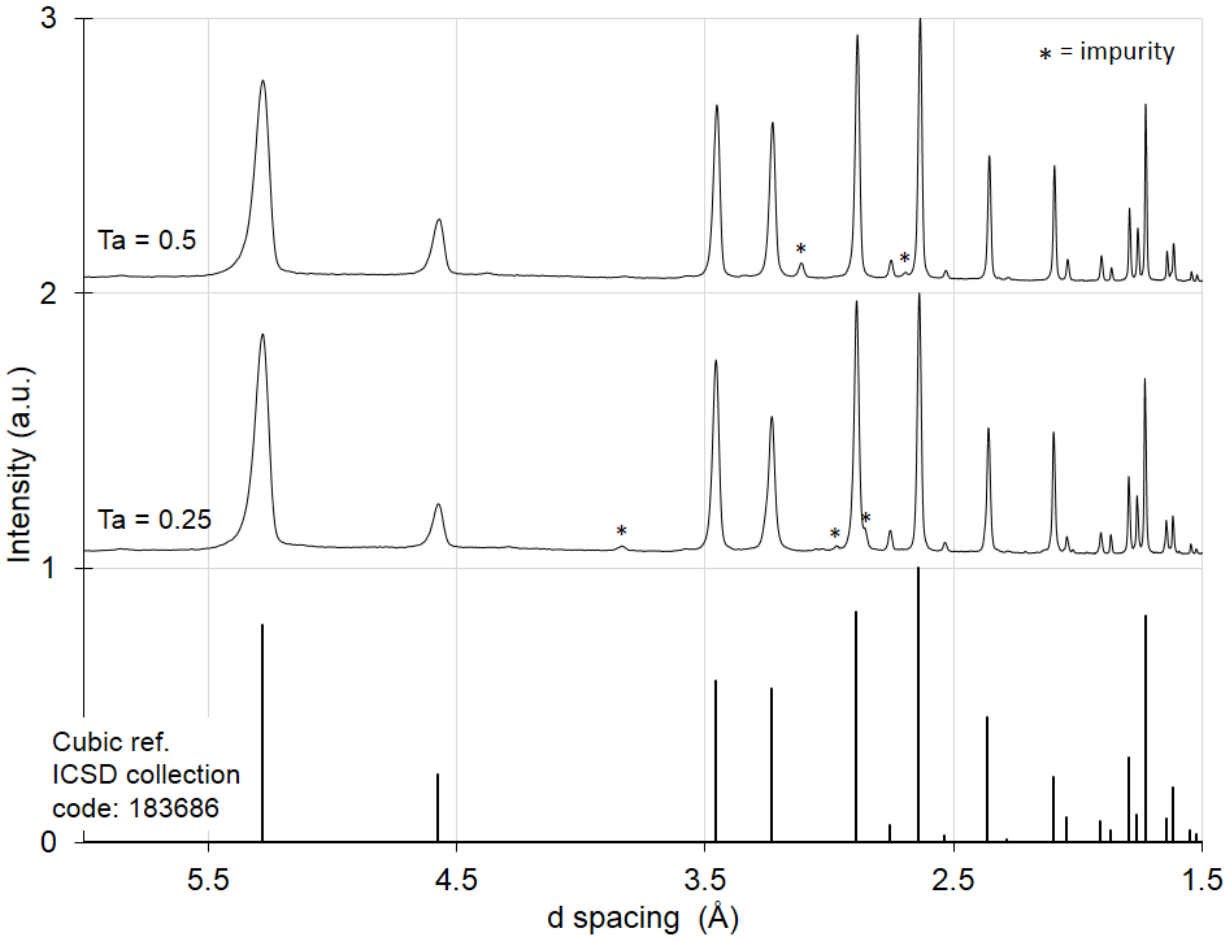

Figure 5.3: X-ray diffraction pattern of the composition $Li_{6.5}La_3Zr_{1.5}Ta_{0.5}O_{12}$, the composition $Li_{6.75}La_3Zr_{1.75}Ta_{0.25}O_{12}$, and a cubic reference [40]. Peaks corresponding to impurities are marked by an asterisk.

was performed.

5.2.1.2 Microstructural analysis

After hot pressing the powders, SEM analysis was performed on fracture surfaces of the nominal compositions $Li_{6.75}La_3Zr_{1.75}Ta_{0.25}O_{12}$ and $Li_{6.5}La_3Zr_{1.5}Ta_{0.5}O_{12}$ to characterize the fracture mode, grain size, and porosity (Figure 5.4). The remaining compositions are discussed later in this section.

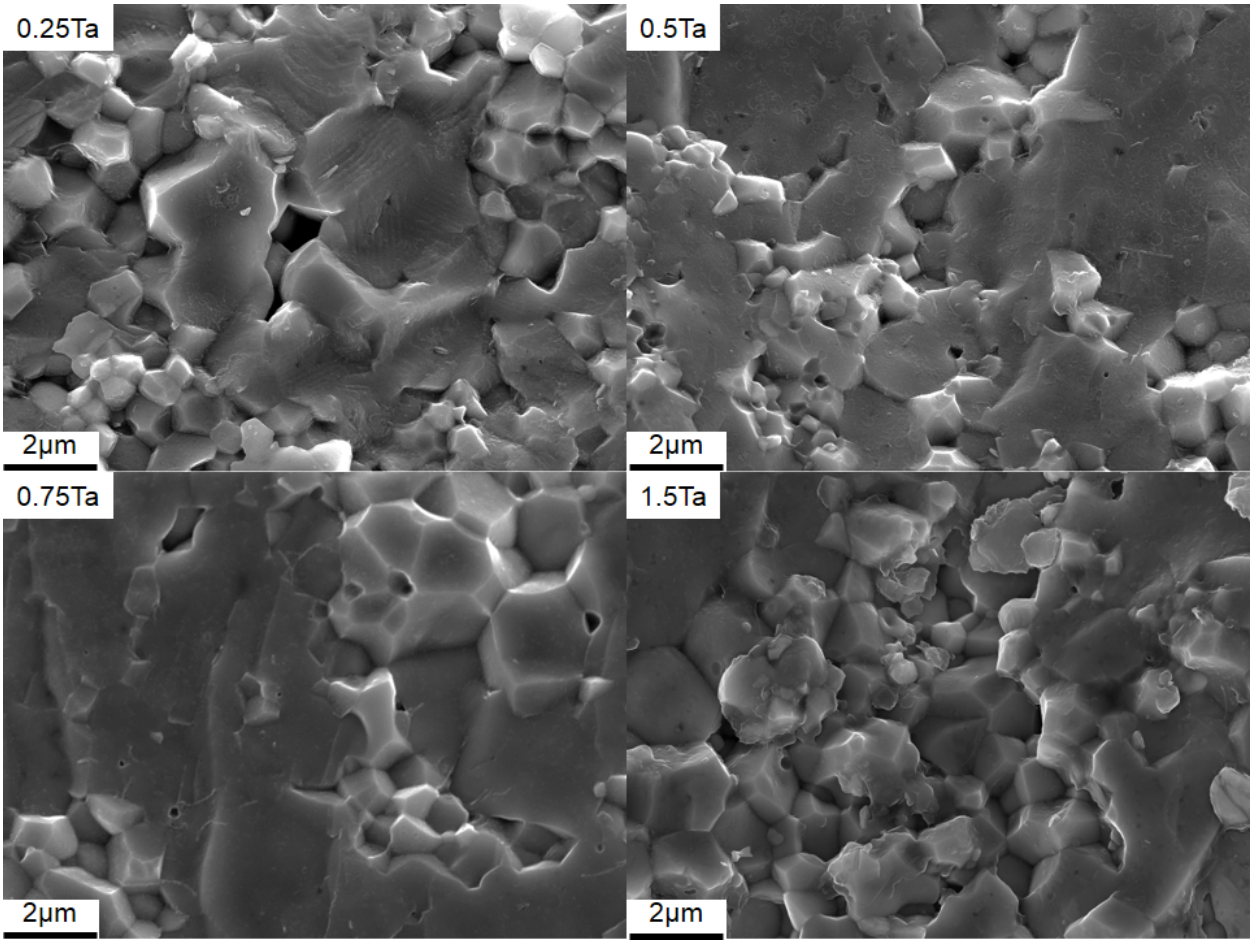

Figure 5.4: Secondary electron SEM micrographs of the fracture surface of hot-pressed pellets of the compositional series $Li_{7-x}La_3Zr_{2-x}Ta_xO_{12}$ (x = 0.25, 0.5, 0.75, and 1.5)

Both samples had relatively dense microstructures (approximately 97 percent for both compositions) with similar microstructural features; an average grain size of 1.4 microns and a mixed inter- and transgranular fracture mode. The relatively dense micrographs, similar grain sizes, and fracture mode indicate that Ta – doped LLZO samples without Al can be consolidated close to the theoretical density without the use of a sintering aid. Striations were observed in some of the grains in the subcritically doped composition. Similar striations in tetragonal LLZO which was consolidated using the same technique have been reported previously [100]. These striations were

not present in any of the grains for the critically doped composition. It is believed the striations result from a twinning phenomenon as described by Wolfenstine *et al.* [100] and are an indicator of the tetragonal phase. Since these striations were only observed in some, but not all, of the grains of the subcritically doped composition, this is taken as evidence that the sample is a mixture of cubic and tetragonal phases. Since the subcritically doped composition appears to be a mixture of cubic and tetragonal phases in SEM, yet cubic in table top XRD, Raman spectroscopy was performed to further clarify the results.

5.2.1.3 Raman spectroscopy

The Raman spectra shown in Figure 5.4 were collected for every sample in the compositional series including an undoped tetragonal reference. The line represents the average intensity value of the 5 locations while the black region of varying width around the line represents the uncertainty in the intensity. Since there are many overlapping features in the Raman spectra and the sample analyzed was polycrystalline, deconvolution of the spectra is not possible and this analysis will be limited to qualitative observations. Preliminary investigations of the Raman spectra of LLZO have been reported by Tietz *et al.* [107] and the phonon density of states has been determined by our collaborators computationally. Several observations can be made from the Raman spectra in Figure 5.5.

First, there is an additional band near 750 cm^{-1} which appears and grows in intensity as more Ta is added to the system. Since it has been determined that the band near 650 cm^{-1} corresponds to

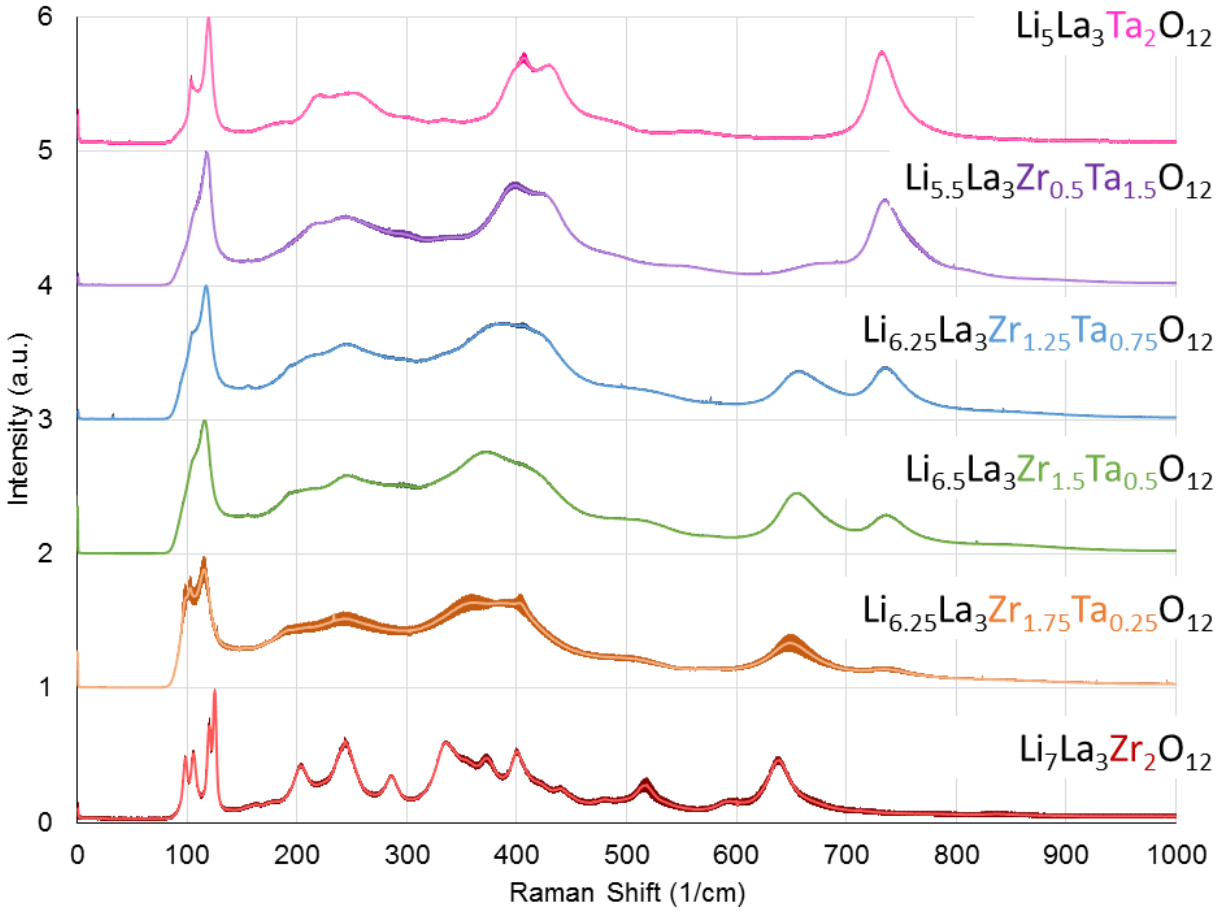

Figure 5.5: Raman spectra of the compositional series $Li_{7-x}La_3Zr_{2-x}Ta_xO_{12}$ (x = 0, 0.25, 0.5, 0.75, 1.5 and 2.0).

the breathing mode of the ZrO_6 octahedron, the appearance of the band at 750 cm^{-1} as Ta is added to the system suggests that this band corresponds to breathing mode of the TaO_6 octahedron.

Second, the ratio of the intensities of these two bands (approximately 650 cm^{-1} and 750 cm^{-1} for the Zr and Ta respectively) is a function of the Ta content in the garnet. Any uncertainty in the intensity of either of the bands individually near 650 cm^{-1} or 750 cm^{-1} means there is also an uncertainty in the ratio of these bands. Since the intensity plotted in Figure 5.5 is an average of 5 points across the sample and the Raman spot size samples a few grains per point, uncertainty in

the band intensity ratio suggests that the Ta content varies from point to point.

Third, for the subcritically doped composition in particular, there is considerable uncertainty in the intensity ratio of the bands near 650 cm^{-1} and 750cm^{-1}. As argued above, this suggests that there is variation in the Ta content at different points in the subcritical sample. This is in contrast to the critically doped, and all other compositions, where there is little uncertainty in the intensity ratio of the bands near 650 cm^{-1} and 750 cm^{-1}, suggesting a uniform Ta concentration throughout the sample. Since it is expected that the Ta content of the tetragonal phase would be different than that of the cubic phase, variation of the band intensity ratio in the subcritically doped composition would be consistent with the SEM analysis which suggested that the microstructure segregated into regions with tetragonal and cubic phases.

Fourth, if the compositional uncertainty in the subcritically doped sample is due to the microstructure phase segregation into cubic and tetragonal regions, then some direct evidence of the tetragonal phase should be present in the Raman spectra. A reduction of symmetry from cubic to tetragonal will result in splitting of the vibrational modes. Tietz *et al.* [107] showed that this is most evident in the bands near 110 cm^{-1}. Figure 5.6 shows a magnification of this region. It is evident that the subcritically doped composition (Ta = 0.25) is a superposition of the tetragonal reference and the critically doped spectra with clear splitting of the bands. This observation is especially evident when the uncertainty in the intensity is considered. This confirms that the subcritically doped sample is not single phase cubic but a mixture of cubic and tetragonal phases.

It is important to note that the spot size for the Raman analysis is approximately 3.5x that of the

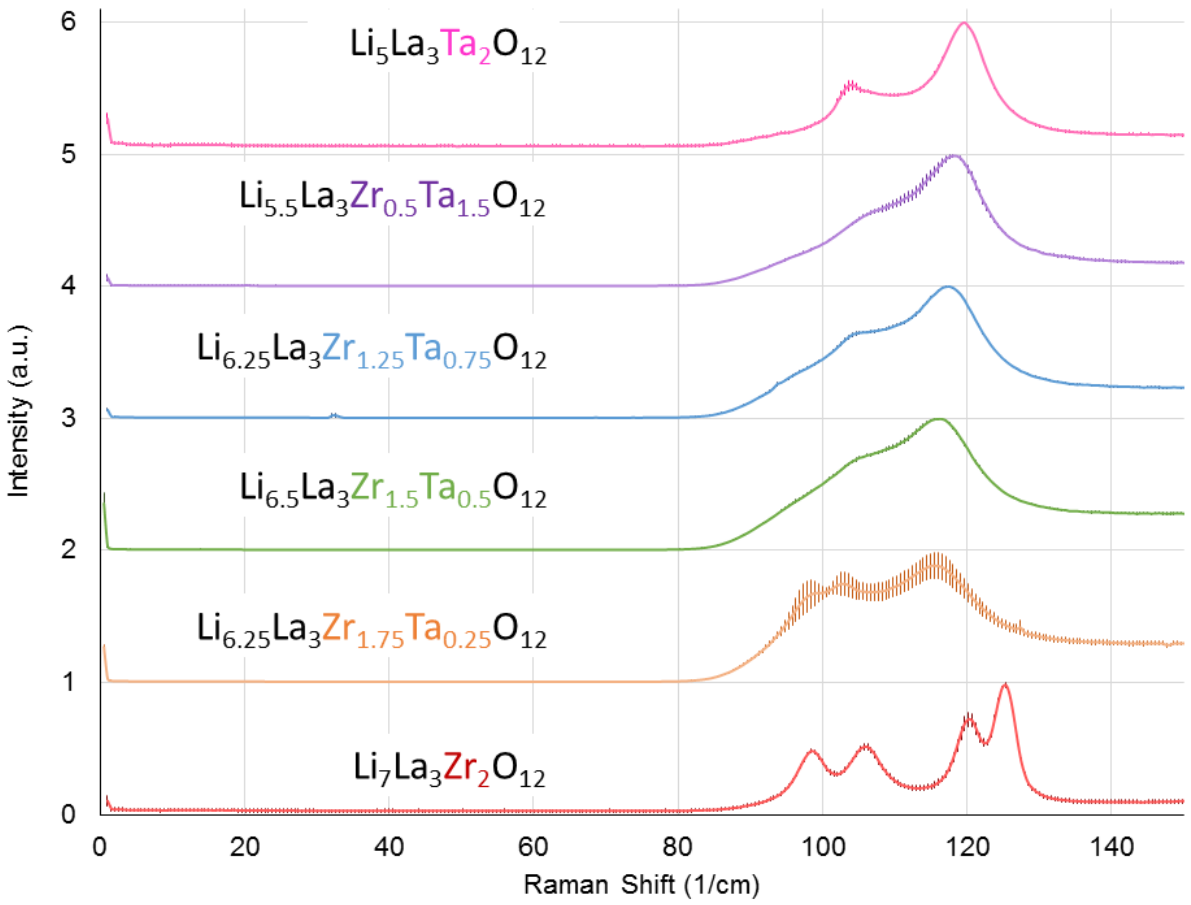

Figure 5.6: Magnification of the Raman spectra for the series $Li_{7-x}La_3Zr_{2-x}Ta_xO_{12}$ (x = 0, 0.25, 0.5, 0.75, 1.5 and 2.0) from 0 to 150 1/cm.

average grain size. As such, several grains are being sampled at each location and could include any impurities present. Indeed, trace impurities, likely with a perovskite structure, are visible in the XRD (marked in Figure 5.3). Since the intensity of these peaks are minor relative to that of the LLZO, the impurities are not expected to change the interpretation of the diffraction results. However, these impurities could manifest as additional bands in the Raman spectra. Since so many vibrational modes are active and overlapping for the LLZO and secondary phases, such as those with the perovskite like structure, could be present as well, it is difficult to assign the bands to

particular vibrational modes. As such, electrochemical impedance spectroscopy with equivalent circuit modeling was performed to help clarify the results of the Raman Spectroscopy and SEM analysis.

5.2.1.4 Electrochemical impedance spectroscopy

Since the density and grain size are similar, comparison of the transport properties is possible. As a consequence, EIS was performed on the sub- and critically doped compositions and equivalent circuit modeling of the data was performed. Figure 5.7 shows the Nyquist plot of the EIS data at room temperature, the equivalent circuit, and the modeled impedance response. EIS was also performed on the remaining compositions but will be discussed later.

In the model developed by Huggins [41], the capacitors were replaced with constant phase elements (CPEs) to account for any dispersion in the time constants. The complex impedance response of a single CPE is given by:

$$Z(\omega) = \frac{1}{Q(j\omega)^{\alpha}} \tag{5.1}$$

where $Z(\omega)$ is the frequency dependent impedance, ω is the frequency, j is the imaginary operator, Q is related to the capacitance and α is the ideality coefficient.

The values of Q for a CPE should be on the order of 10^{-12} $\frac{F}{cm^2}$ for the bulk and 10^{-9} $\frac{F}{cm^2}$ for the grain boundaries [41, 108]. The refined CPE Q values from the equivalent circuit modeling for the bulk and grain boundary processes for both compositions agree with the expected Q values for

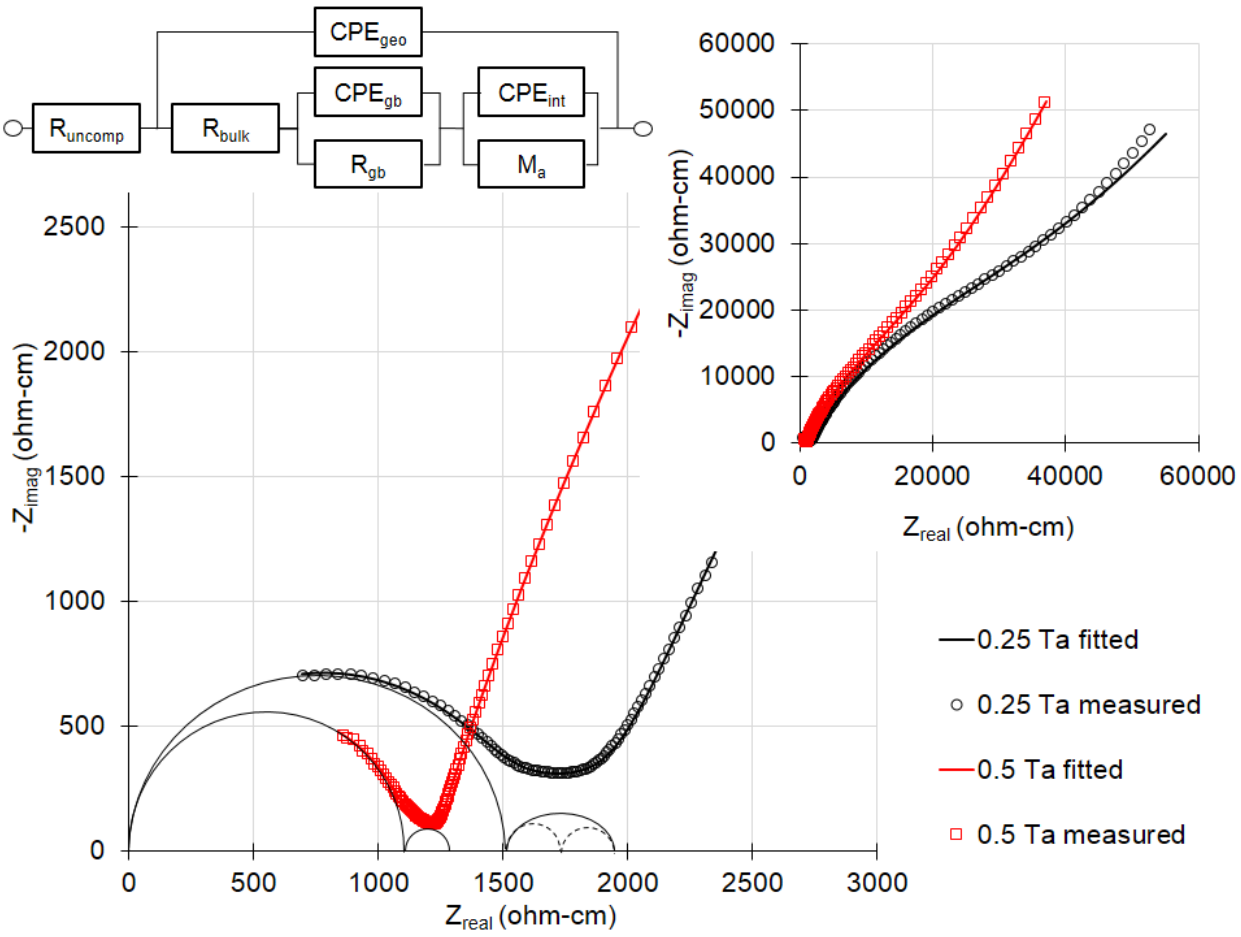

Figure 5.7: Nyquist plot of the complex impedance calculated from the EIS measurement performed at room temperature. The open symbols correspond to the experimental data and the solid lines are the fitted results of the equivalent circuit. The equivalent circuit model is shown in the top left. The inset shows the low frequency portion of the spectra. The semi-circles are included to help guide the eye.

these physical processes. The ideality of the CPE is represented by the coefficient α. The values for the ideality coefficient α were allowed to refine and settled to values near 1 for the bulk process for both the sub- and critically doped compositions. For the critically doped composition, the α value for the grain boundary feature also refined to nearly 1. However, for the subcritically doped composition, the α value was 0.78 and the resulting semi-circular feature in the Nyquist plot of the complex impedance was depressed. A depression in the mid-frequency regime has been observed

for tetragonal LLZO, which also exhibited a twinned microstructure [100]. Since twinning and grain boundaries are both two dimensional crystal defects, they have similar capacitances [109, 110]. Consequently, it is likely that the low α value for the mid-frequency CPE element for the subcritically doped composition is caused by the presence of more than one defect, namely the twinned tetragonal grains and grain boundaries. Analysis of the EIS data, therefore, suggests that the subcritically doped sample is not single phase cubic but a mixture of cubic and tetragonal phases. In contrast, the EIS data for the critically doped sample is as expected for purely cubic LLZO.

5.2.1.5 Neutron diffraction

The SEM, Raman, and EIS analysis do not support the observation made in the XRD that both the sub- and critically doped compositions are entirely cubic. It should be noted, however, that lab scale diffraction experiments can be resolution limited. Furthermore, XRD is insensitive to light elements and the tetragonal distortion results from ordering on the Li sublattice. Because of the sensitivity to Li, high resolution neutron diffraction (ND) and synchrotron x-ray diffraction was performed at the POWGEN beamline of the Spallation Neutron Source at Oak Ridge National Laboratory and at the 11-BM beamline of the Advance Photon Source (APS) at Argonne Nation Laboratory, respectively. Structural refinement of the subcritically doped compositions was attempted, however, due to the complexity of the phase segregation, quantitative phase analysis was not successful. As such, this analysis is treated qualitatively to confirm the observations made in

the SEM, Raman, and EIS analysis. The structures were successfully solved for the other compositions in the series and is discussed in detail later.

The ND patterns for the sub- and critically doped compositions are shown in Figure 5.8. The ND pattern of the critically doped composition, $(Li_{6.5}La_3Zr_{1.5}Ta_{0.5}O_{12})$, shows single peaks for each Bragg reflection, indicating that the phase is cubic. However, the ND pattern for the subcritically doped composition, $(Li_{6.75}La_3Zr_{1.75}Ta_{0.25}O_{12})$, clearly shows peak splitting. The insets in Figure 5.8 show the single (400) peak at a d-spacing of 3.23Å of the critically doped cubic LLZO composition and highlights the splitting of the sample peak for the subcritically doped composition into three peaks. Splitting of the peaks has been observed in undoped tetragonal compositions [100] and for subcritical Al doping on the Li site [42] in XRD. If only the tetragonal phase was present, then it would be expected that the single peak would split into two. However, since three peaks are observed, the high resolution ND supports the observations made in the SEM, Raman, and EIS analysis that the subcritically doped composition, $(Li_{6.75}La_3Zr_{1.75}Ta_{0.25}O_{12})$, is a mixture of cubic and tetragonal phases.

5.2.1.6 Summary of the tetragonal-to-cubic phase transformation

Before a more detailed analysis of the structure, including the Li site distribution, are correlations to the Li transport are made, the results of the cubic-to-tetragonal phase transformation are summarized here.

Since the table top XRD showed both the subcritically doped and the critically doped com-

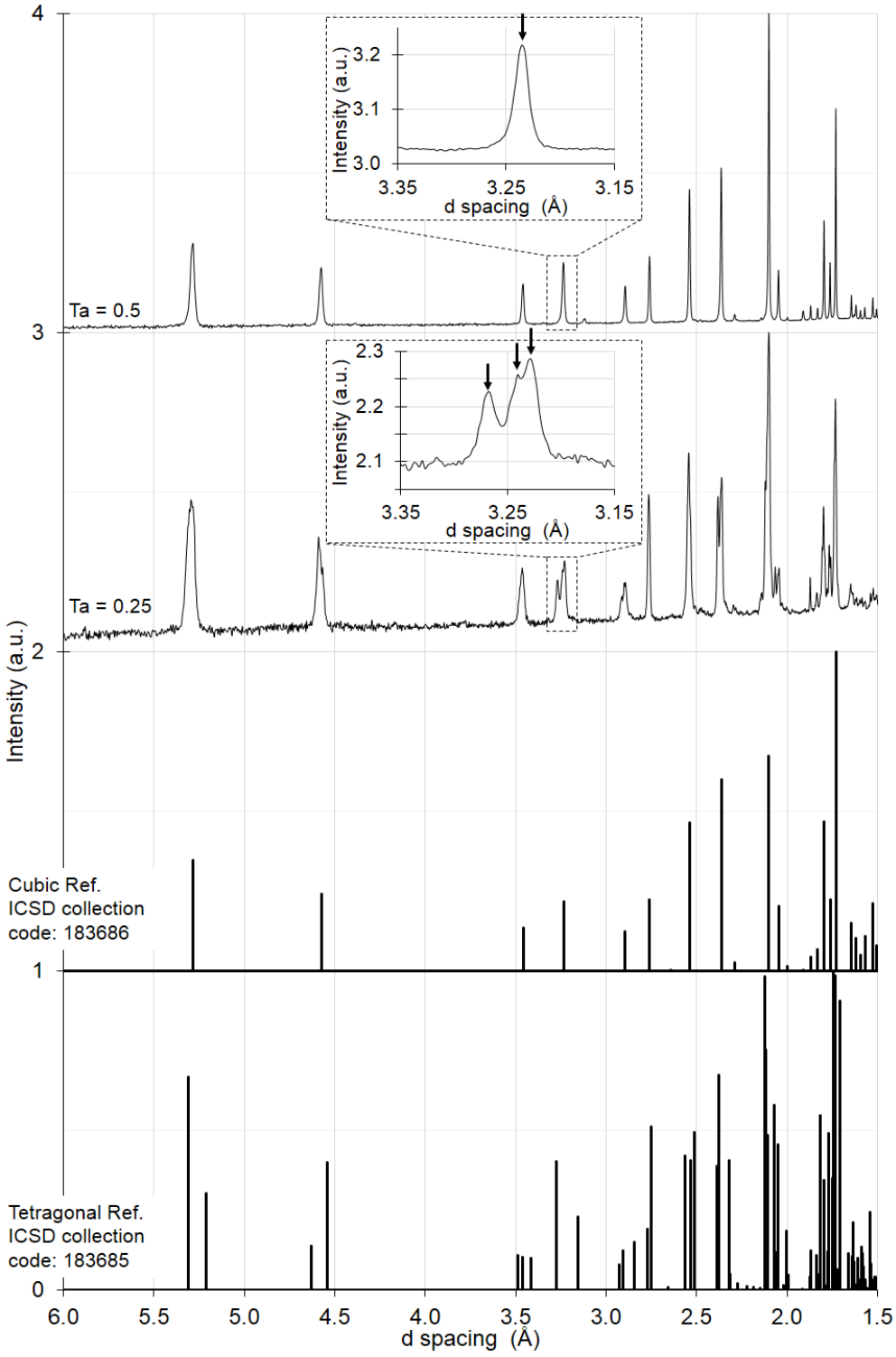

Figure 5.8: Neutron diffraction patterns of the composition $Li_{6.5}La_3Zr_{1.5}Ta_{0.5}O_{12}$, the composition $Li_{6.75}La_3Zr_{1.75}Ta_{0.25}O_{12}$, a cubic reference [40], and a tetragonal reference [40]. The insets highlight the (400) peak splitting observed.

positions as cubic, further materials characterization was performed. First, SEM analysis of the subcritically doped composition showed distinct striations in the microstructure where there were none in the microstructure of the critically doped composition. Second, Raman spectra of the subcritically doped composition showed variation in the Ta content from point to point and splitting of the vibrational modes where no variation in the Ta content nor splitting of the vibrational modes were observed in the critically doped composition. Third, EIS analysis showed a clear depression of the mid-frequency feature in the Nyquist plot of the subcritically doped composition and exhibited an α value of 0.78 for the CPE element where the mid-frequency feature for the critically doped composition was nearly ideal and exhibited an α value of 0.98 for the CPE. Finally, high resolution ND of the subcritically doped composition clearly showed splitting of the Bragg reflections while the critically doped composition did not. The results of the neutron diffraction data are in excellent agreement with the SEM, Raman, and EIS analysis and confirm that the subcritically Ta doped composition is a mixture of tetragonal and cubic phases while the critically Ta doped composition is entirely cubic. Furthermore, this is in agreement with experimental observations with Al doping [42] and combination density functional and molecular dynamics computations [99] which predict that a critical doping level of 0.4 – 0.5 mols of Li vacancies per formula unit is required to stabilize the cubic phase. The previous discrepancies between prediction and the experimental results for supervalent cation doping on the Zr site may be a result of Al incorporated during the processing steps or because of resolution limitations in table top x-ray diffractometers. Finally, this work suggests that SEM and Raman analysis can complement X-ray diffraction to

detect the presence of the tetragonal phase in compositions very near the critical doping level. This is important since nearly all of the highest conductivities have been reported at Li vacancy concentrations close to 0.4 - 0.5 mols of Li vacancies per formula unit. Furthermore, the tetragonal phase is known to have a significantly lower ionic conductivity and the presence of this phase in a composite microstructure is expected to decrease the over all conductivity.

5.2.2 Effect of Li concentration on the conductivity of cubic Ta doped LLZO

LLZO is also referred to as a "stuffed" garnet, because of its relatively high Li concentration (7 moles) compared to $Li_3La_3M_2O_{12}$. It is believed that the increase in Li concentration (i.e. carrier concentration) is one of the attributes that results in the higher conductivity compared to the other Li-based garnets. However, since the Li is distributed between two sites in the garnet structure, the Li site occupancy is another, less understood, parameter that affects the conductivity [111]. Likewise, to further improve the ionic conductivity, a detailed understanding of the Li site occupancy, as a function of Li concentration, is necessary. Furthermore, as the Li content is increased, the structure undergoes a reduction of symmetry from the high conductivity cubic to the lower conductivity tetragonal phase. The cubic to tetragonal phase transition was discussed in some detail in the above sections. Nevertheless, all of these structural affects must be explored in order to understand the system and identify new strategies to increase the conductivity. As such, when conductivity data is presented latter in this chapter as a function of dopant/Li concentration, it is assumed that compositions in the subcritically doped region are a mixture of cubic and tetrago-

Table 5.1: Summary of the results of the EIS equivalent circuit modeling and microstructure analysis.

	Nominal Ta content (mol)		
	0.5	0.75	1.5
RT total σ (mS/cm)	0.816	0.390	0.080
RT bulk σ (mS/cm)	0.903	0.405	0.103
$R_{gb}/(R_{bulk}+R_{gb})$	9%	4%	22%
Total Ea (eV)	0.431	0.452	0.561
Bulk Ea (eV)	0.435	0.443	0.536
Grain size (μm)	1.4	1.3	1.2
Relative density	97.8%	97.1%	97.3%

nal phases. Emphasis is primarily placed on the correlation of bulk, not total, conductivities to structural parameters such as the Li site occupancy.

5.2.2.1 Microstructural analysis

After hot pressing the powders, SEM analysis was performed on fracture surfaces to characterize the fracture mode, grain size, and porosity. Representative microstructures for each composition in the series $Li_{7-x}La_3Zr_{2-x}Ta_xO_{12}$ (x = 0.5, 0.75, and 1.5) are shown in Figure 5.4. All samples had relatively dense microstructures with grain sizes between 1.2 – 1.4 microns and exhibited a mixed intra- and transgranular fracture mode similar to previous reports [42]. The theoretical density was calculated using the refined diffraction data (shown below) and had relative densities >97 percent. The relative density and grain size for each composition is shown in Table 5.1.

The high relative densities, similar grain sizes, and fracture mode indicate that Ta - doped LLZO samples without Al can be consolidated close to full theoretical density without the use

of a sintering aid and that all the samples in this study had similar microstructures. Furthermore, because the microstructural features (i.e. porosity and grain size) were similar among the samples, comparison of the bulk transport properties between compositions is possible.

5.2.2.2 Electrochemical impedance spectroscopy

Electrochemical Impedance Spectroscopy (EIS) was performed as a function of temperature. For this work, the EIS data were modeled using a modified equivalent circuit proposed by Huggins [41] as described in Chapter 3 section 3.2.

Figure 5.9 shows a representative Nyquist plot of the EIS data for composition $Li_{6.5}La_3Zr_{1.5}Ta_{0.5}O_{12}$ at room temperature, the equivalent circuit and the modeled impedance response. The salient features are labeled with their characteristic frequencies and semi-circles are included to help guide the eye. It should be noted that because of the relatively high frequencies required to capture the full EIS spectrum, not all of the temperature points could be modeled. It can be seen in Figure 5.9 that even at room temperature, the characteristic frequency for the bulk response does not occur until >12 MHz (as estimated by extrapolation of the modeled impedance response to higher frequencies). Thus, the Arrhenius plot of the bulk conductivities (Figure 5.10) explicitly excludes points at elevated temperature which could not modeled with certainty. Of the spectra that could be modeled, excellent equivalent circuit fits were achieved. The entire impedance spectra were normalized to the bulk sample geometry before the equivalent circuit modeling was performed. The constant phase elements (CPE) used in the model were observed to behave nearly

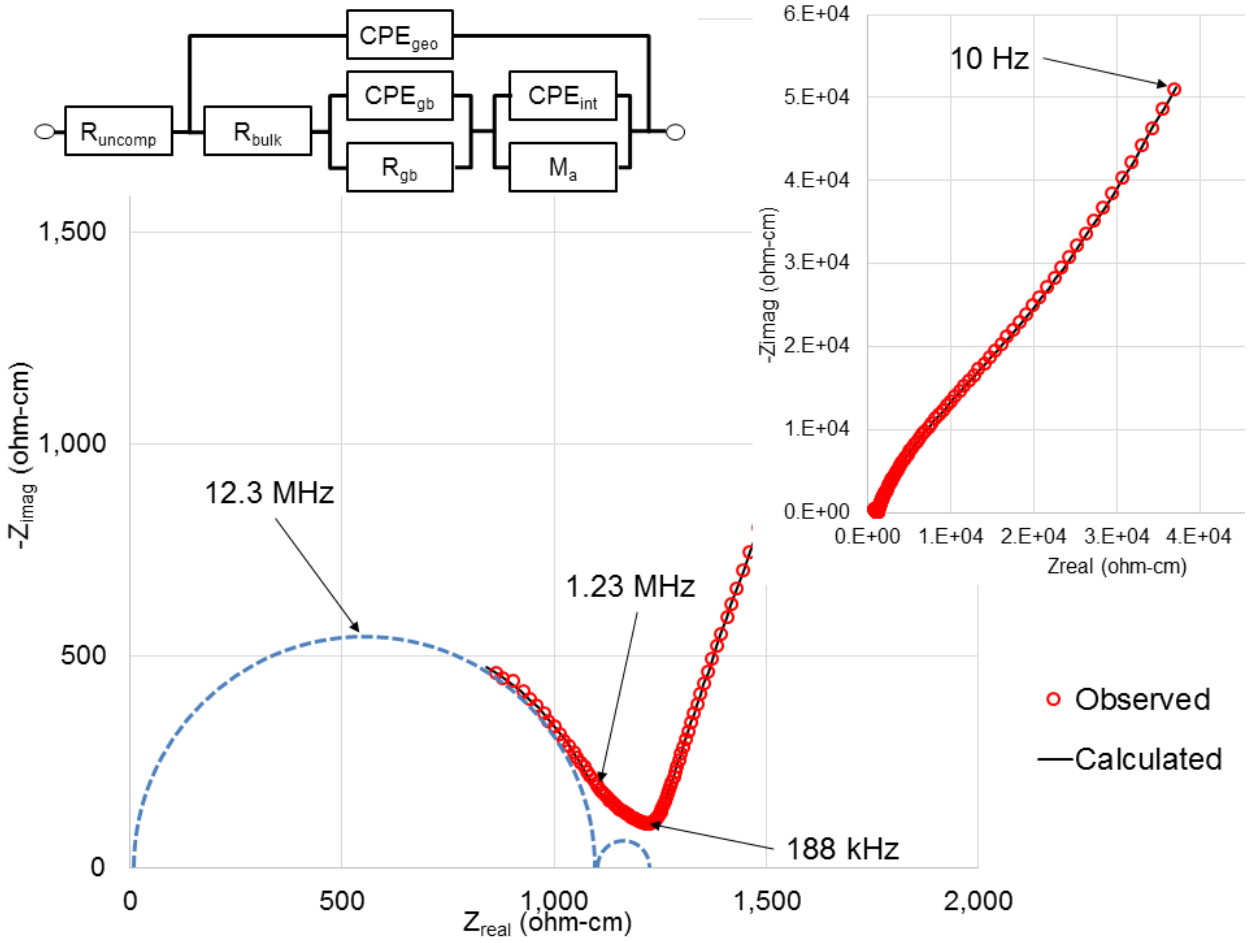

Figure 5.9: Ionic transport data obtained from electrochemical impedance spectroscopy in Ta doped LLZO. Representative Nyquist plot (for x = 0.5 Ta), equivalent circuit used to model the data, and the calculated impedance response. The salient features are labeled with their characteristic frequencies and semi-circles are included to help guide the eye.

ideally as is evident by α coefficients refining to values ranging between 0.92 and 1.0. Because of the configuration of the elements in this model, it is impossible to calculate equivalent capacitances for the CPEs. However, since the CPEs exhibited nearly ideal behavior, the Q value can be taken as a capacitance as a first approximation. Two conduction processes (i.e. bulk and grain boundary) are observed in the high frequency regime of the Nyquist plot shown in Figure 5.9. The values of Q for the CPEs for the grain and grain boundary processes are $10^{-11}\ \frac{F}{cm^2}$ and $10^{-8}\ \frac{F}{cm^2}$ for the bulk and

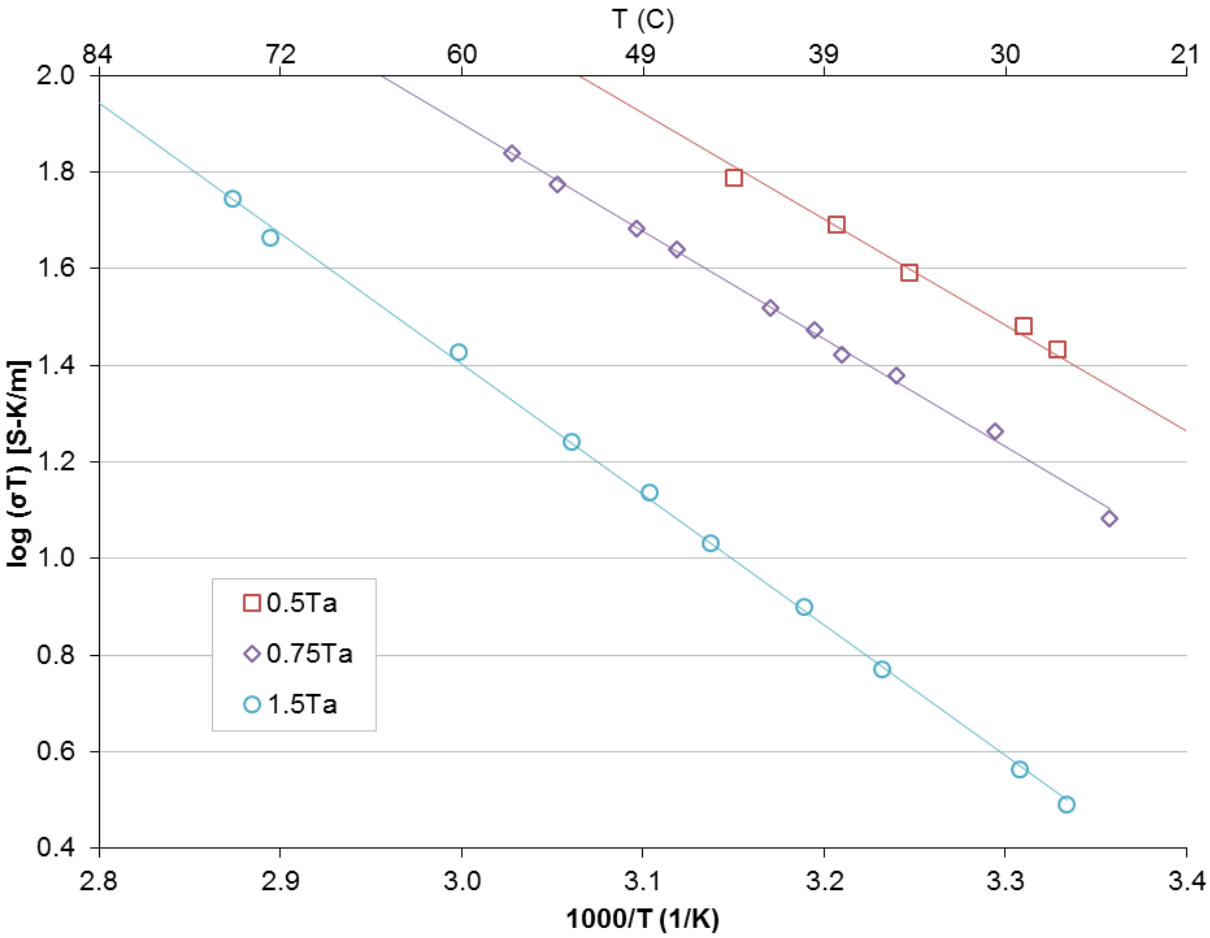

Figure 5.10: Arrhenius plot of the bulk, not total, conductivity of the compositional series as determined form the equivalent circuit modeling.

the grain boundaries, respectively, which is in excellent agreement with what is expected [41, 108]. The Q value for both the bulk and grain boundary processes did not appreciably change with temperature for all samples.

Figure 5.10 is an Arrhenius plot of the bulk conductivities extracted from the impedance spectra by the equivalent circuit modeling. It can be seen that the sample at the critical doping level to stabilize the cubic phase, with nominal composition x = 0.5 Ta, exhibited the highest conductivity for all temperatures. This agrees well with what has been reported in the literature [101, 112].

Table 5.1 summarizes the extracted values from the Nyquist and Arrhenius data. Based on the data in Table 5.1, several observations can be made. First, the bulk and total conductivities are similar. This is expected since the presence of significant transgranular fracture observed in the SEM micrographs (Figure 5.4) indicates grain-to-grain adhesion. Second, the activation energies of >0.4 eV observed are higher than what has been reported for samples that contain Ta and Al [71,101]. These values are higher than what has been reported previously for Ta containing LLZO, however, in recent Ta-stabilized LLZO series made without Al, the activation energies of this work agree well [112]. It has been demonstrated that LLZO samples stabilized with only Al have low activation energies on the order of 0.26 – 0.34 eV [42, 43]. It is possible that the Al in these Ta-stabilized LLZO literature references is lowering the activation energy. However, the conductivities of samples doped with Al also have 1/2 to 1/3 of the conductivities of samples doped with Ta at room temperature. How Al lowers the activation energy, yet the conductivity is not increased, is unclear at this time. However, it is possible that the Al residing on the Li sublattice is responsible for the behavior observed.

5.2.2.3 Synchrotron x-ray and neutron powder diffraction

Synchrotron x-ray and neutron powder diffraction were performed on the series $Li_{7-x}La_3Zr_{2-x}Ta_xO_{12}$ (x = 0.25, 0.5, 0.75, and 1.5). As mentioned in above, the subcritically doped sample, with composition $Li_{6.75}La_3Zr_{1.75}Ta_{0.25}O_{12}$, was a mixture of tetragonal and cubic phases and Rietveld refinement of the diffraction patterns was not successful. As such, even

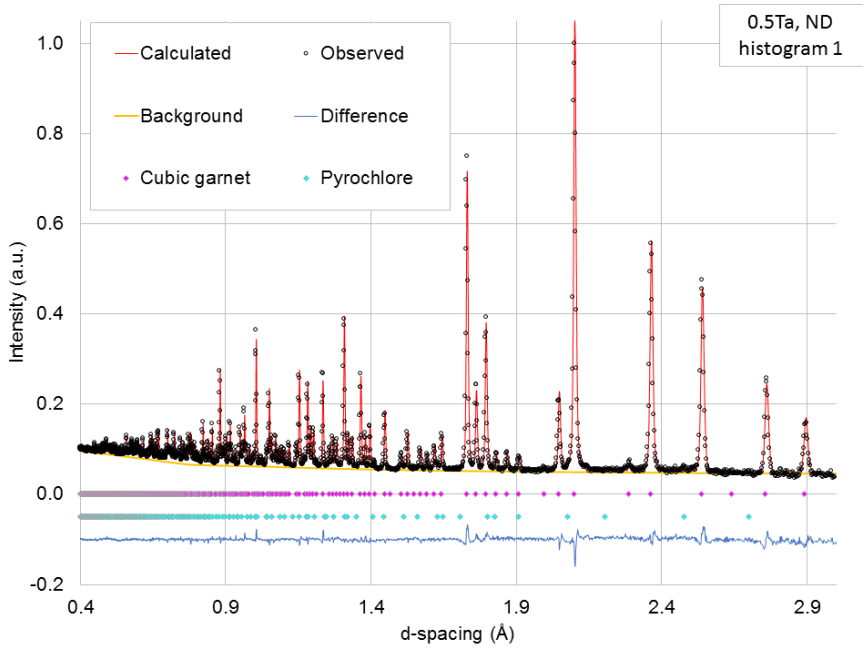

Figure 5.11: Refinement of neutron diffraction data after convergence for the sample with composition of $Li_{6.5}La_3Zr_{1.5}Ta_{0.5}O_{12}$.

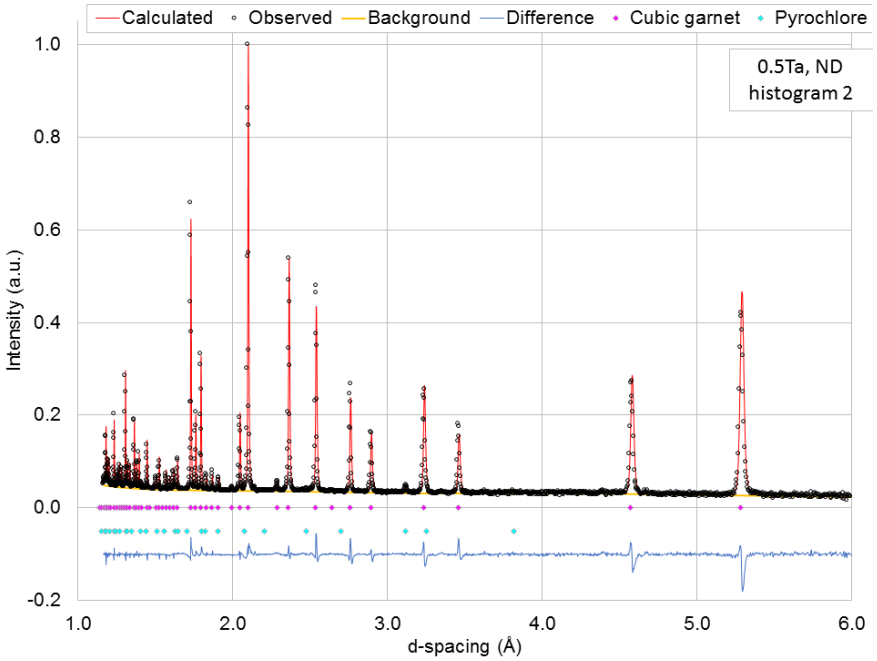

Figure 5.12: Refinement of neutron diffraction data after convergence for the sample with composition of $Li_{6.5}La_3Zr_{1.5}Ta_{0.5}O_{12}$.

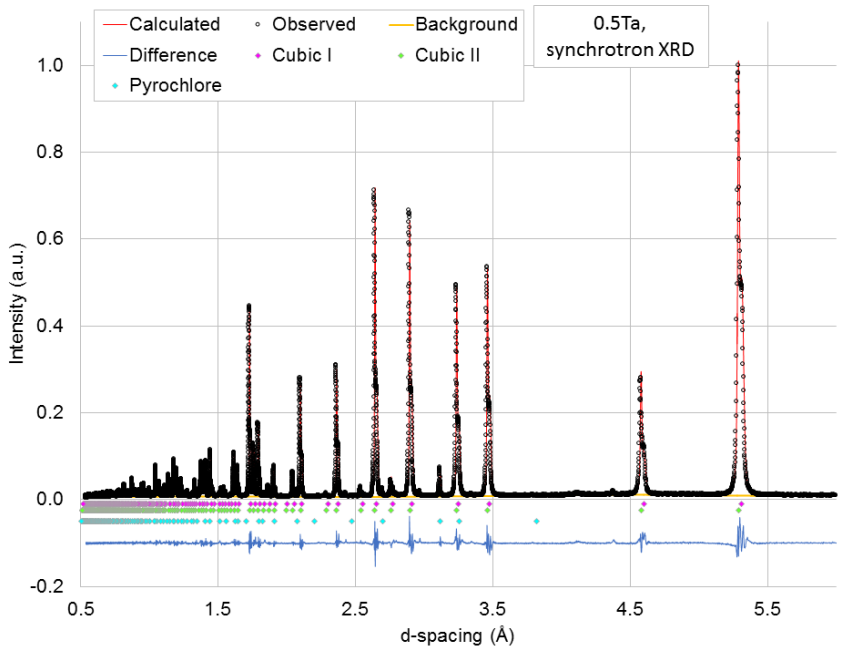

Figure 5.13: Refinement of synchrotron x-ray diffraction data after convergence for the sample with composition of $Li_{6.5}La_3Zr_{1.5}Ta_{0.5}O_{12}$.

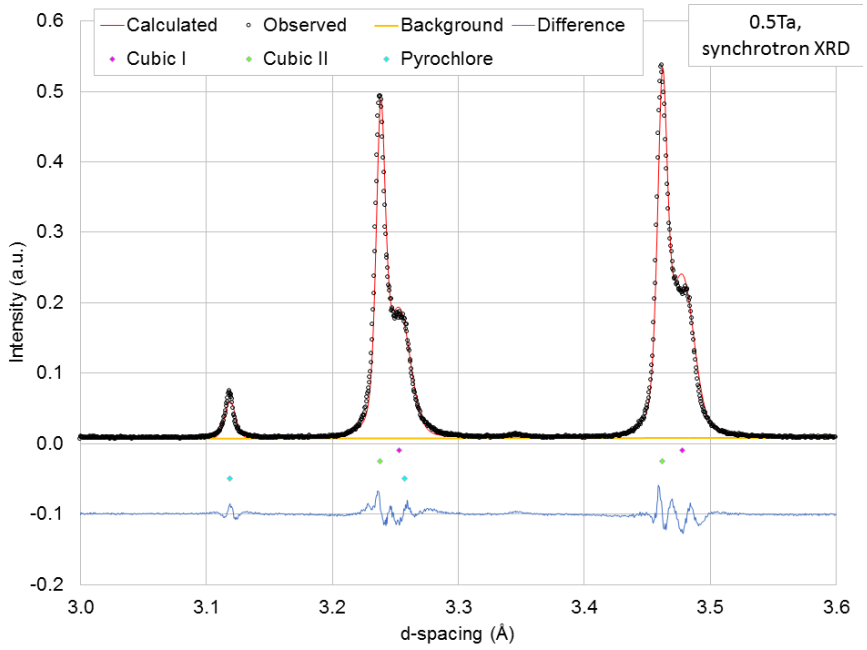

Figure 5.14: Magnified region of the refinement of synchrotron x-ray diffraction data after convergence for the sample with composition of $Li_{6.5}La_3Zr_{1.5}Ta_{0.5}O_{12}$ highlighting the two cubic phases observed.

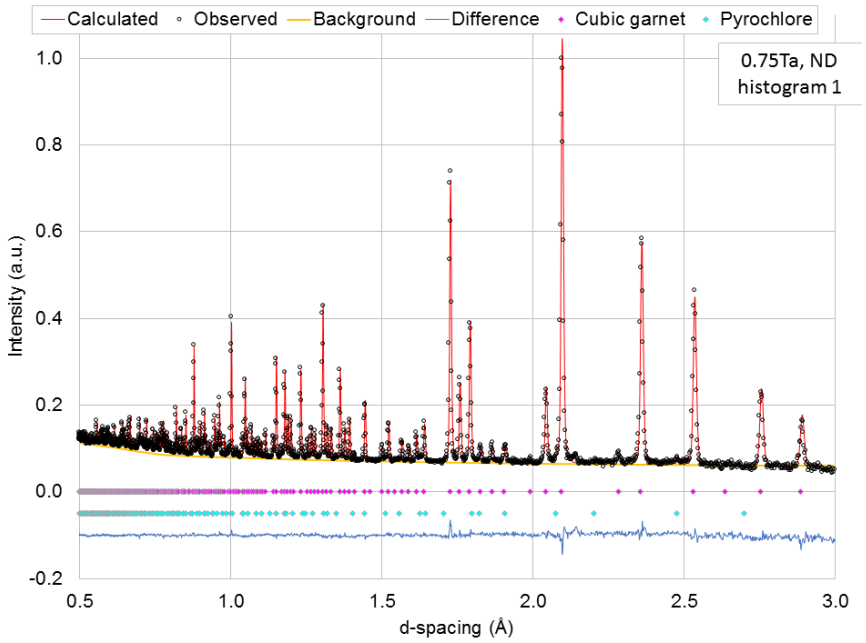

Figure 5.15: Refinement of neutron diffraction data after convergence for the sample with composition of $Li_{6.25}La_3Zr_{1.25}Ta_{0.75}O_{12}$.

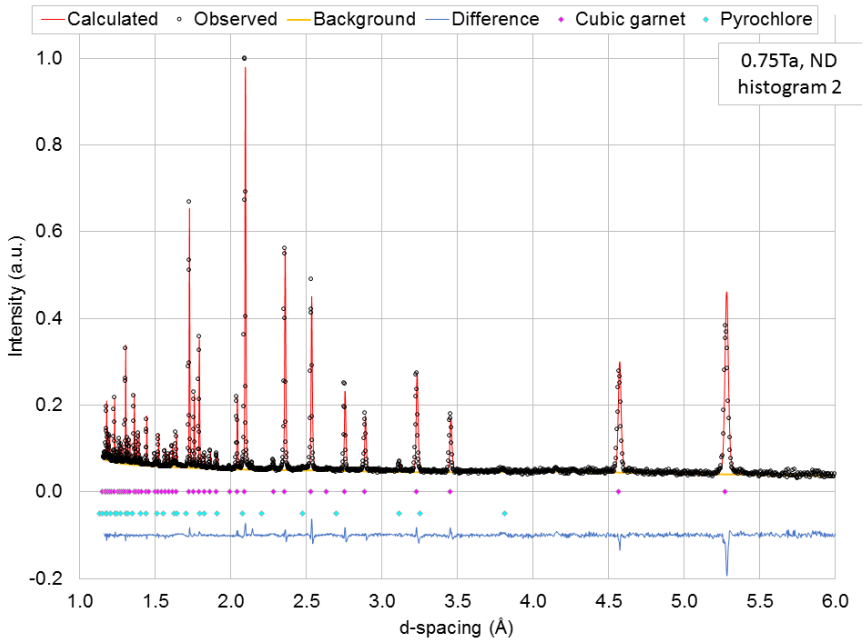

Figure 5.16: Refinement of neutron diffraction data after convergence for the sample with composition of $Li_{6.25}La_3Zr_{1.25}Ta_{0.75}O_{12}$.

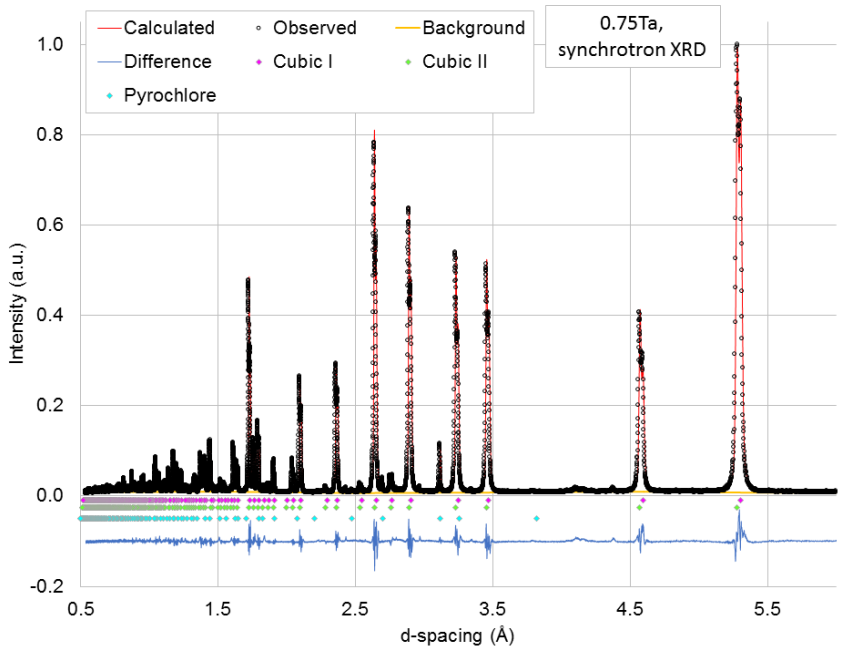

Figure 5.17: Refinement of synchrotron x-ray diffraction data after convergence for the sample with composition of $Li_{6.25}La_3Zr_{1.25}Ta_{0.75}O_{12}$.

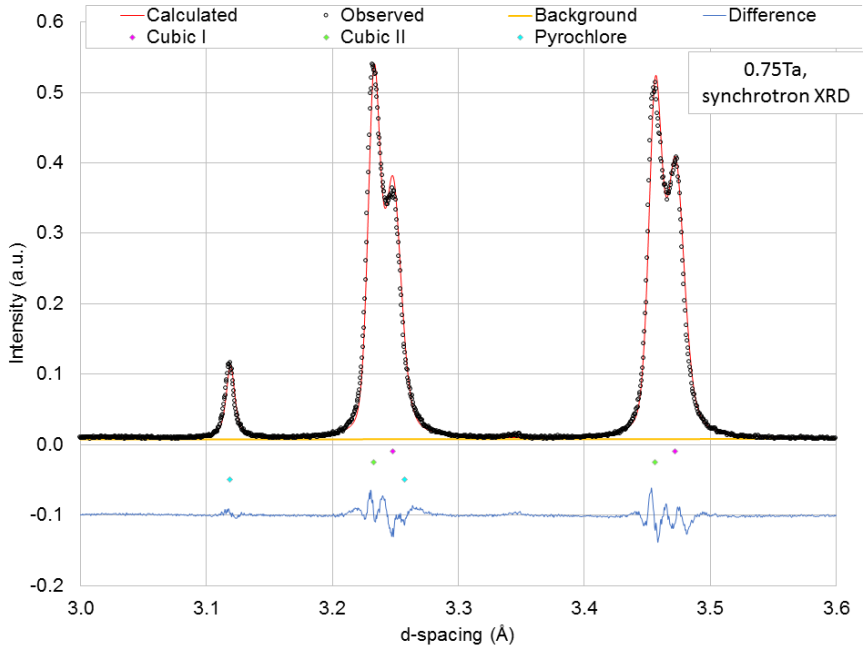

Figure 5.18: Magnified region of the refinement of synchrotron x-ray diffraction data after convergence for the sample with composition of $Li_{6.25}La_3Zr_{1.25}Ta_{0.75}O_{12}$ highlighting the two cubic phases observed.

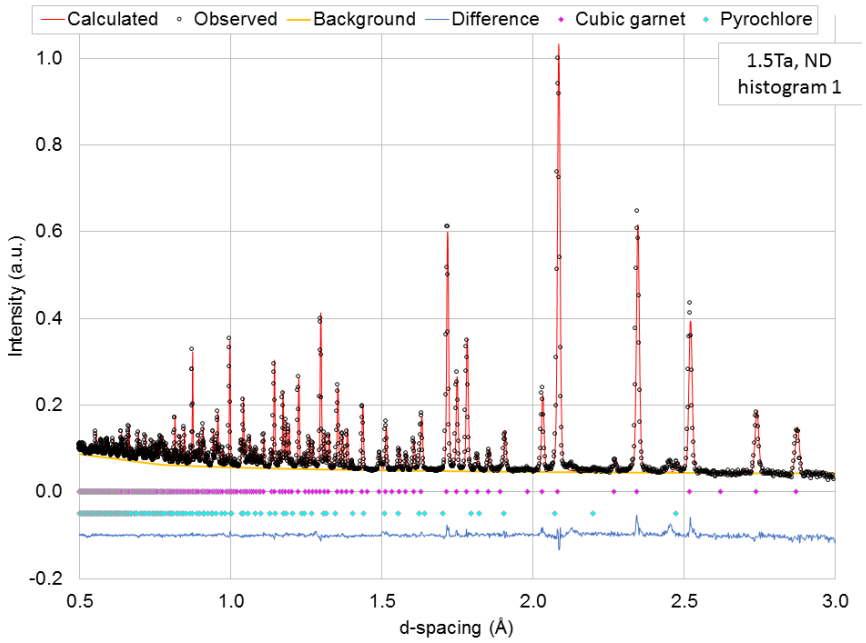

Figure 5.19: Refinement of neutron diffraction data after convergence for the sample with composition of $Li_{5.5}La_3Zr_{0.5}Ta_{1.5}O_{12}$.

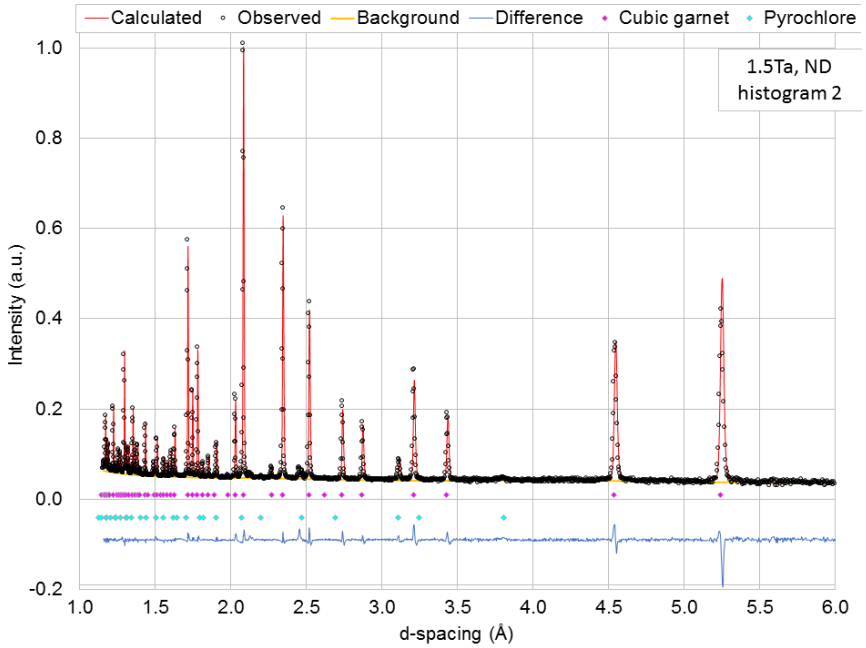

Figure 5.20: Refinement of neutron diffraction data after convergence for the sample with composition of $Li_{5.5}La_3Zr_{0.5}Ta_{1.5}O_{12}$.

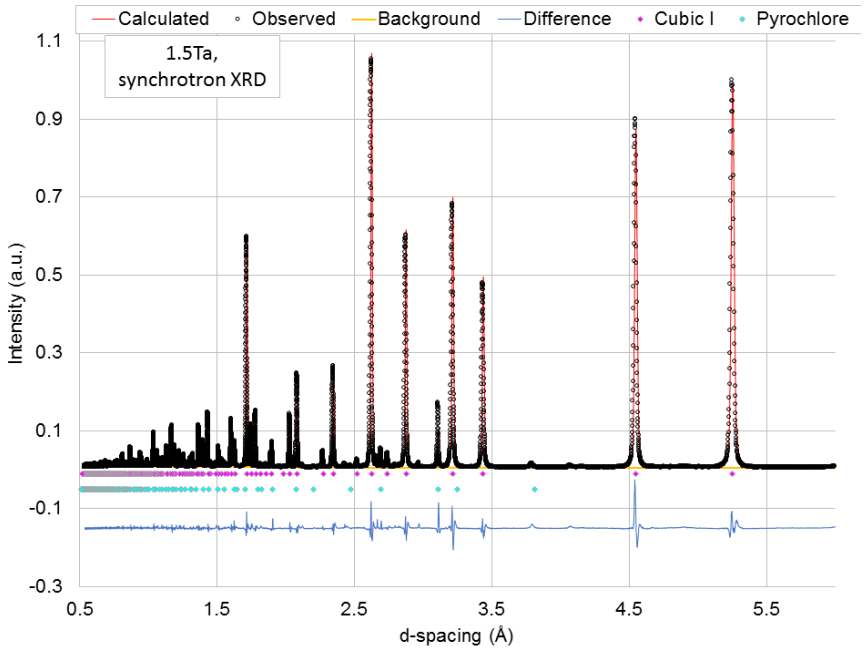

Figure 5.21: Refinement of synchrotron x-ray diffraction data after convergence for the sample with composition of $Li_{5.5}La_3Zr_{0.5}Ta_{1.5}O_{12}$.

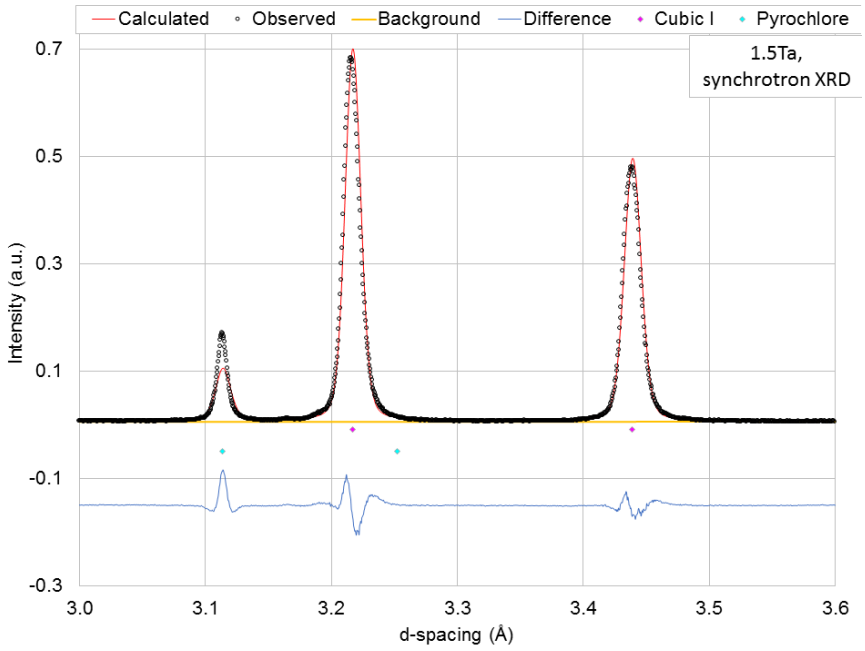

Figure 5.22: Magnified region of the refinement of synchrotron x-ray diffraction data after convergence for the sample with composition of $Li_{1.5}La_3Zr_{0.5}Ta_{1.5}O_{12}$. Unlike the other compositions, a single cubic phase was observed.

Table 5.2: Rietveld structural refinement results for $Li_{6.5}La_3Zr_{1.5}Ta_{0.5}O_{12}$.

Name	Site	Site Occupancy	X	Y	Z	100xU$_{eq}$ (Å^2)
Li1	24d	0.412(9)	3/8	0	1/4	2.24(15)
Li2	96h	0.375(4)	0.0972(4)	0.6868(4)	0.5790(4)	1.79(11)
La	24c	1.000	1/8	0	1/4	1.012(7)
Zr	16a	0.738(2)	0	0	0	0.806(10)
Ta	16a	0.247(2)	0	0	0	0.806(10)
O	96h	1.000	-0.0317(5)	0.0536(5)	0.1488(5)	1.467(6)

Space group Ia-3d (No. 230); a=12.9307(4) Å; R_{wp} = 3.19, χ^2 = 6.31, R_p = 5.36

Table 5.3: Rietveld structural refinement results for $Li_{6.25}La_3Zr_{1.25}Ta_{0.75}O_{12}$.

Name	Site	Site Occupancy	X	Y	Z	100xU$_{eq}$ (Å^2)
Li1	24d	0.450(8)	3/8	0	1/4	2.61(13)
Li2	96h	0.354(4)	0.0979(4)	0.6868(4)	0.5785(4)	1.94(11)
La	24c	1.000	1/8	0	1/4	0.960(6)
Zr	16a	0.596(2)	0	0	0	0.666(8)
Ta	16a	0.384(2)	0	0	0	0.666(8)
O	96h	1.000	-0.0313(4)	0.0529(5)	0.1481(5)	1.401(6)

Space group Ia-3d (No. 230); a=12.9089(30) Å; R_{wp} = 2.37, χ^2 = 2.996, R_p =4.59

though the conductivity data is available, the corresponding structural information, such as Li site occupancy, is not. Since X-ray diffraction is not sensitive to light elements such as Li with low Z numbers and Ta and Zr have similar neutron scattering cross-sections, both X-ray and neutron powder diffraction were performed. The experimental neutron and synchrotron diffraction patterns and calculated fits after convergence are shown in Figures 5.11 - 5.22. This complimentary approach allowed for accurate structural refinement [113], the results of which are shown in Tables 5.2 - 5.4.

Figure 5.23 plots the lattice parameter vs. nominal Ta content constructed from the structural refinement data and relevant literature values. The literature references included in Figure 5.23 correspond to other Zr/Ta garnet solid solutions of similar compositions [40, 43, 101, 114]. As

Table 5.4: Rietveld structural refinement results for $Li_{5.5}La_3Zr_{0.5}Ta_{1.5}O_{12}$.

Name	Site	Site Occupancy	X	Y	Z	100xU$_{eq}$ (Å^2)
Li1	24d	0..646(8)	3/8	0	1/4	2.77(10)
Li2	96h	0.262(4)	0.1006(5)	0.6862(5)	0.5781(5)	1.84(14)
La	24c	1.000	1/8	0	¼	1.030(7)
Zr	16a	0.197(2)	0	0	0	0.552(8)
Ta	16a	0.754(2)	0	0	0	0.552(8)
O	96h	1.000	-0.0302(4)	0.0514(4)	0.1458(4)	1.301(5)

Space group Ia-3d (No. 230); a=12.8363(33) Å; R_{wp} = 2.88, χ^2 = 4.37, R_p = 5.11

expected, the Zr/Ta solid solution is following Vegard's Law where the lattice parameter is linearly changing with increasing substitution. Furthermore, the lattice parameter decreases with increased Ta substitution which is expected since the Ta^{5+} ion in 6-fold coordination is smaller than the Zr^{4+} with the same coordination (78 pm and 86 pm, respectively) [106]. However, it is apparent in the high resolution synchrotron x-ray diffraction that the system does not form a continuous solid solution from the Zr to the Ta end member (Figure 5.14, 5.18, 5.22). In all compositions except for the Ta = 1.5, two cubic phases were present with slightly different Ta contents and lattice parameters. This is the first known observation of this in the Ta substituted LLZO but has been observed previously in Al substituted LLZO [115]. Since the two phases were not resolvable in neutron diffraction (even though it is also a high resolution beamline), the average Ta and Zr contents for each composition was found using the synchrotron x-ray diffraction and fixed in the structural refinements for the neutron diffraction.

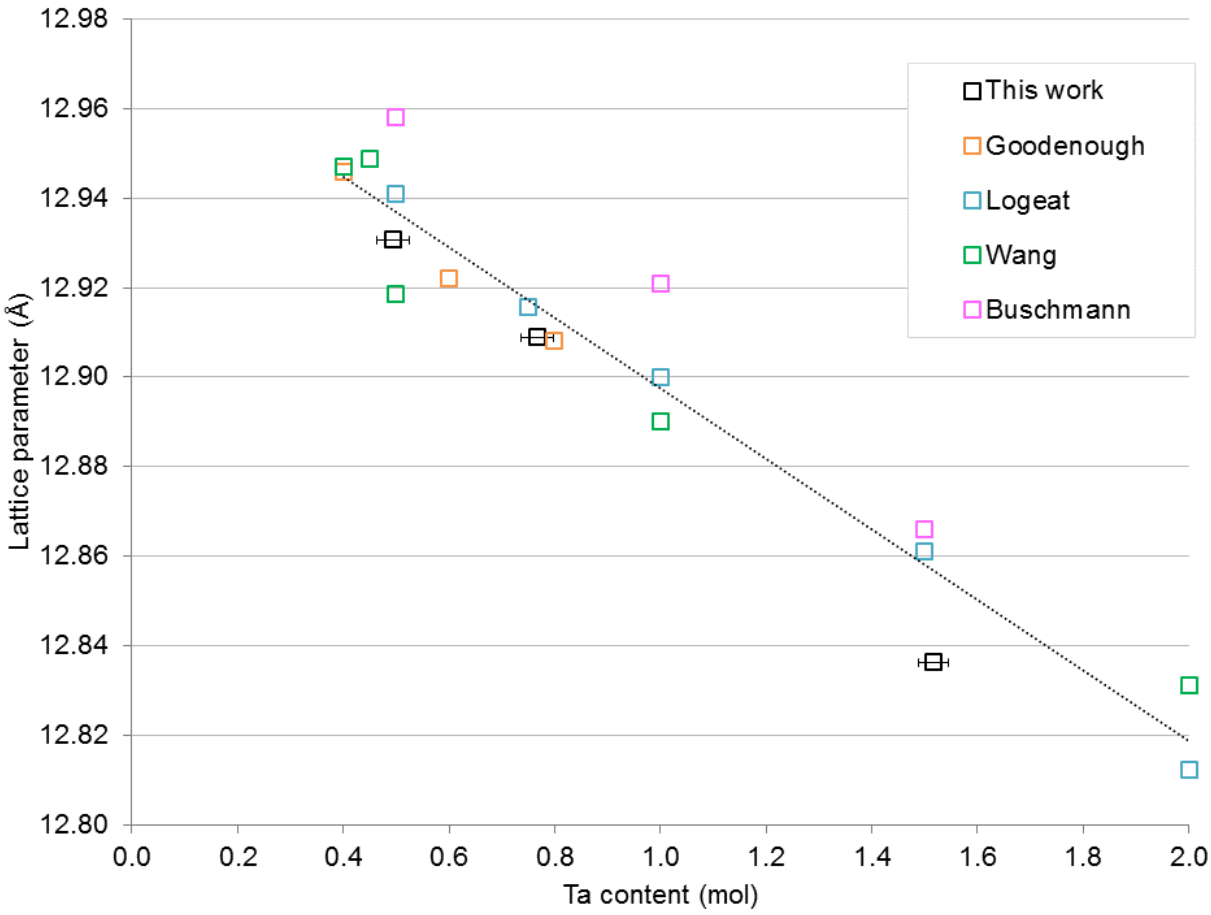

Figure 5.23: The lattice parameter vs. Ta content of this work compared to other studies available in the literature [40, 43, 101, 114]. The dotted line in a linear fit to all the data on the plot and is included to help guide the eye.

5.2.2.4 Li site occupancy

Before more detailed analysis of the diffraction and conductivity data is discussed a note should be made regarding this work. Collectively, Figures 5.9 – 5.23 are included in this report not because conclusions are drawn from them directly but to clearly highlight the following: i) all the compositions are high quality and comparable to what is available in the literature, ii) all the microstructures are comparable, iii) all the characterization was performed carefully with every

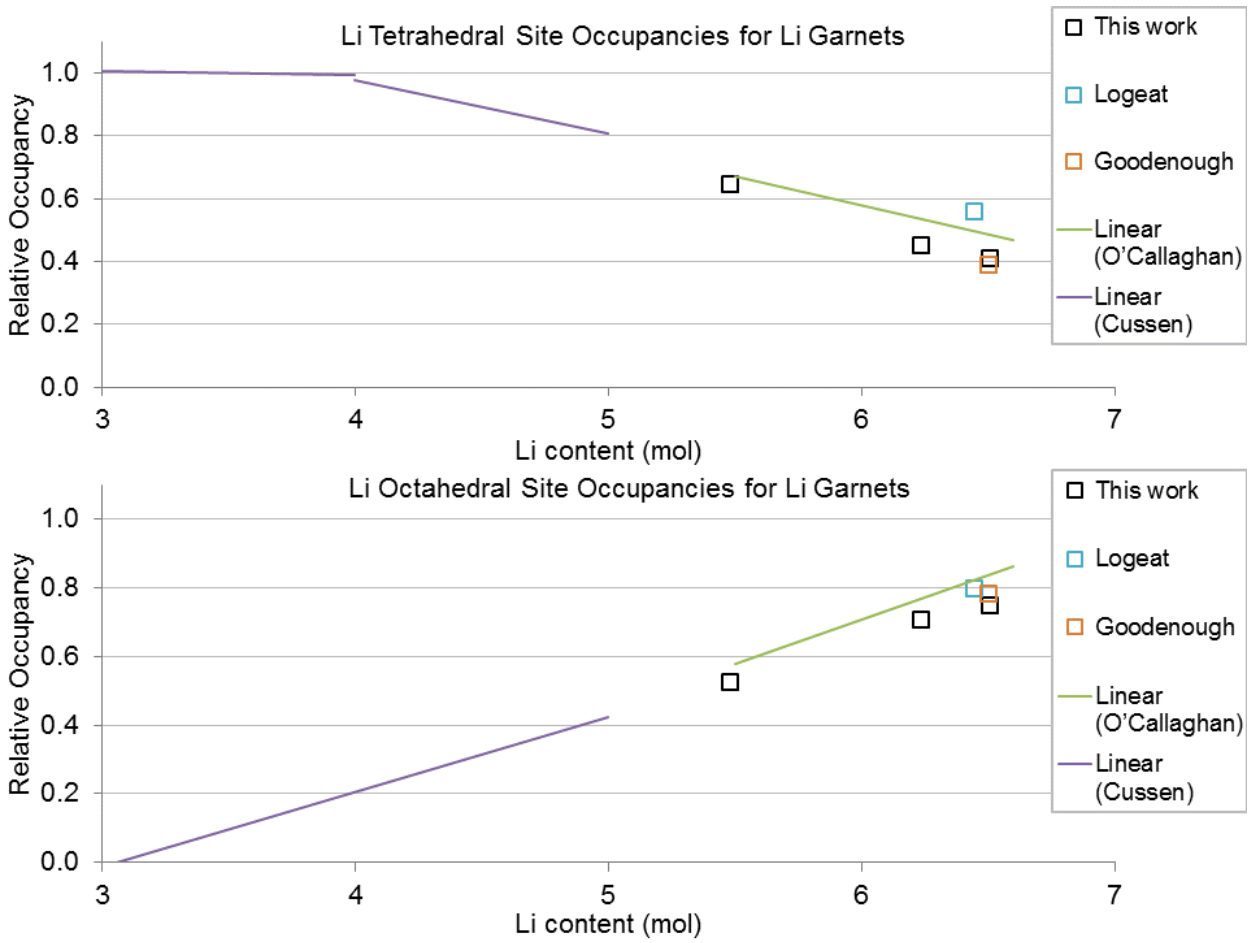

Figure 5.24: Plot of the tetrahedral and octahedral Li site occupancies vs. Li content compared to data available in the literature [40, 85–88, 90, 92, 101].

best practice learned through previous work with this system (such as minimization of H+ and the elimination of Al contamination) used throughout. This is important to note because the system is complex and any unaccounted for variables (such as a difference in porosity, a difference in the volume fraction of grain boundaries, or adventitiously included dopants) could confound the analysis and results. Since these variables are consistent between the compositions explored in this work, values for the bulk conduction process could be extracted with some confidence and a direct comparison can be made with the structural parameters.

The Li site occupancies have been refined for this compositional series from the diffraction data are summarized in Figure 5.24. The results were compared to literature values for similar compositional series and for garnets based on other formulations with lower Li contents. All literature references shown in Figure 5.24 are results from neutron diffraction. The linear fits to the Cussen *et. al.* and O'Callaghan *et al.* data are garnet structures of a variety of formulations based on W, Te, Sb, and Ta with lower Li contents [85–88, 90, 92]. The Logeat *et al.* and Goodenough *et al.* data sets are for Zr/Ta solid solutions similar in composition to the series explored in this work [40, 101]. For the data of this work, uncertainties were calculated but were smaller than the symbol and have been omitted.

In cubic LLZO there are two Li coordination environments; tetrahedral and octahedral coordination with oxygen [105, 116]. There are two ways to define the site of the octahedrally coordinated Li. The first is with a single symmetric Wyckoff position 48g. The second is with a displaced Wyckoff positions referred to as 96h sites. The 96h position represents the splitting of the proposed 48g site into two off-center 96h sites each oppositely adjacent to the 48g site, where only one of 96h sites can be filled at any one time due to Li-Li coulombic repulsion. Earlier structural models used the 48g position or a combination of the 48g and 96h, however, subsequent studies have pointed to the 96h position as being a more accurate description of the octahedrally coordinated Li [40, 98, 103, 105, 116, 117]. In order to compare structural models together, an octahedral occupancy for the Li has been defined as $Li_{octahedral} = 2 * Occ_{Li96h} + Occ_{Li48g}$. In this work, where only the 96h site was considered, the octahedral Li occupancy was calculated by

$Li_{octahedral} = 2 * Occ_{Li96h} + 0$. As seen in Table 5.2 - 5.4, modeling the experimental data with the octahedrally coordinated Li described only by the 96h site resulted in excellent fits with low χ^2 values in the range of 3 – 6, and R_wp values as low as approximately 2.5 being achieved. This indicated that the structural results can be treated with more certainty.

Since the purpose of this study was to probe the Li environment directly with a technique which is sensitive to it (i.e. neutron diffraction) without the need for assumptions regarding the Li content, the Li stoichiometry was allowed to freely refine in the structural model without the imposition of charge balance. Charge imbalance was observed but oxygen vacancies could easily account for the difference seen and have, in fact, been proposed (but not discussed) in the literature previously [101]. The presence of a second crystal defect, besides what is purposefully introduced by the dopant, could be another, uncontrolled variable. Since the Li content is the conventional parameter used to discuss Li-ion conducting garnets, the influence of oxygen defects on the Li-ion transport in garnets deserves more investigation, if these defects are indeed present. Since the presence and role of other charge compensating defects, which could alter the Li content, is not resolved, the nominal Li content is used to discuss the results shown in Figure 5.24.

Accordingly, the general trend of the Li occupancy in the two coordination environments for the experimental series are in excellent agreement with reported literature values for garnets not only stabilized by Ta with Al [40, 101] present but also for the garnets of significantly different formulations investigated by Cussen *et al.* and O'Callaghan *et al.* [85–88, 90, 92]. As the Li content is increased, the tetrahedrally coordinated (24d) Li sites depopulate and the octahedrally coordinated

(96h) Li sites populate. This is significant because the 96h site is not normally populated in the garnet structure, yet the trend is obvious over a wide compositional range. Furthermore, NMR reports suggest that the ions occupying the 96h site are more mobile than those occupying the 24d site [118]. Previous diffraction studies by Goodenough *et al.* suggest that a 3:1 ratio of 96h/24d population is the optimum for high ionic conductivity, however the Al^{3+} ions present in their sample was not accounted for in the structural model [101]. Still, it is likely that high population of the 96h site is of importance for high ionic conductivity. How the site occupancy is correlated to the bulk conductivity is discussed next.

5.2.3 Discussion

In general, the ionic conductivity should follow the relationship: $\sigma = \mu q \eta$ where μ is the carrier mobility, q is the valence number, and η is the carrier concentration. Based on this equation, the conductivity is governed by the carrier concentration and/or the mobility, since the charge is fixed at 1 for Li-ion conductors. Thus, in order to understand the conductivity behavior, the carrier mobility and concentration must be well defined and the variables that affect these parameters must be understood. One such variable that has not been fully explored is the Li concentration on each of the two Li sites in the garnet crystal structure. It is asserted that the occupancy of the two Li sites plays a crucial role in how the carrier concentration is defined.

Models have been developed for single site conductors at the dilute limit to mathematically explain the charge transport ([111], Nernst-Einstein relations). Based on these theoretical models,

the carrier concentration is defined as all the Li ions in the system and is therefore equivalent with the Li stoichiometry, i.e. all the ions participate in conduction. However, this assertion was contested by investigation of the family of AgI materials, the archetypal single-site superionic conductor, nearly 50 years ago [119]. Originally, it was claimed that only a small fraction of the available Ag^{+} ions participate in conduction. However, after decades of disagreement, ionic Hall Effect measurements were performed and it was found that the Hall Mobility only agreed with the drift mobility if all the ions were participating in conduction [119, 120]. This definition of the carrier concentration, namely, that all the ions participate in conduction, has been applied to the garnet materials system even though garnet is fundamentally different from systems like AgI, where the theory was developed. For example, in the garnet system, two conduction sites are present. Nevertheless, this definition of the carrier concentration was assumed. Since the definition of the carrier concentration was not well defined even in the most studied family of ionic conductors, AgI, it is rational to have a similar conversation regarding how the carrier concentration is defined for the garnet family of ionic conductors.

For the garnet system, where the Li content is changed by the introduction of a dopant, it has been empirically observed in the literature that the ionic conductivity at room temperature passes through a maximum near a nominal Li content of 6.5 mols (Figure 5.25. The prevailing assumption has been that the conductivity increases as the Li content is increased primarily because the Li content (i.e. carrier concentration) is increasing. However, when the carrier concentration is calculated based on this assumption, it can be found that the conductivity is not increasing linearly with the

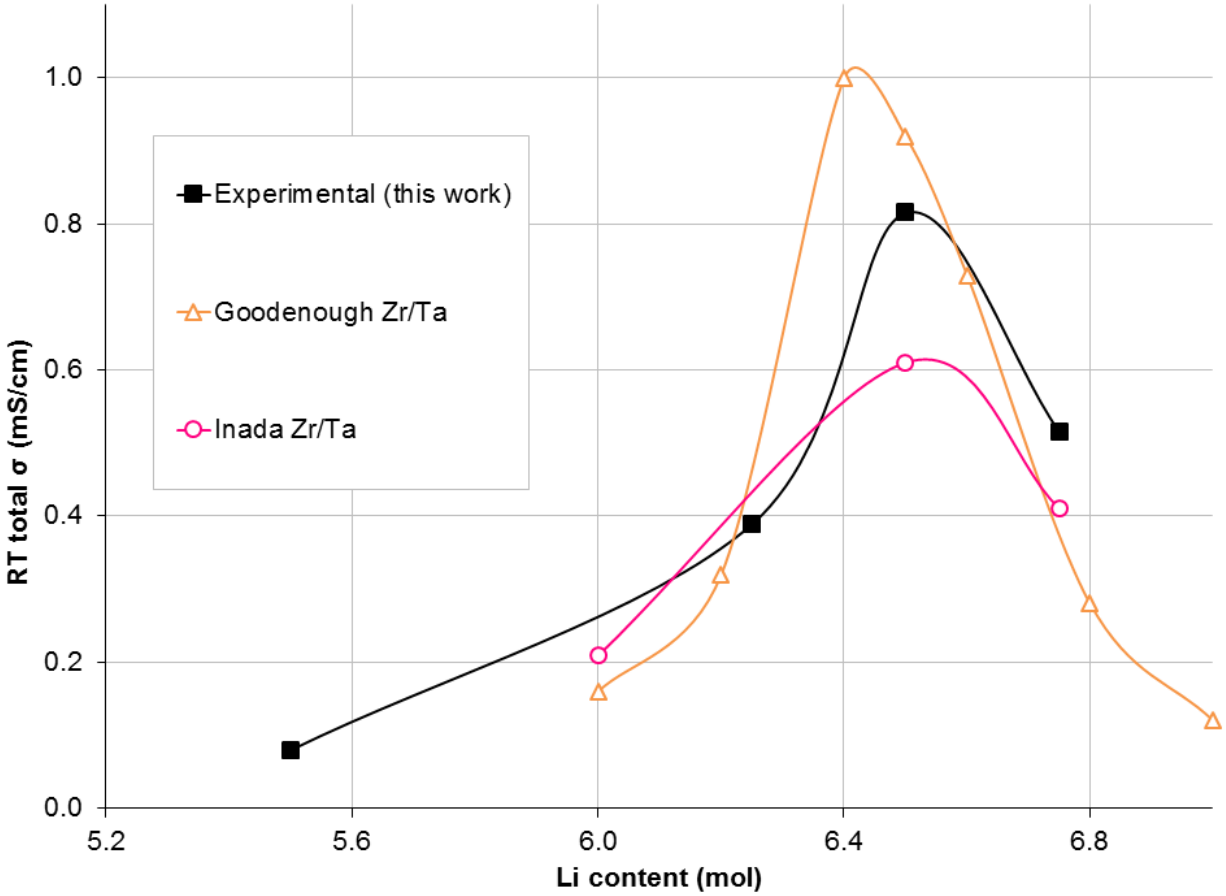

Figure 5.25: Plot of the room temperature total conductivity as a function of Li content from this work compared to literature references [101, 112].

carrier concentration. For example in this work, the conductivity of $Li_{6.5}La_3Zr_{1.5}Ta_{0.5}O_{12}$ is 120 percent higher than $Li_{6.25}La_3Zr_{1.25}Ta_{0.75}O_{12}$ even though the carrier concentration (assuming all the ions participate in conduction) only increases by 4 percent. Similar observations were made in the work of Ohta *et al.* on a related system with Nb doping on the Zr site. Since the carrier concentration (assuming all the ions participate in conduction) does not change enough to explain the increase in conductivity, it was thought that the mobility must, therefore, be responsible for the increase in the conductivity [81]. However, subsequent work by Ohta *et al. via* quasi-elastic neutron

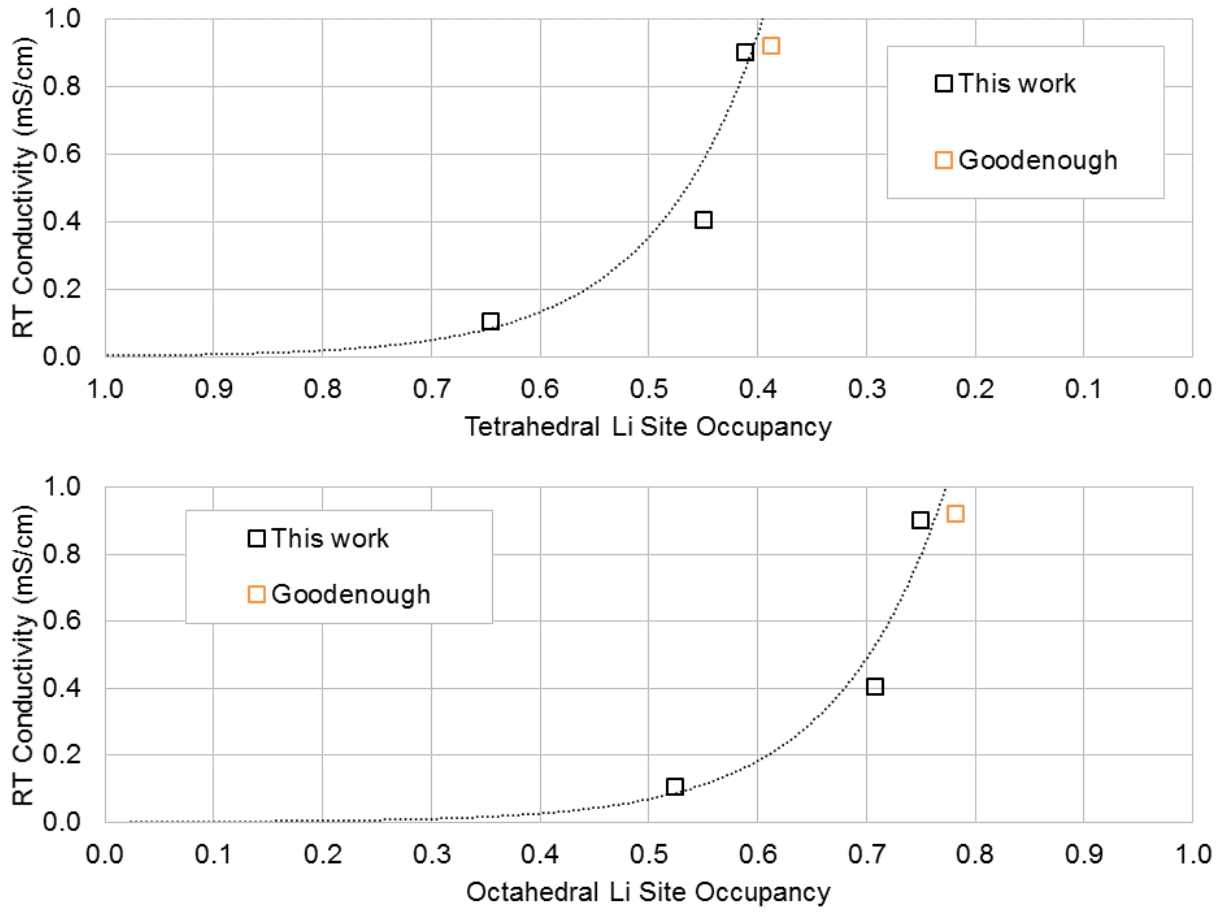

Figure 5.26: Plot of the room temperature ionic conductivity vs. the site occupancy for both the tetrahedrally coordinated 24d site and the octahedrally coordinated 96h site. Since equivalent circuit modeling was performed, the data of this work is the bulk conductivity while that of the literature reference is of the total conductivity [101]. The dotted line is included to help guide the eye.

scattering (QENS) and positive muon spin relaxation $(+\mu SR)$ found that the diffusivity (mobility) does not change with the dopant, and therefore Li, concentration and that only a small fraction (10 – 15 percent) of the ions were acting as carriers [121]. The finding that only a small fraction of the ions may be participating in the conduction is reminiscent of the discussion surrounding the AgI family of ionic conductors.

Even though there is not yet enough data available in the literature to draw a full definition, this

work proposes that the Li site occupancy is an important factor for defining the effective carrier concentration. Figure 5.26 plots the Li site occupancies determined from the results of the structural refinements vs. the room temperature bulk conductivity and is compared to values available in the literature. It should be noted that the literature reference in Figure 5.26 corresponds to the total conductivity. This work utilized 1) a hotpressing technique to minimize grain boundary contributions, 2) Ta^{5+} doping on the primary lattice to avoid affects of dopants on the Li sublattice and 3) equivalent circuit modeling of the impedance data so that direct comparison between the conductivity for the bulk and the Li site occupancy could be made. It can be seen that the conductivity increases non-linearly with population of the 96h site and depopulation of the 24d site.

To begin the discussion of how the carrier concentration should be defined, *this work proposes that the increase in conductivity, with increasing Li content, is caused by an increase in the effective carrier concentration.* It is asserted that the effective carrier concentration does not change proportionally with the Li stoichiometry. This type of behavior has been observed previously in the literature for $AgPO_3 - AgI$ glasses [122,123]. It is proposed that the highly *non-linear increase in conductivity* as the Li content is increased (Figure 5.26) is due to a synergistic *affect of the Li site distribution on the effective carrier concentration caused by carrier-carrier interactions.*

It has been shown from computational reports that there is significant carrier-carrier interactions in the stuffed garnets such that conduction pathway changes as the Li content is increased [117] and conduction occurs *via* cooperative ion movement cubic Li = 7 compositions [124, 125]. Interestingly, previous work comparing the conductivity behavior of AgBr, which exhibits high ionic mo-

bility but low conductivity, to AgI, a superionic conductor, suggest that highly interacting charge carriers may be a hallmark and even a necessary condition for superionic behavior [120]. It should be noted that the computations performed on the Li = 7 garnet compositions [124, 125] were artificially cubic. As discussed previously in this chapter and in the literature [42, 45, 99], as the Li content is increased past 6.5 moles, the system undergoes a reduction of symmetry from the cubic to the tetragonal phase, in order to relieve coulombic repulsion in the Li sublattice [99]. Perhaps the non-linear increase in the effective carrier concentration, and thus conductivity, could increase as the 96h site is further populated at the expense of the 24d site, however, the discussion held previously in the chapter has shown that phase segregation occurs and the conductivity decreases. Since it is thought that the 96h site occupancy is of importance for defining the effective carrier concentration in garnet, the carrier concentration has been calculated for each composition from the data presented in this work assuming all the ions participating and also assuming that only the ions occupying the 96h site are considered the carriers (Figure 5.27). However, neither of these definitions for the carrier concentration result in a linear increase in the conductivity when plotted vs the carrier concentration. This means that the definition of the carrier concentration is not all the Li ions, nor all the ions occupying the 96h site, but is further restricted. It is thought that the restriction to the definition of the carrier concentration arises from the fact that several variables, besides the Li site occupancy, are changed simultaneously by the introduction of a dopant.

Therefore, since the only known approach to change the Li site occupancy is by changing the total Li content *via* a dopant, compositions near Li = 6.5 with just enough Li vacancies to stabilize

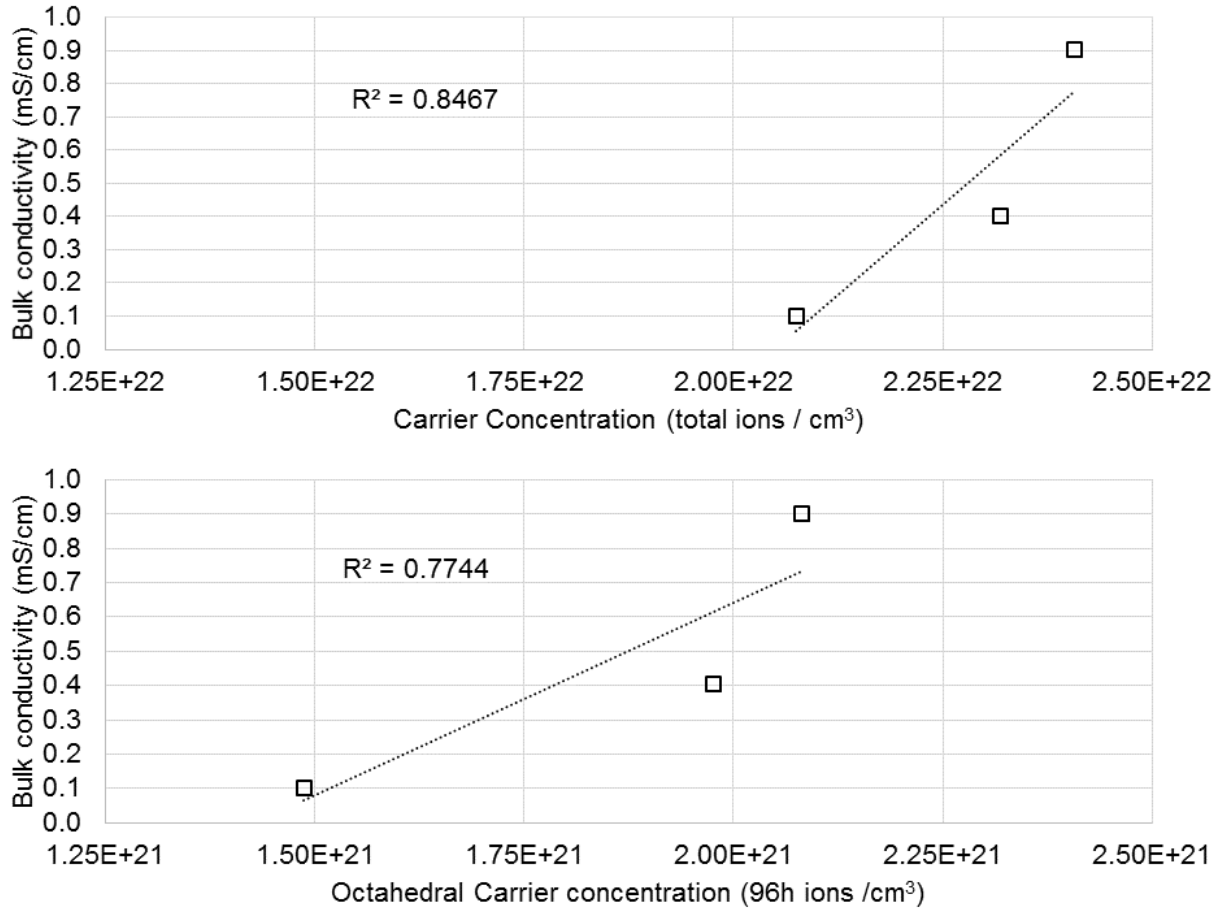

Figure 5.27: Plot of the room temperature ionic conductivity vs. the carrier concentration assuming all the Li ions participate in conduction (top) and assuming only the 96h Li ions participate in conduction (bottom). The dotted line is a linear fit and the R^2 value is included as a measure of linearity.

the cubic phase also represent the compositions the highest occupancy of the 96h site and lowest occupancy of the 24d site and therefore exhibit the highest possible bulk conductivity in LLZO. Even though the carrier concentration is not yet defined, the results suggest that compositions at the critical Li vacancies concentration to stabilize the cubic phase should be targeted for further studies. Certainly, other factors such as the lattice parameter also affect the conductivity, but before they can be investigated and conclusions drawn regarding them with any kind of certainty,

the carrier concentration must first be defined.

To summarize, LLZO based garnet materials seem to simultaneously meet the preliminary requirements needed in a solid electrolyte for thermogalvanic devices. Namely, 1) is a solid 2) sufficiently high total ionic conductivity, 3) negligible electronic conductivity, and 4) electrochemical stability with Li metal. More than that, though, the garnet materials system could be a new platform for fundamental scientific investigations into the nature of ionic transport in systems with more than one conduction site and significant carrier-carrier interactions. This system could help shed light on questions such as:

- Is cooperative ion movement a necessity for superionic conduction or is this requirement only an artifact of single site systems?
- How is the carrier concentration defined for ionic conductors with significant carrier-carrier interaction that conduct *via* cooperative ion movement?
- Is the apparently reduced effective carrier concentration a consequence of the carrier-carrier interaction or of the fact that two sites for conduction are present in the garnet system?

Answering these questions will lead to a better understanding of the variables which control the carrier mobility and concentration in the relationship $\sigma = \mu q \eta$ where μ and can lead to strategies to further increase the conductivity. This work also explains why compositions with just enough Li vacancies to stabilize the cubic phase exhibit the maximum in ionic conductivity. While these types of fundamental questions are being investigated, compositions near Li = 6.5 should be targeted for

the evaluation of the remaining thermogalvanic properties. As such, these compositions were selected for further thermogalvanic testing and are discussed next.

CHAPTER 6

THERMOGALVANIC OPERATION OF A SOLID-STATE CELL WITH A GARNET ELECTROLYTE

In Chapter 5, the zirconium based garnet system, with nominal composition $Li_7La_3Zr_2O_{12}$ (LLZO), was identified as a promising material for the electrolyte in a solid-state thermogalvanic cell. Thermogalvanic cells based on LLZO are discussed next. One of the key findings in Chapter 5 was that garnet compositions at the critical Li vacancy concentration to stabilize the cubic polymorph of LLZO exhibit the highest ionic conductivity and that these compositions should be the focus of further thermogalvanic evaluation. The investigation performed in Chapter 5 was done with supervalent doping Ta^{5+} on the Zr^{4+} site. However, it is not clear if the Ta^{5+} dopant will be electrochemical stable against metallic Li (the electrode of choice for the investigation of the remaining thermogalvanic properties) since there are lower oxidation states for the Ta atom besides +5. As such, supervalent doing of Al^{3+} on the Li^{+} site was selected. Even though the conductivity of compositions with Al as the dopant is lower then when Ta is used as the dopant for the same Li vacancy concentration, the Al atom only has one oxidation state (besides metallic) and is expected to be more electrochemically stable compared to Ta. A single composition was investigated, namely $Li_{6.1}Al_{0.3}La_3Zr_2O_{12}$, and the purpose of this work was to present proof of concept for the use of LLZO based electrolytes in thermogalvanic cells.

In order to investigate the thermogalvanic properties and determine a thermogalvanic zT for

LLZO, thermal conductivity, Soret coefficient and ionic conductivity were measured over a broad range of temperatures. The best practices for these measurements established by the thermoelectric community were attempted, however, it became evident during the investigation that thermogalvanic measurements have challenges not common to thermoelectric measurements. For example, in thermoelectric materials measurements, where the charge carrier are electrons/holes, the transfer of the carrier into the metallic contact is achieved through relatively simple ohmic contacts. However, in thermogalvanic systems the charge carriers, which are ions, may or may not be soluble in the electrodes which make contact with the material during the measurements. The electrode is known as a blocking electrode when the carrier ion is insoluble with the electrode material. Furthermore, the ionic conductivity is normally measured *via* AC impedance with blocking electrodes, as opposed to DC resistance in thermoelectric materials. This makes it is difficult to simultaneously perform all three measurements (thermopower, thermal conductivity, electrical conductivity) required to determine the zT in a single testing apparatus. As such, the data presented in this chapter was not simultaneously collected on a single sample but was assembled from several measurements and best estimates were made so that a thermogalvanic zT for LLZO could be determined for the first time.

6.1 Demonstration of LLZO-enabled thermogalvanic cell

Figure 6.1 is plot of the total ionic conductivity of LLZO. The 0.3Al doped sample is the focus of this study but the sample doped with 0.5Ta is included for reference since it was the focus of Chap-

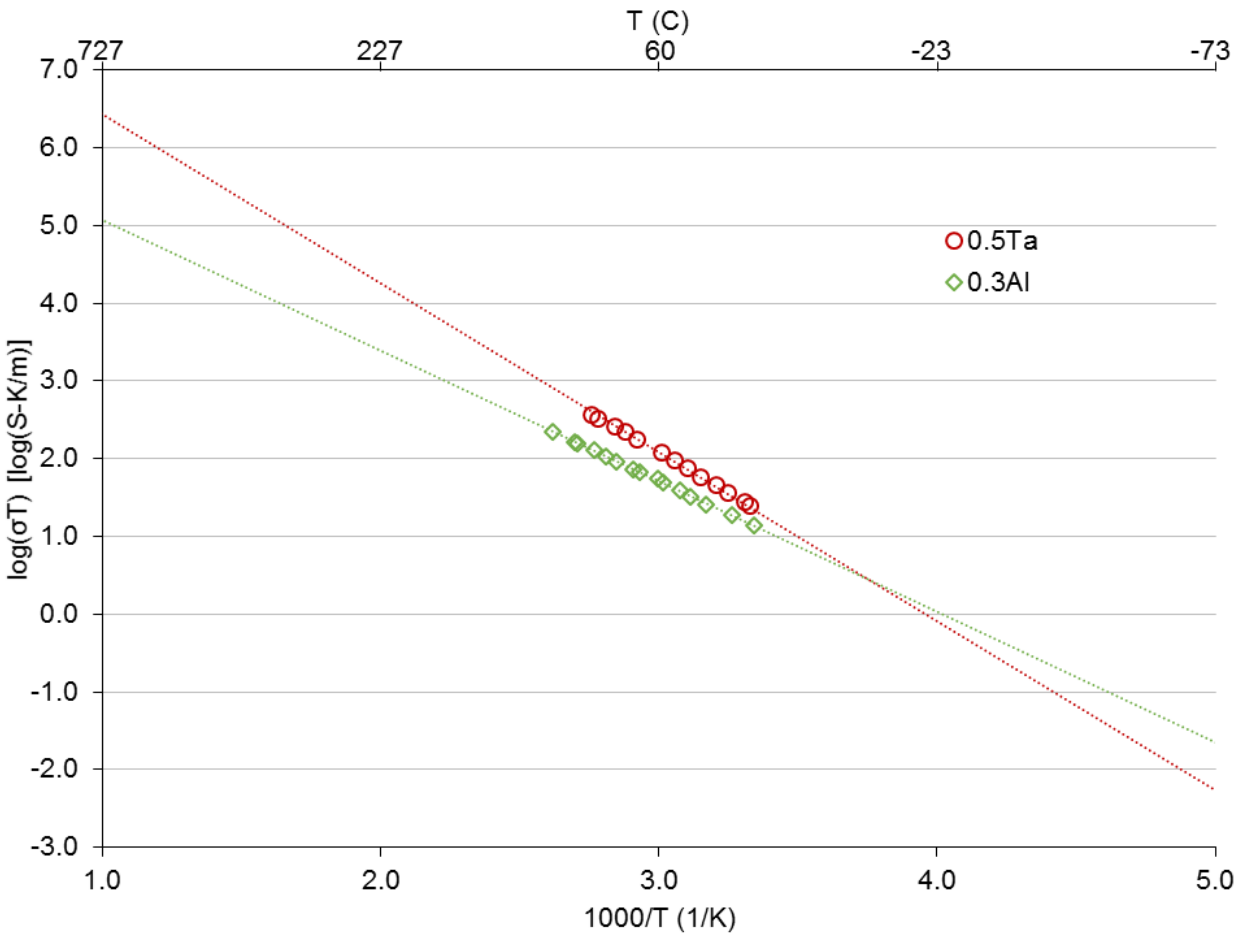

Figure 6.1: Arrhenius plot of the total conductivity for LLZO doped with Ta and Al with comparable Li vacancy concentrations near the critical concentration to stabilize the cubic phase. The dotted line is a linear fit to the data and is extrapolated to the entire temperature range that will be discussed in this chapter.

ter 5 and will be used in Chapter 7. It can be seen that the conductivity fits an Arrhenius description well. This allows for the extrapolation to temperatures outside the measurement window for combination with other materials properties to determine the thermogalvanic zT. When performing an extrapolation such as this, it is assumed that no phase transformations occur. A transformation of the tetragonal phase to the cubic is known at elevated temperature when no dopant is present. However, as discussed in Chapter 5, 0.3 mols of Al is enough to stabilize the cubic phase and

the assumption is seen as reasonable. Still, it is important to note that outside this (fairly narrow) temperature range, the conductivity is an estimate only. Later in this section when zT values are calculated, this data is reproduced but is not plotted in an Arrhenius fashion.

Figure 6.2 - Figure 6.6 are the thermogalvanic data collected for two different samples at low temperatures on the cryostat equipment with blocking electrodes. Figure 6.2 is a plot of the Soret coefficient for the first sample, referred to Cryo1 for the remainder of this work. It can be seen that the Soret coefficient is large and positive over most of the temperature. This trend is expected since the ions conducted are positively charged and previous work on solid ionic conductors also exhibited large values for the thermopower [20, 26]. It can be seen that near 250K, the value of the Soret coefficient quickly changes magnitude and sign. The reason for this is unclear, however, it may not be coincidental that this temperature is also near the melting temperature of water. Since it was unclear if this transition was intrinsic to the LLZO or an artifact of the measurement, a second sample was measured. Figure 6.3 is a plot of the Soret coefficient for the second sample, referred to Cryo2 for the remainder of this work.

It can be seen in the Figure 6.3 that the change in sign of the Soret coefficient observed in the Cryo1 sample is not present. However, the behavior of the Soret coefficient is considerably different. First, the majority of the data are negative in sign and highly erratic. It should be noted that the Ag paste did not wet either the Cryo1 or Cryo2 samples well during preparation for the measurement as evident by the poor adhesion of the Ag paste to the sample. It is possible that the erratic data observed is due to poor contact with the sample. Similar difficulties were

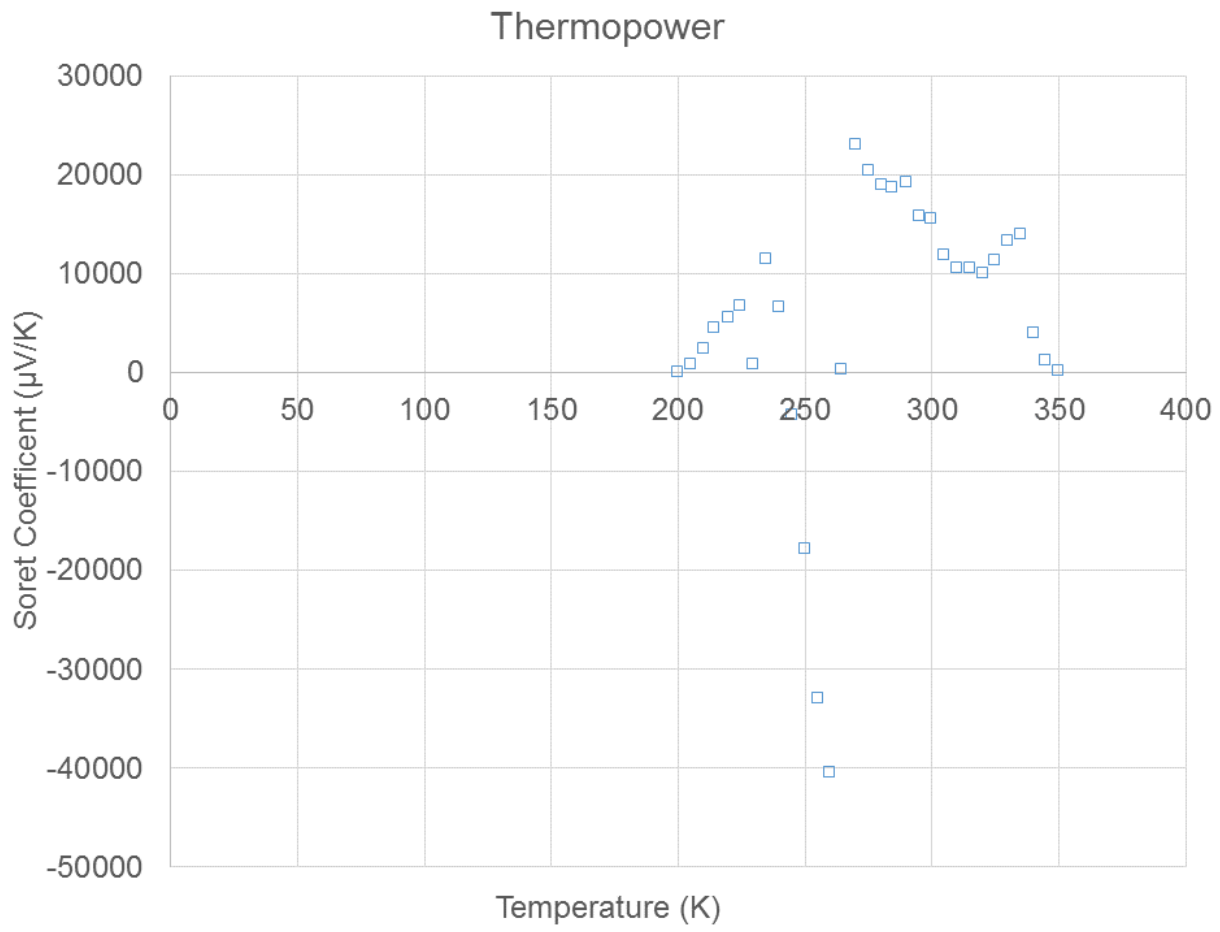

Figure 6.2: Soret coefficient for an Al doped LLZO sample measured at low temperatures on a cyostat (Cryo1).

experienced when thermoelectric measurements (presented in Chapter 4) were made on cobaltates using the same equipment and similar procedure. With the sodium cobalt oxide (NCO) and calcium cobalt oxide (CCO), it was hypothesized that an insulating surface layer, possibly a carbonate, was responsible for the poor contact with the samples. It is possible that a similar surface later is present with LLZO, preventing electrical contact with the sample.

Figure 6.4 is a reproduction of the total ionic conductivity shown in Figure 6.1. Figure 6.4 is plotted with linear axis so that direct comparison to the other thermogalvanic measurements can

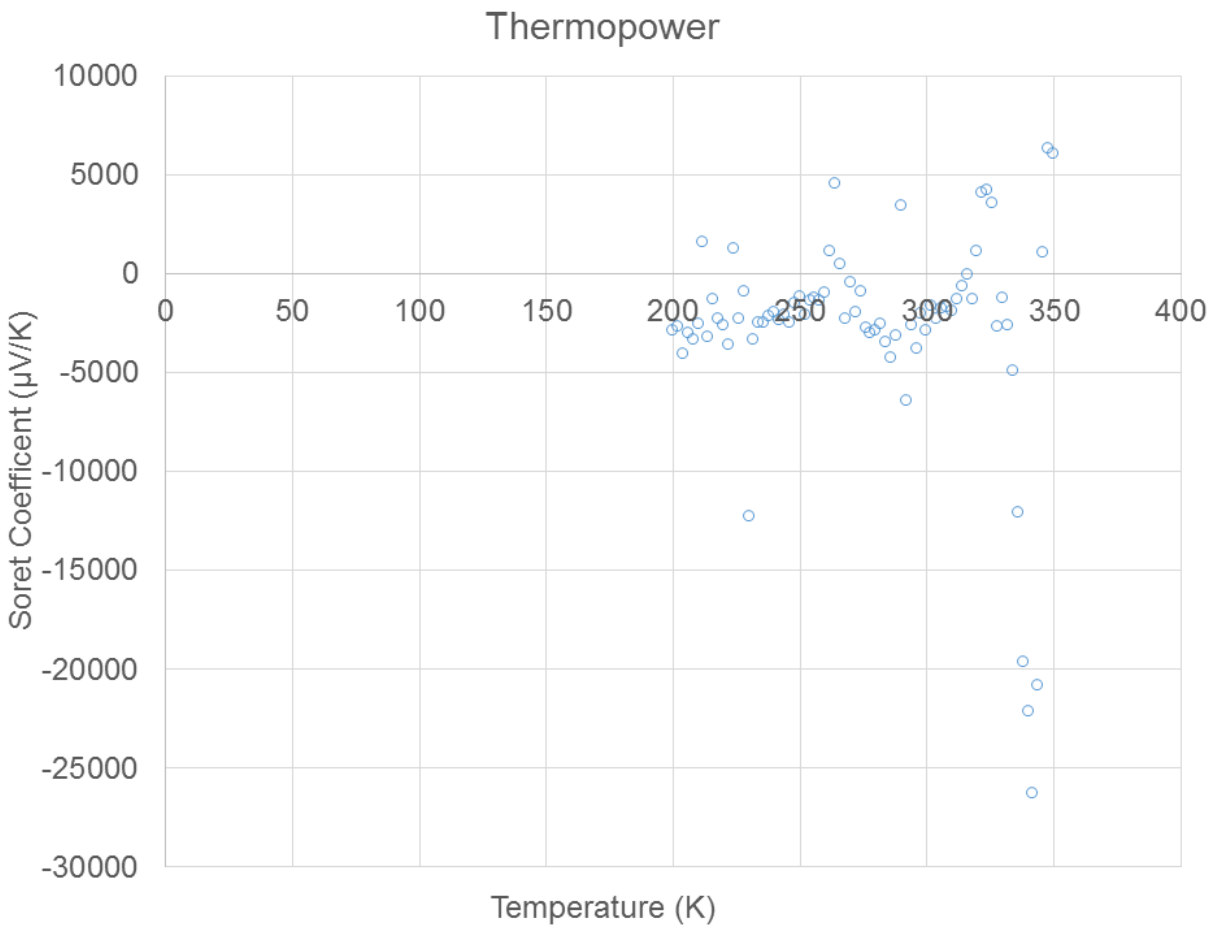

Figure 6.3: Soret coefficient for an Al doped LLZO sample measured at low temperatures on a cryostat (Cryo2).

be facilitated. Since this is an extrapolation of the Arrhenius data, unless otherwise noted, the remaining discussion regarding the conductivity for the remaining samples will refer back to this figure.

Figure 6.5 is a plot of the total thermal conductivity for both the Cryo1 and Cryo2 sample. Both samples exhibited similar trends for the thermal conductivity with values falling between 3 and 0.5 $\frac{W}{mK}$. Like the Soret coefficient data presented above, this data was collected with Ag paste electrodes and it was likely that poor contact was made. However, unlike the Soret measurements,

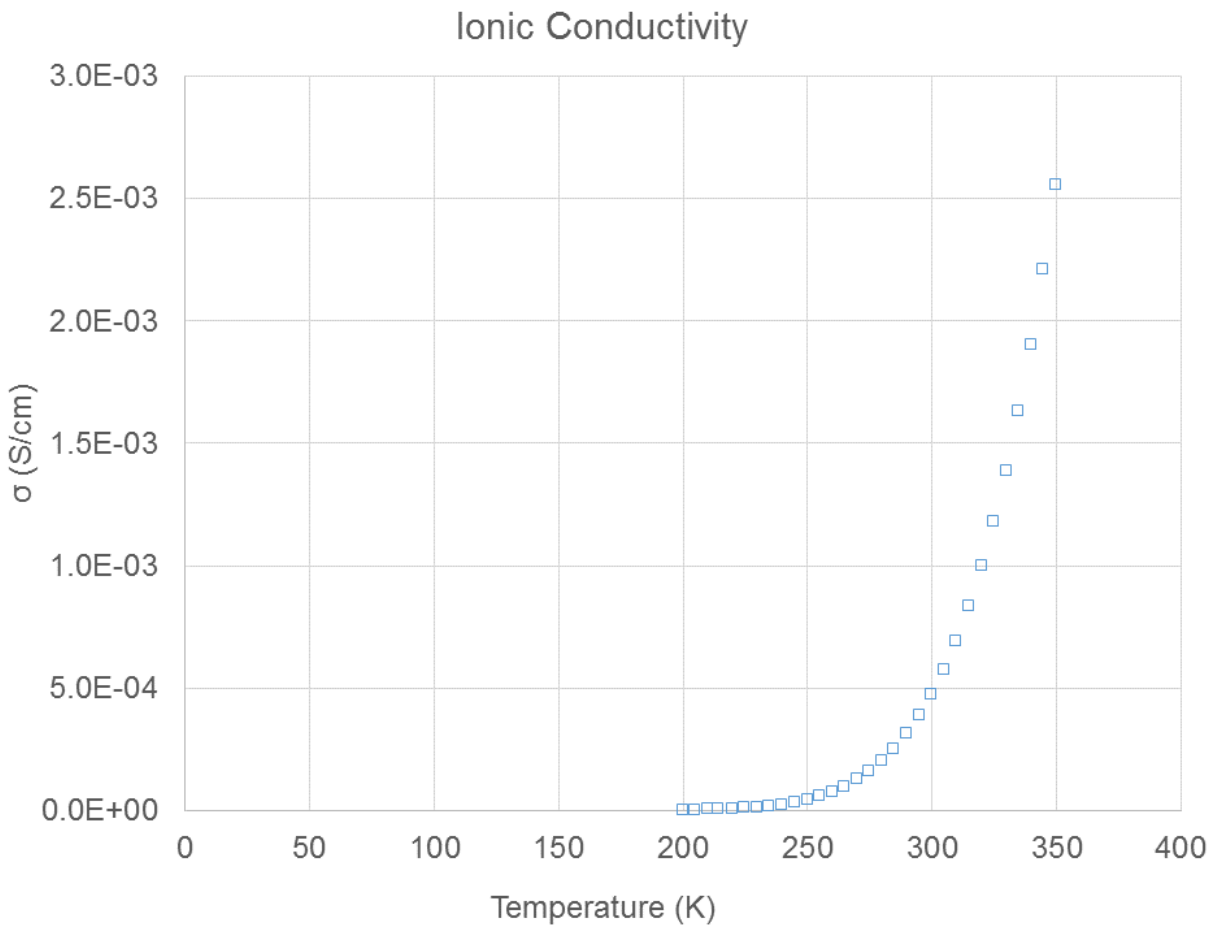

Figure 6.4: A reproduction of the total ionic conductivity shown in Figure 6.1. A linear axis so that direct comparison to the other thermogalvanic measurements can be facilitated.

it is probably that the surface layer has a comparable thermal conductivity to the sample and is not effecting the outcome of the measurements. Still, variation in the data is observed for both samples. A similar observation regarding the thermal contact and resulting measurements was made in the cobalt thermoelectric data presented in Chapter 4.

Figure 6.6 is a plot of the zT calculated from the Soret coefficient, ionic conductivity, and thermal conductivity presented above. The zT (y-axis) is plotted logarithmically since the values vary by several orders of magnitude as a function of temperature. This behavior is primarily a

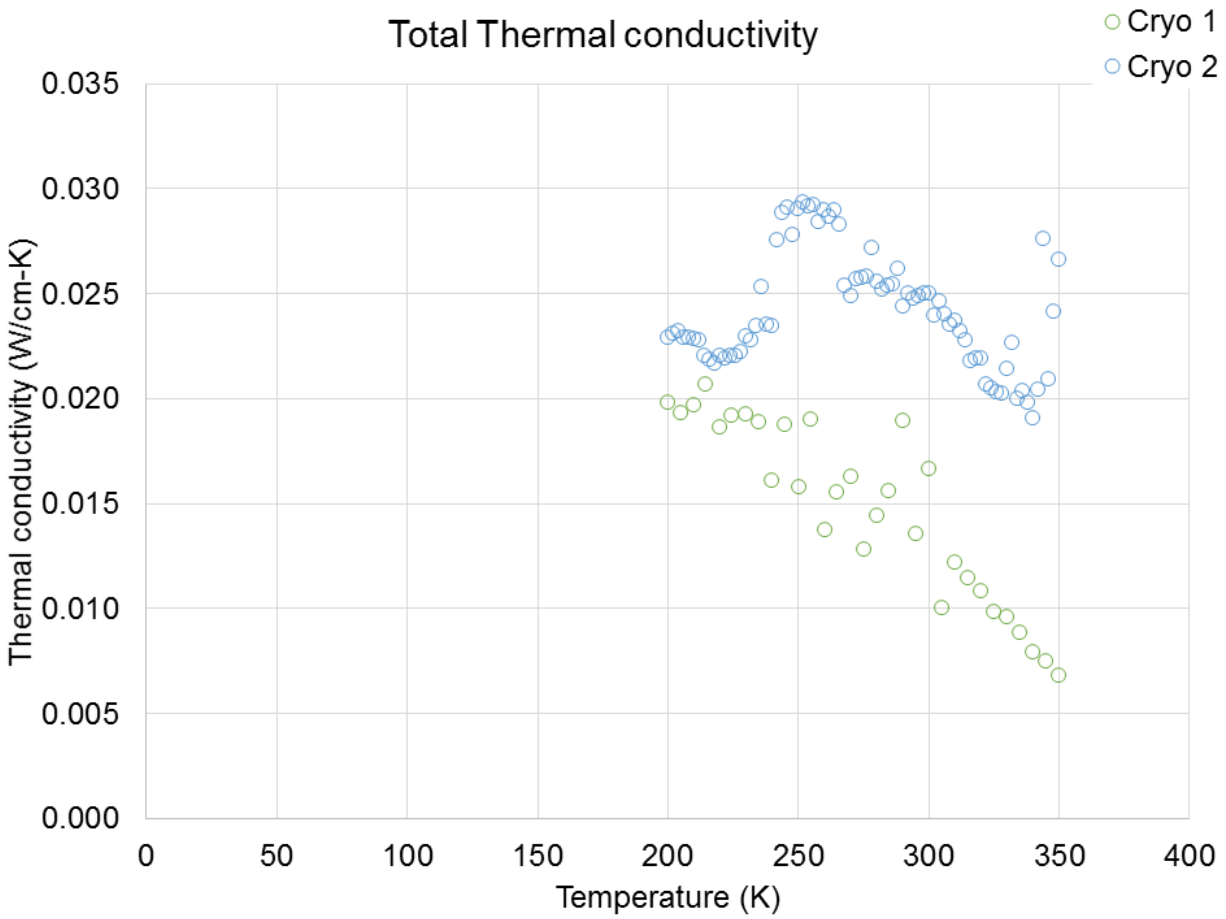

Figure 6.5: Plot of the total thermal conductivity for both of the Al doped samples measured at low temperatures (Cryo1 and Cryo2).

reflection of the ionic conductivity, which exponentially varies with temperature and likely governs the temperature dependent transport properties. A generally increasing trend with temperature is observed and the maximum zT for the Cryo1 and Cryo2 samples are 0.012 at 335K and 0.023 at 342K respectively. For the purpose of this work, the Soret coefficient in the calculation of the zT is taken without question and the change in sign observed as a function of temperature is simply ignored. Certainly, further work is required in understanding the Soret coefficient in these materials.

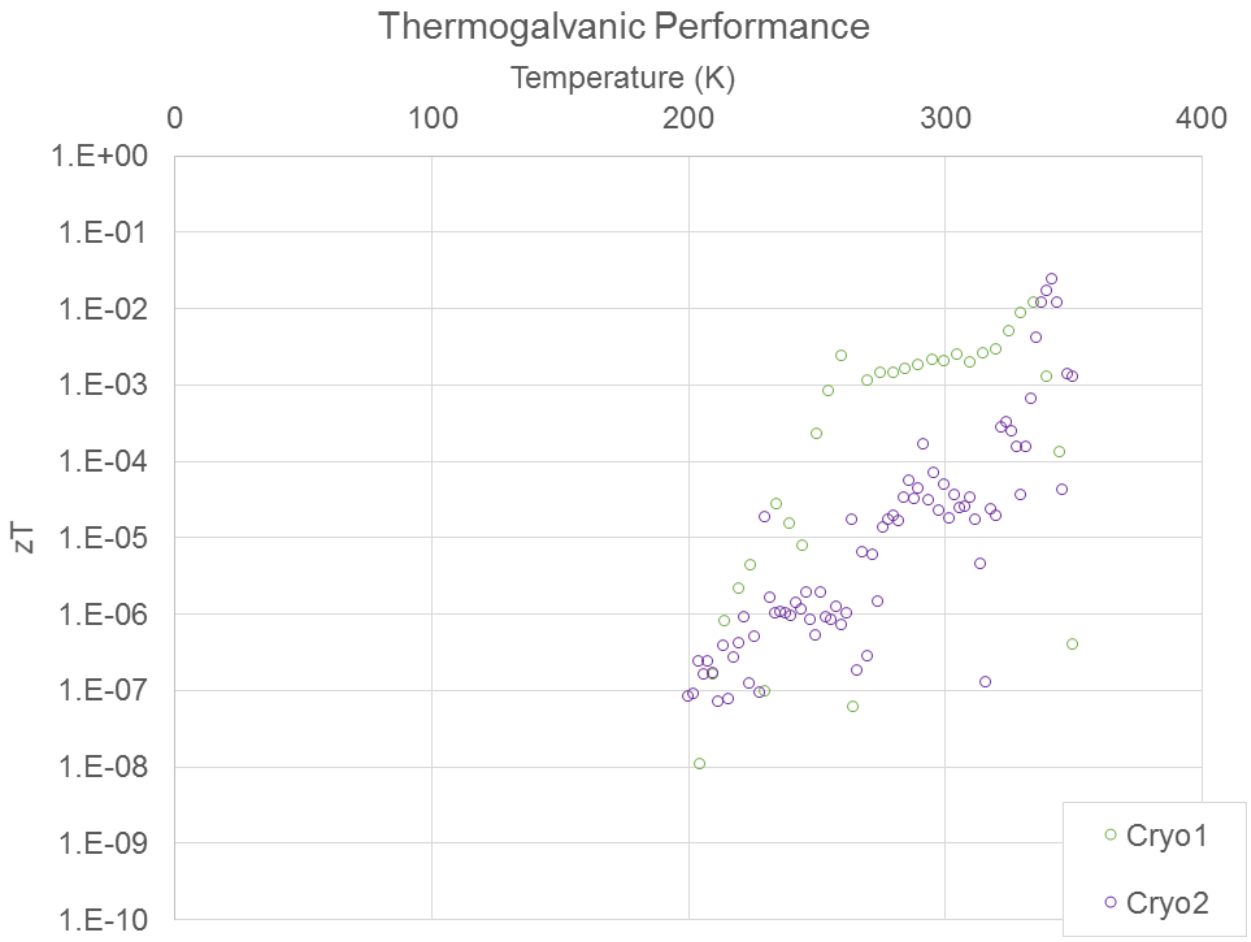

Figure 6.6: Plot of the thermogalvanic figure of merit, zT, for both of the Al doped samples measured at low temperatures (Cryo1 and Cryo2).

Since it was evident that the Ag paste electrodes did not form an acceptable contact with the material during testing and it is not clear whether the use of blocking electrodes is valid for the determination of the Soret coefficient, an attempt was made to rectify this. First, formation of a surface layer was minimized by limited exposure of the samples to ambient air. This was accomplished by assembling the cells and performing the measurements in a dry room (approximately 230K dew point). Second, Li metal foil ws used for both the hot and cold electrodes. It was thought that the ductility of the Li metal would be sufficient in forming a low contact resistance interface

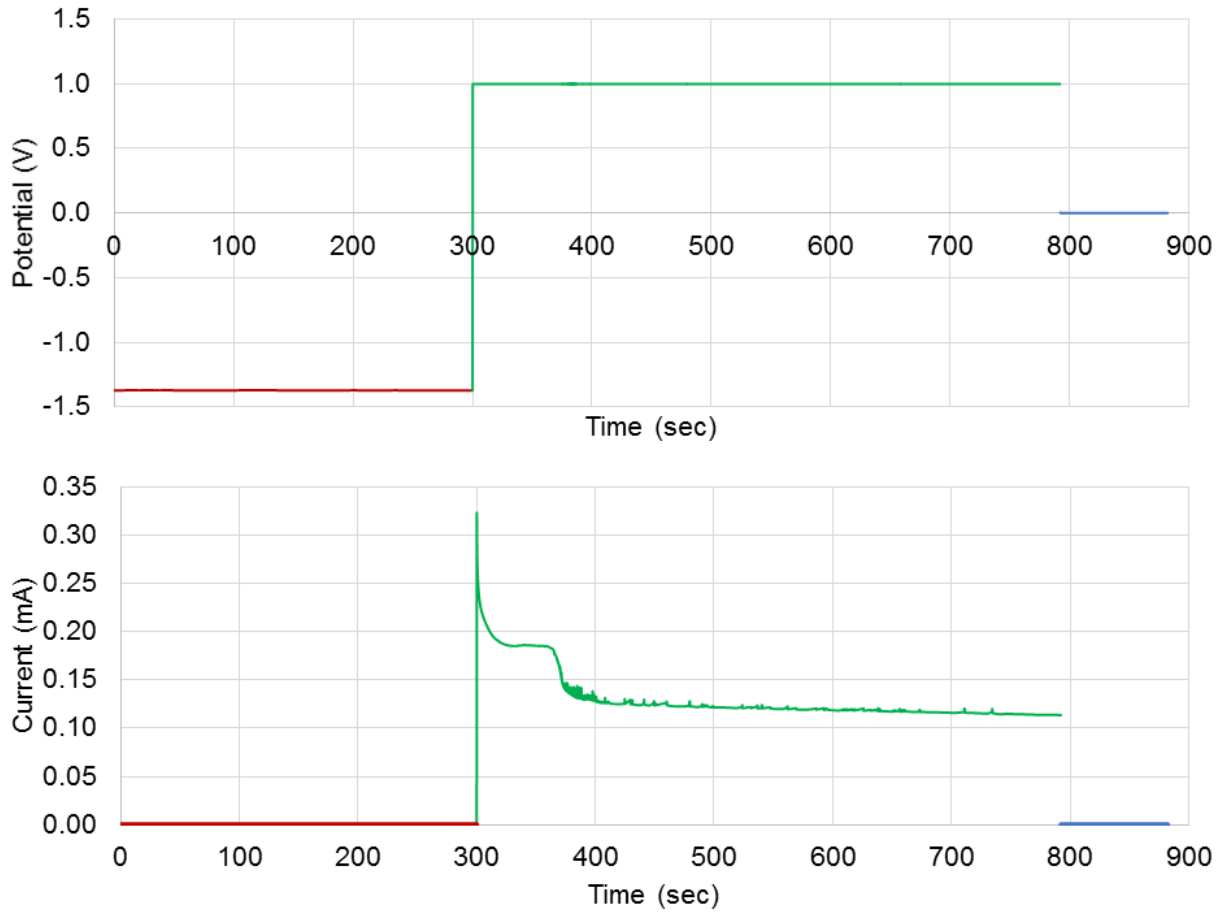

Figure 6.7: Plot of the potential and current of the Li/LLZO/Pt(Li) cell as a function of time during the Li plating experiment.

with the sample. Furthermore Li metal electrodes are not blocking with the LLZO electrolyte. The use of non-blocking electrodes is seen as more relevant for the characterization of thermogalvanic materials since these are the type of electrodes which will be used in a device. However, contact resistance was still found to be an issue. As such, a sputtered Pt film was formed on one of the surfaces and Li metal was electrochemically plated to from the interface of the cold electrode. Li metal foil was still used as the hot electrode. This mitigated most of the contact impedance problems and measurements were possible.

Figure 6.7 is a plot of the potential of and current through the Li/LLZO/Pt(Li) cell as a function of time and represents the Li plating experiment described above. The cell was isothermally heated to 70C, the working electrode was the Li foil and the counter electrode was the Pt film. From t = 0 - 300 seconds, the cell is in open circuit condition and the OCV is near -1.3V. At 300 seconds, the potential of the cell is stepped to 1V and held there for approximately 500 seconds. During the step, a chronoamperometric measurement was performed and the current through the cell was recorded. It can be seen that initially, the current response decays exponentially to a steady state value near 0.2 mA. This is consistent with a capacitive like response of the polarization of the cell. Next, at 350 seconds, the current again falls and approaches a new steady state value near 0.1 mA. It is believed that plating of metallic Li began at the second feature near 350 seconds. At 800 seconds, the cell was returned to open circuit conditions and it was observed that the OCV was near 0V. This was taken as evidence that metallic Li was plated on the sputtered Pt interface. In order to confirm the formation of a plated Li metal interface, EIS was performed before and after the Li plating experiment.

Figure 6.8 is a Nyquist plot of the complex impedance data for the Li/LLZO/Pt(Li) cell before and after the Li plating experiment. It can be seen in the figure that impedance response of the cell before Li plating exhibits a semi-circular feature at high frequencies, a flat almost linear region at mid frequencies, and a tail at low frequencies. From previous equivalent circuit modeling shown in Chapter 5, it is assumed that i) the high frequency feature corresponds to the ionic conduction through the LLZO electrolyte, ii) the mid frequency region corresponds to the charge transfer

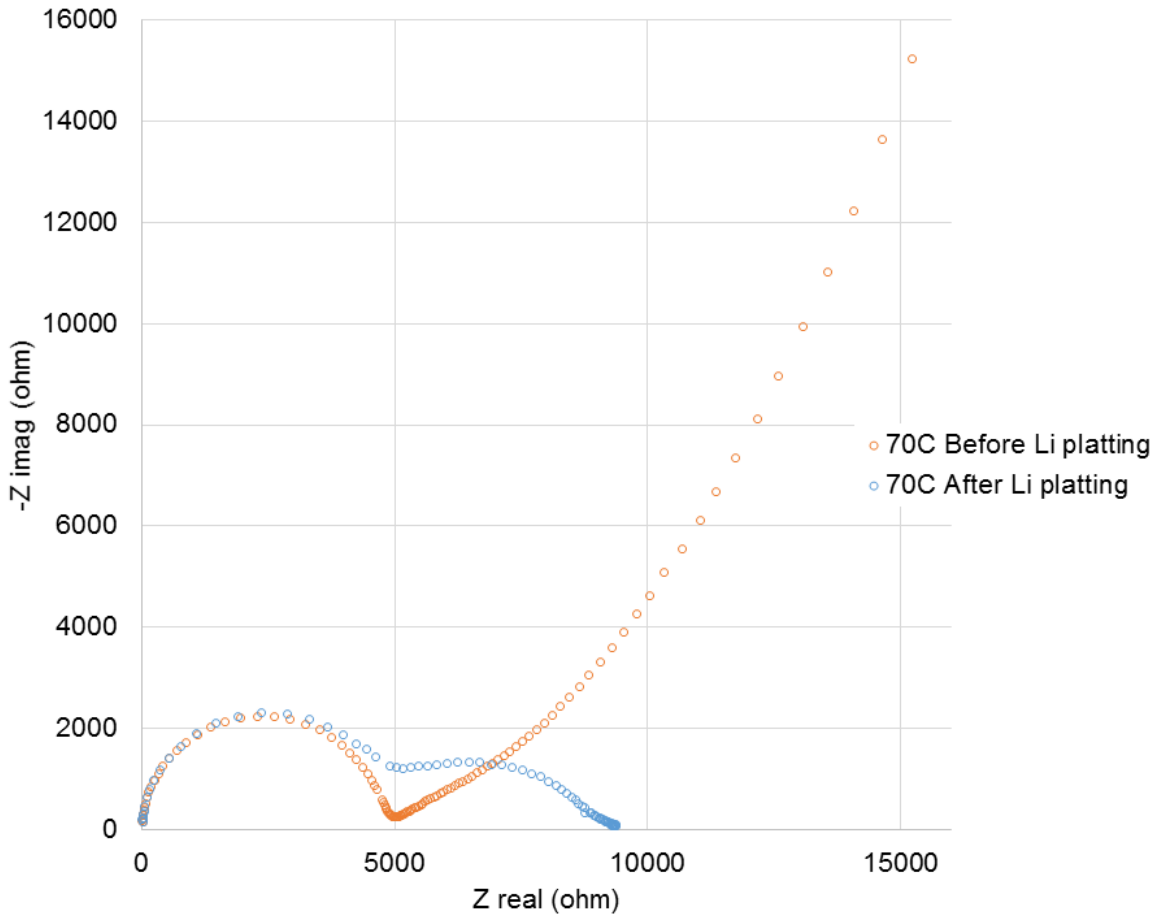

Figure 6.8: Nyquist plot of the complex impedance of the Li/LLZO/Pt(Li) cell before and after the Li plating experiment.

event at the Li/LLZO interface, and iii) the tail corresponds to the blocking behavior of the Pt film. After the Li plating experiment, it can be seen that the high frequency feature is unchanged, the low frequency tail is absent, and the mid frequency feature is now a clearly resolved semi-circle that is larger in diameter then before the experiment. The increase in the diameter of the mid frequency feature is consistent with the formation of a second Li/LLZO interface and two charge transfer phenomenon of equal magnitude occurring. The change in the impedance spectrum and the 0V OCV after the chronoamperometric experiment are consistent with the formation of a plated

metallic Li interface.

After deposition of the Li metal electrode on the Pt current collector, the cell was left undisturbed and cooled to room temperature so that the measurement of the Soret coefficient could be performed. Since these measurements were performed by hand, maintaining a low ΔT across the LLZO parallelepiped as the average temperature was increased (the conditions that the measurements on the cryostats were performed) was not possible. As such, a large ΔT was established so that the Soret coefficient at above ambient temperatures could be estimated. The OCV for the cell was measured as a function of time as the temperature gradient across the cell was established.

Figure 6.9 is a plot of the OCV as a function of time as the temperature gradient was established. The line is a floating average of the data and the data are the dark region behind the line. From 0 - 9,000 seconds, the cell is isothermal and the OCV is near 0V. At approximately 9,000 seconds the thermal gradient was applied. It can be seen that the cell voltage quickly increased and begins to stabilize near 22,000 seconds. It is unclear why the cell voltage dropped near 18,000 seconds. At 25,000 seconds the temperature of both electrodes and the voltage was recorded ($T_{hot} = 102.4C$, $T_{cold} = 47.6C$, and the OCV was approximately 12.8 mV). Both the temperature and the voltage were stable and the Soret coefficient was calculated to be 235 $\frac{\mu V}{K}$. As expected since the charge carriers are positive, the Soret coefficient was positive, however, the magnitude was smaller then expected. The Soret coefficient for the measurements with blocking electrodes was on the order of several $\frac{mV}{K}$ and other solid materials measured previously in the literature were on the order of 1 $\frac{mV}{K}$ [20, 26]. It is possible that contact impedance is still an issue with the hot

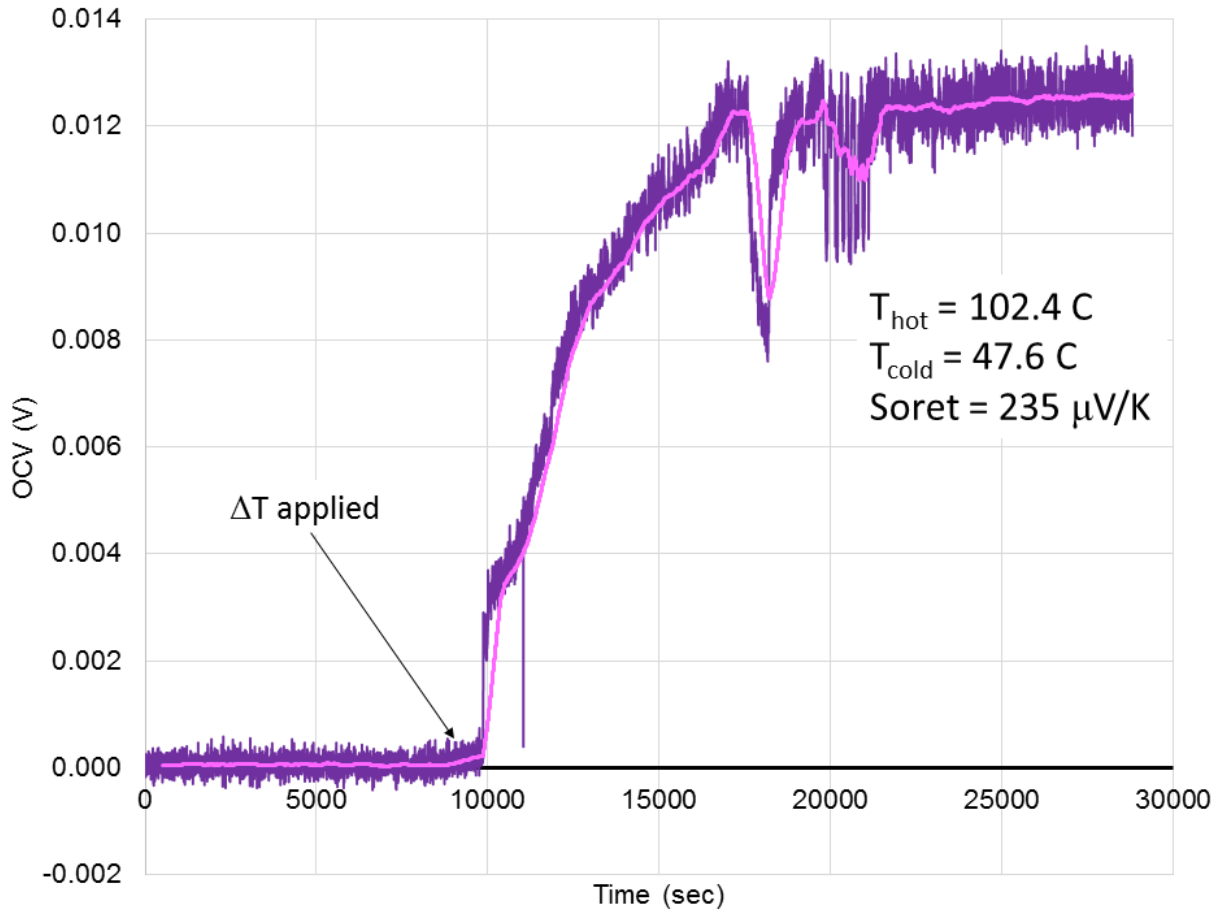

Figure 6.9: A plot of the OCV as a function of time as the temperature gradient was established across the Li/LLZO/Pt(Li) cell.

electrode and is responsible for the decrease in the Soret coefficient measured.

Before the cell was cooled to room temperature and disassembled, a counter current was incrementally applied and a chronopotentiometric measurement was performed. This data was used to construct the I-V and I-P curves shown in Figure 6.10. It can be seen that the Li/LLZO/Pt(Li) cell is behaving ohmicly with a linear change in the potential as a function of current. A linear best fit, the equation for the line, and an R^2 value are included as annotations in Figure 6.10. The slope of the linear line corresponds to the DC internal resistance of the cell. The value of approximately

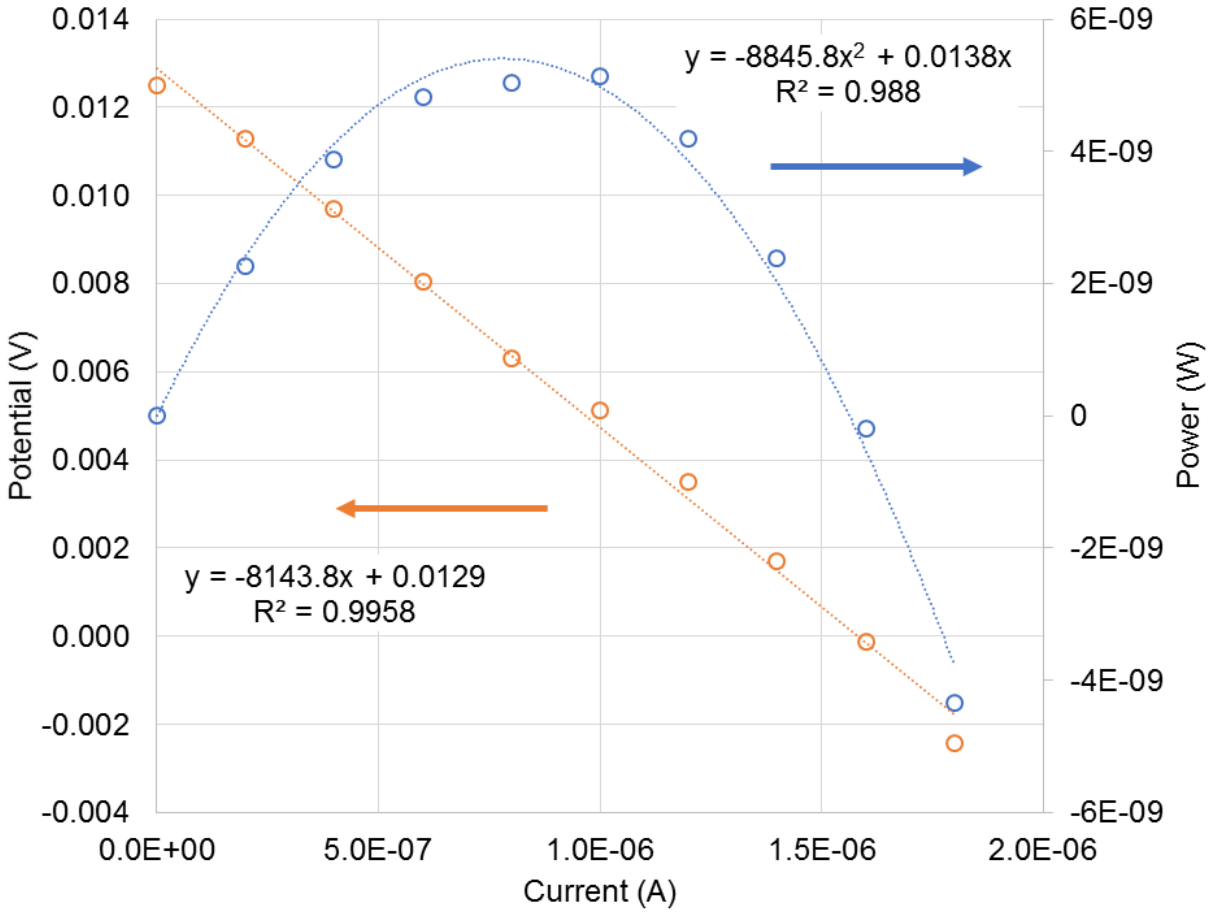

Figure 6.10: A plot of the voltage vs the current and power vs the current through the Li/LLZO/Pt(Li) cell.

8000 Ω agrees with the value of approximately 9000 Ω as measured by the AC technique (Figure 6.8). The power generated by the cell was calculated by: $P = IV$ and is also shown in Figure 6.10. The data was fitted with a parabolic function and it was found that the maximum power was 5.4 nW at 0.78 μA. In terms of current and power density, this corresponds to 8.6 $\frac{\mu A}{cm^2}$ and 60 $\frac{nW}{cm^2}$, respectively, for this sample.

Thermal diffusivity measurements were carried out on two samples using a laser flash technique so that a thermogalvanic zT could be estimated at elevated temperatures. The thermal dif-

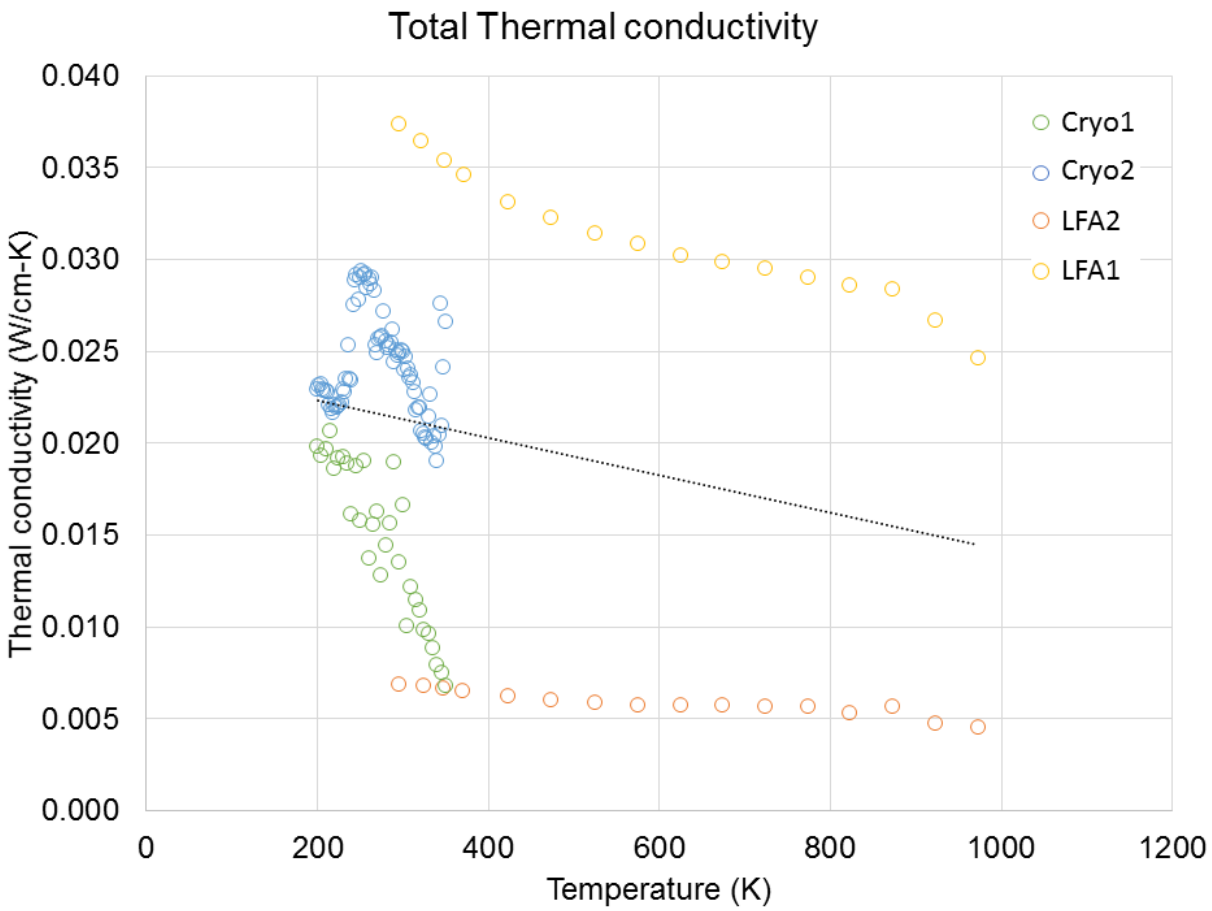

Figure 6.11: A plot of the total thermal conductivity, as estimated from laser flash thermal diffusivity measurements, of Al doped LLZO as a function of temperature. Since the temperature ranges overlap, the low temperature measurements made on the cryostat are included. The dotted linear line is a fit to all four data sets.

fusivity data was then used to calculate the thermal conductivity. Since the temperature ranges overlapped, Figure 6.11 shows the results of the thermal conductivity from the laser flash experiments along with low temperature data from the cryostats. It can be seen in the figure that the results of the four measurements, on four different samples, are within reasonable agreement. In order to estimate the zT over the whole temperature range, a linear fit to all four data sets (dotted line in Figure 6.11) was used.

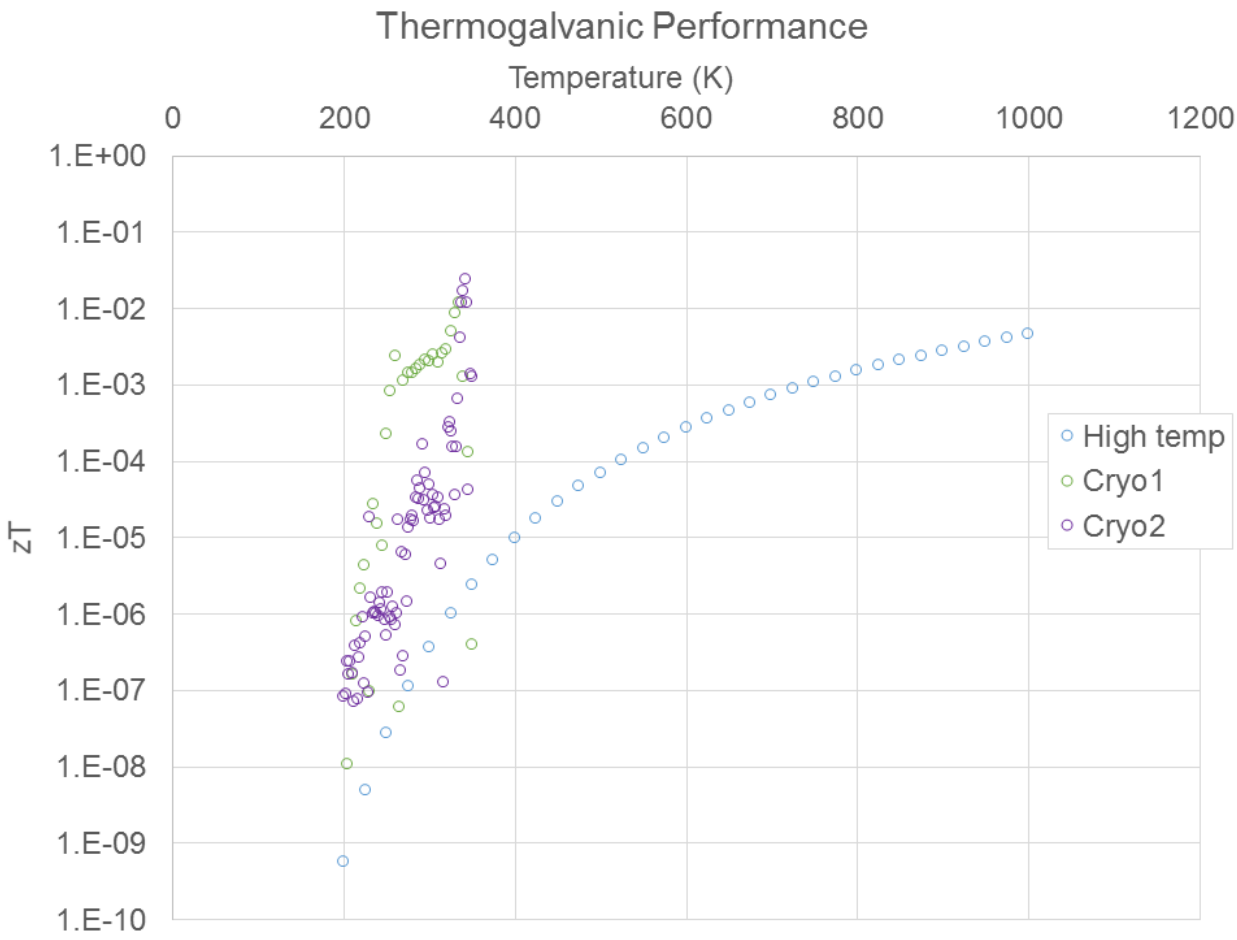

Figure 6.12: Plot of the thermogalvanic figure of merit, zT, for both of the Al doped samples measured at low temperatures (Cryo1 and Cryo2).

Using the linear fit to the thermal conductivity (Figure 6.11), the Arrhenius fit to the ionic conductivity (Figure 6.1) and a constant Soret coefficient of 235 $\frac{\mu V}{K}$ (Figure 6.9), the thermogalvanic figure of merit was estimated over the entire temperature range of 200 - 1000 K (Figure 6.12). The results of the low temperature cyrostat measurements are included for reference even though it is unclear if the use of blocking electrodes is valid. These three data sets are within reasonable agreement with each other and represent a first report of the estimation of thermogalvanic performance of LLZO. Clearly, a zT of 10^{-3} is too low for use in a real device. However, it should be noted

that these results are for a completely unoptimized system. The measurements presented in this chapter and the resulting thermogalvanic zT presented in Figure 6.12 are taken as proof of concept that thermogalvanic cells based on garnet type LLZO solid electrolytes are feasible. Approaches to further increase the zT are discussed in the next chapter.

CHAPTER 7

CONCLUSIONS AND FUTURE WORK

As stated in Chapter 1, the purpose of this work was to:

> use an interdisciplinary approach to marry together the electrochemistry of galvanic systems with the strategies used to better semiconductor based thermoelectric materials and ceramics processing techniques to fabricate these systems.

As discussed in Chapter 2, thermogalvanic systems are not a new concept, however, little work has been performed on solid-state dual purpose thermogalvanic systems from a power generation standpoint. The majority of the work on thermogalvanic systems for power generation has been performed on liquid electrolytes. However, this approach has several disadvantages and solid electrolytes for thermogalvanic power generation seem to address the shortcomings of liquid electrolytes. Solid thermogalvanic materials had been investigated previously by General Electric in the 1950's and 1960's. It was shown that solid state thermogalvanic cells could be operated based on the superionic conductor AgI. However, upon cycling, cell failure occurred *via* penetration of Ag dendrites through the solid AgI. Further exploration of solid-state thermogalvanic systems has been hindered by the lack of superionic conducting materials for the electrolyte which can also resist dendrite penetration. As discussed in Chapter 5, the discovery a new superionic conducting material LLZO, based on the garnet crystal structure, could meet the requirements of an electrolyte

for thermogalvnic devices. Mechanical properties measurements suggest that LLZO should have a sufficiently high shear modulus to resist Li dendrite penetration. This work has shown that LLZO exhibits superionic conductivity and has inspired new fundamental work regarding how the carrier concentration is defined for the system. Since LLZO simultaneously meets all the requirements of a thermogalvanic material, this work has endeavored to reintroduce the concept of a solid-state dual-purpose thermogalvanic device and evaluate the feasibility of using LLZO based garnet solid electrolytes in such a cell.

Advanced ceramic materials synthesis, powder processing, and materials characterization techniques were developed and utilized as a means to achieve this. This includes the invention of a new materials synthesis technique and the development of a novel hot-pressing technique. Several materials characterization techniques were used including: SEM analysis, Raman spectroscopy, powder x-ray diffraction, powder neutron diffraction, Rietveld structural refinement. Electrochemical techniques such as Electrochemical Impedance Spectroscopy with equivalent circuit modeling, chronoamperometric measurements and chronopentiometric measurements were used as well.

During the course of the investigations several observation were made. First, in Chapter 4, it was found that polycrystalline powder compacts of oxide thermoelectric materials based on layered cobaltate structures will most likely not match the performance of their single crystal counterparts even if significant texturing of the microstructure is achieved. Since the growth of single crystals is likely impractical in large quantities and of sufficient size, this, then, suggests that the cobaltate thermoelectric oxides investigated here may be platforms for scientific investigations but will have

many difficulties for commercialization of a device. Second, in Chapter 5, LLZO based on the garnet crystal structure was identified as a promising thermogalvanic material. A detailed investigation to understand the Li ion transport in these materials was performed and it was found that the carrier concentration for this system is not adequately defined to explain the conductivity behavior observed. Finally, in Chapter 6, it was shown that LLZO does exhibit thermogalvanic behavior and the proof of concept of a thermogalvanic cell based on LLZO was demonstrated.

7.1 Future Work

As presented in Chapter 6, the LLZO garnet based solid electrolyte can operate in a thermogalvanic cell. However, because the figure of merit (zT) is low, the overall conversion efficiency will be unacceptable in a real device. It is important to note that the thermogalvanic data are for an unoptimized system but clearly show that the concept is feasible. Therefore, future work should entail addressing the following question: How feasible is a zT >1, which would be comparable to state of the art thermoelectric materials? This section will outline some explanations for why the zT was lower then expected, experiments to validate the data, and finally will speculate on some possibilities if improvements to the properties that make up the zT can be made.

First, it became evident during this course of work that section of the electrodes and the interfacial properties between the thermogalvanic material of interest (LLZO in this case) and the electrodes is not trivial. Ag paste and Cu electrodes were originally selected for their ease of application and near zero Seebeck coefficient (since they are metals). It is unclear whether the use

of blocking electrodes is valid for the determination of the Soret coefficient since non-blocking electrodes will be used in a real device. As such, Li foil electrodes were used. It was believed that high ductility of the Li metal would facilitate contact with the LLZO. However, even with the application of heat and pressure, sufficient contact was not achieved. Only when the Li electrode was plated on an inert current collector was acceptable contact made. It is believed that interfacial impedance between the electrolyte and the electrodes is responsible for the lower then expected Soret coefficient. Evidence of this is found in Chapter 6, Figure 6.10. In the I-V plot, ohmic behavior was maintained well past the short circuit condition. In the Nyquist plot shown in Chapter 6, Figure 6.8, the interfacial impedance is almost half of the total cell impedance. Since the voltage measurement was made on the Li foil (or current collector), it is speculated that the interfacial impedance significantly reduced the overall cell potential. Soret coefficients for solid ionic conducting materials are on the order of 1 $\frac{mV}{K}$. An example of typical Soret coefficients was presented in Chapter 2, Figure 2.7. It is expected that the Soret coefficient of LLZO will be similar to what is measured for other solid electrolytes once the interfacial impedance is reduced and better contact is made.

Second, it became evident that no protocol is established in the characterization of thermogalvainc materials. In thermoelectric materials, it is widely accepted that all properties (thermal conductivity, electronic conductivity, and Seebeck coefficient) should be performed on the same sample at the same time. Furthermore, when measuring the Seebeck coefficient, care should be taken to measure the temperature and voltage at the hot and cold ends of the sample in the same

physical location and the temperature difference should be small (near 1K ΔT). These same best practices should be carried over to thermogalvanic materials characterization as well. However, because of the electrochemical nature of the device, realizing this is more difficult. For example, the stainless steel cladding used on thermocouples is not blocking with Li ions and an AC technique is needed to measure the ionic conductivity. Since high frequency perturbations are needed to perform the AC impedance measurements (>1 MHz), any AC interference from components in the measurement apparatus (such as heater pins) will be reflected in the measurement. Still, these are metrology details can solved and an experimental test bed will be developed. As experimental best practices are being developed, emphasis should be place on measuring the individual properties over extended temperature ranges so that less extrapolation is required.

Finally, improvements to each materials property which makes up the zT are clearly possible. First, if the interfacial impedance can be minimized, it is expected that higher Soret coefficients will be possible. Furthermore, it may be possible to tune the activation energy barrier, similarly to how band engineering is currently performed on thermoelectric materials [19], to further increase the Soret coefficient. Second, the thermal conductivity can be reduced. The crystal structure is complex for garnet materials so a low intrinsic thermal conductivity is expected. The same strategies to lower the thermal conductivity for thermoelectric materials (i.e. bulk nanostructuring, hierarchical ordered structures) [16, 18] should be possible. Third, the ionic conductivity can be increased. It has already been demonstrated in this work (Chapter 6, Figure 6.1) that doping with Ta instead of Al results in a nearly 2x higher conductivity near room temperature. As explained in

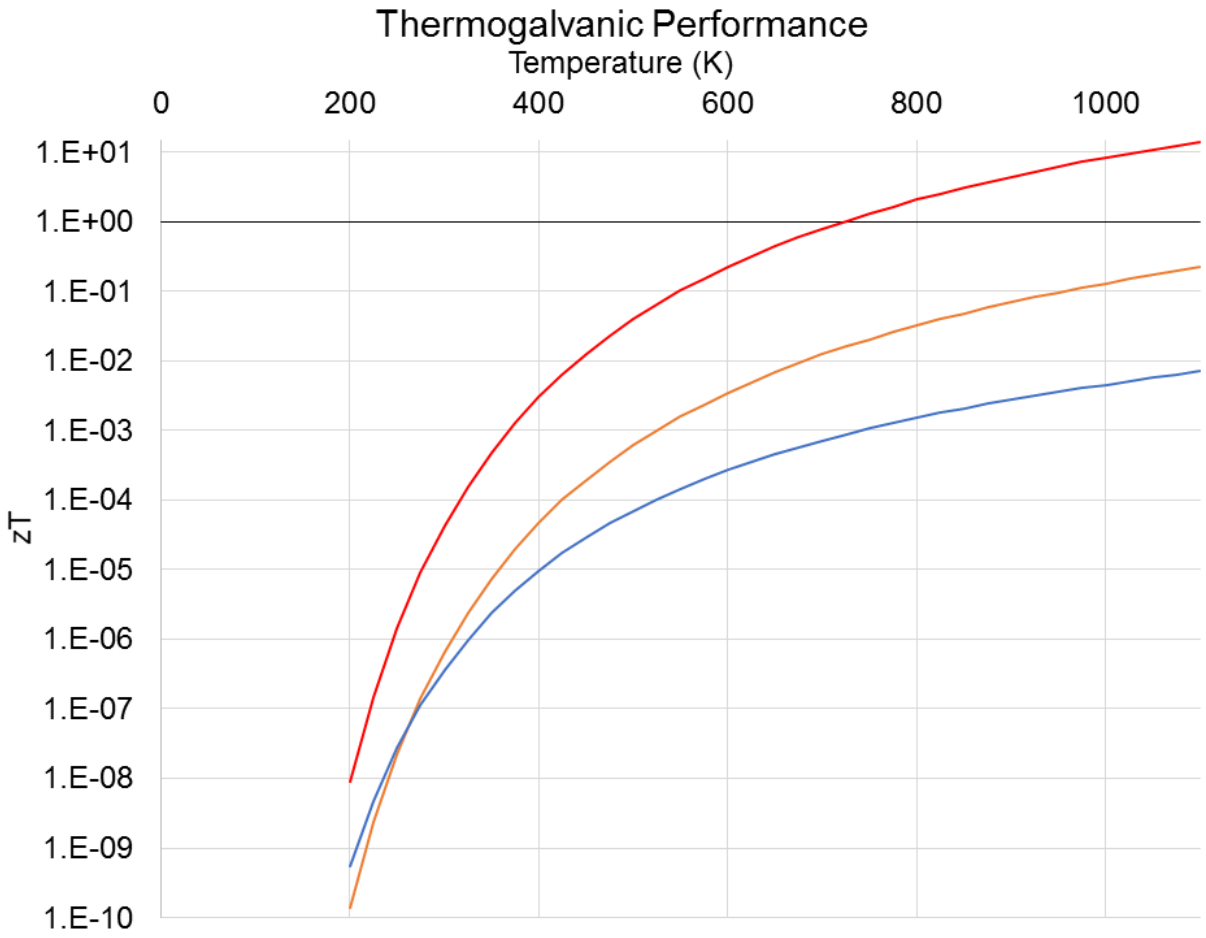

Figure 7.1: Plot of the thermogalvanic figure of merit, zT, estimated assuming various improvements to the physical properties of LLZO are possible.

Chapter 5, it is likely that the conductivity can be further increased though a better understanding of how the carrier concentration is defined.

Figure 7.1 is a plot of the zT estimated assuming some of the improvements to the materials properties mentioned above can be made. First, the blue line is the same estimate from Chapter 6, Figure 6.12 and is included as a baseline reference. The assumptions for this curve are i) constant Soret coefficient with increasing temperature with a value of 235 $\frac{\mu V}{K}$ (Chapter 6, Figure 6.9), ii) Arrhenius behavior of the ionic conductivity with temperature for Al doping (Figure 6.1), iii)

linearly decreasing thermal conductivity with increasing temperature ranging between 2.3 and 1.4 $\frac{W}{mK}$.

The orange line is an estimate assuming an improvement to the ionic conductivity can be made. Namely, the ionic conductivity used in the estimation of the blue line was with Al doping. This has been replaced with the conductivity that was measured for Ta doping. The remaining assumption have been left unchanged from the baseline. The Arrhenius behavior for Ta doping is included in Chapter 6, Figure 6.1 along with that for Al doping and it can be seen that Ta doping has a higher activation energy then Al doping. As such, at low temperatures, the zT would be expected to be lower for Ta doped LLZO but would cross over the baseline near room temperature and outperform the baseline by an order of magnitude near 1000K.

Finally, the red line represents an estimation of the zT assuming that improvements to the Soret coefficient and the thermal conductivity can be made in addition to the increase in the ionic conductivity due to the use of Ta as a dopant. Namely, it is assumed that a 4x increase in the Soret coefficient and a 4x decrease in the thermal conductivity can be achieved over the base line. Specifically, the assumptions are: i) constant Soret coefficient with increasing temperature with a value of 940 $\frac{\mu V}{K}$, ii) Arrhenius behavior of the ionic conductivity with temperature for Ta doping (Chapter 6, Figure 6.1), iii) linearly decreasing thermal conductivity with increasing temperature ranging between 0.58 and 0.35 $\frac{W}{mK}$. These assumptions are seen as reasonable since Soret coefficients near 1 $\frac{mV}{K}$ have been measured on other solid thermogalvanic materials [26] and similar reductions in thermal conductivity have been observed in optimized thermoelectric

systems [126]. It can be seen in Figure 7.1 that a zT of 1 would be expected near 700K under these assumptions. Since LLZO based garnets are oxide materials, they are stable in this temperature regime. As such, this is seen as reasonable operating temperature for a thermogalvanic device based on LLZO, assuming that the electrodes used in the cell are also stable in this temperature range.

In order to place the present thermogalvanic materials data presented here in context, Figure 7.2 plots the conversion efficiency determined form the projected thermogalvanic figures of merit estimates shown in Figure 7.1 and compares it to various power generation cycles [127]. Recall that the conversion efficiency for thermoelectric as well as thermogalvanic devices can be estimated from:

$$\eta = \eta_{Carnot} \frac{\sqrt{1+zT_{avg}} - 1}{\sqrt{1+zT_{avg}} + \frac{T_{cold}}{T_{hot}}} \tag{7.1}$$

Where η_{Carnot} is the Carnot efficiency, zT is the dimensionless figure of merit, T_{cold} is the cold side temperature, and T_{hot} is the hot side temperature.

The colored lines shown in Figure 7.2 correspond to the same conditions for those shown in Figure 7.1. As anticipated above, the conversion efficiency for the blue curve, which corresponds to a peak zT of approximately 10^{-3} is essentially zero for all temperatures. The conversion efficiency of the orange curve, which corresponds to a peak zT of approximately 10^{-1}, is still relatively low and with a value of a few percent above 1000K. However, the conversion efficiency of the red curve, which corresponds to a peak zT of approximately 10^{1}, is appreciable at elevated tempera-

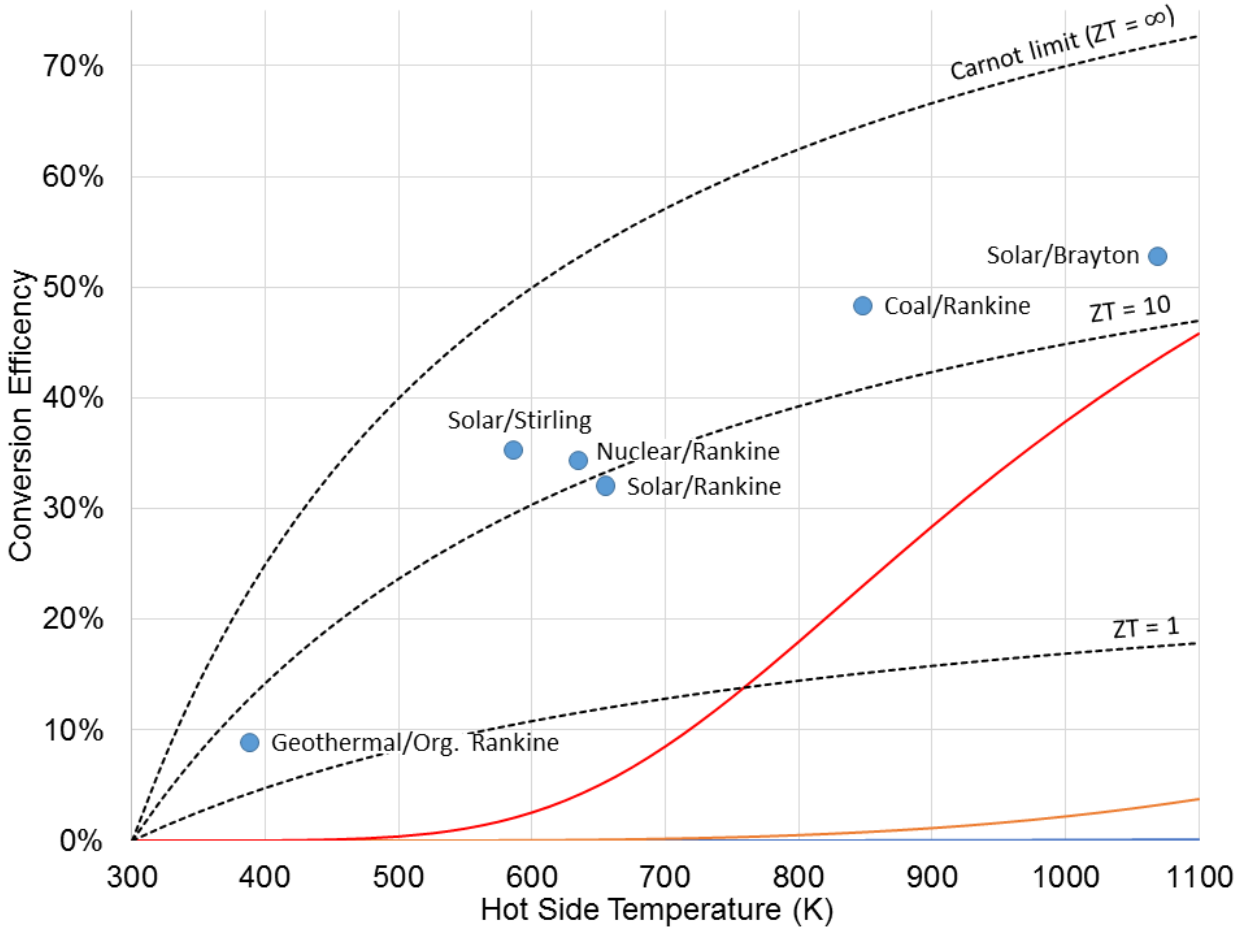

Figure 7.2: Plot of the conversion efficiency estimated from the projected improvements to the thermogalvanic figure of merit, zT, discussed in the chapter. These estimates are compared to currently utilized mechanical heat engines [127]. Constant lines of ZT are included for reference to thermoelectric devices.

tures. The improvement to the conversion efficiency is primarily a reflection of the improved zT due to the projected increase to the Soret coefficient with better contact of the electrolyte to the electrodes in the cell. Dashed lines corresponding to constant ZT of 1, 10 and infinite are included for reference to thermoelectric materials. An infinite ZT corresponds to the Carnot limit to the efficiency, which no heat engine can cross. It can be seen in Figure 7.2 that at high temperatures, thermogalvanic devices could perform similarly to a Brayton cycle powered by solar heat input.

This is significant since solar thermal applications were specifically identified for thermogalvanic devices by Osteryoung and Chum in their original report [20]. However, unlike a solar powered Brayton cycle mechanical heat engine, charge storage as well as power generation is possible in a thermogalvanic device. This lowers the complexity, and thus parasitic losses, of the over all system.

In the course of this work, LLZO garnet materials have been identified as a potential material for use as an electrolyte in a thermogalvanic cell due to the unprecedented combination of superionic behavior in a bulk polycrystalline material and electrochemical stability with metallic Li. It has been discussed in this work that LLZO garnet materials also have sufficient mechanical properties to resist Li dendrite penetration. This is significant because dendrite penetration was found to be the primary failure mechanism for other solid TRES devices such as thermogalvanics based on AgI and AMTECs based on Na β ”-alumina. Furthermore, thermogalvanic operation of a LLZO based thermogalvanic cell has been demonstrated for the first time in this work. Finally, a thermogalvanic zT of 1, which is comparable to modern thermoelectric materials, is likely possible at moderate operating temperatures if the improvements to the physical properties proposed here can be realized. Therefore, further explorations are justified to verify the predicted performance. Thermogalvanic devices based on LLZO garnet type solid electrolytes could be the first type of device to offer combined solid-state direct thermal-to-electric energy conversion and storage in a singular device. The elimination of a secondary system to store charge for load matching would significantly reduce the cost of alternative energy conversion systems and help to reduce the

growing problem of climate change.

BIBLIOGRAPHY

BIBLIOGRAPHY

[1] Ahmed F. Ghoniem. Needs, resources and climate change: Clean and efficient conversion technologies. *Progress in Energy and Combustion Science*, 37(1):15–51, February 2011.

[2] Martin Hoffert, Ken Caldeira, Gregory Benford, David R. Criswell, Christopher Green, Howard Herzog, Atul K. Jain, Haroon S. Kheshgi, Klaus S. Lackner, John S. Lewis, H. Douglas Lightfoot, Wallace Manheimer, John C. Mankins, Michael E. Mauel, L. John Perkins, Michael E. Schlesinger, Tyler Volk, and Tom M. L. Wigley. Advanced Technology Paths to Global Climate Stability: Energy for a Greenhouse Planet. *Science*, 298(5595):981–987, May 2014.

[3] G Berry and W Daily. Energy Flowchart Scenarios of Future US Energy Use Incorporating Hydrogen Fueled Vehicles. *2004*, January 2004.

[4] VS Arunachalam and Fleischer. The global energy landscape and materials innovation. *MRS Bulletin*, January 2008.

[5] U. S. Energy Information Administration. Annual Energy Outlook 2014 With Projections to 2040. pages 1–269, May 2014.

[6] J. Potocnik. Renewable Energy Sources and the Realities of Setting an Energy Agenda. *Science*, 315(5813):810–811, February 2007.

[7] G. M. Whitesides and G. W. Crabtree. Don't Forget Long-Term Fundamental Research in Energy. *Science*, 315(5813):796–798, February 2007.

[8] J. Chow, R. J. Kopp, and P. R. Portney. Energy Resources and Global Development. *Science*, 302(5650):1528–1531, November 2003.

[9] C Parmesan and G Yohe. A globally coherent fingerprint of climate change impacts across natural systems. *Nature*, January 2003.

[10] Intergovernmental Panel on Climate Change. Climate Change 2007: The Physical Science Basis, Summary for Policy Makers. *IPCC WGI Fourth Assessment Report*, January 2007.

[11] JR Senft. *Mechanical efficiency of heat engines*. Cambridge University Press, University of Wisconsin–River Falls, January 2007.

[12] MV Volkenstein, A Shenitzer, and RG Burns. *Entropy and information*. Birkhäuser Verlag AG, January 2009.

[13] E. D. Wachsman and K. T. Lee. Lowering the Temperature of Solid Oxide Fuel Cells. *Science*, 334(6058):935–939, November 2011.

[14] GJ Snyder and ES Toberer. Complex thermoelectric materials. *Nature Materials*, January 2008.

[15] JF Li, WS Liu, LD Zhao, and M Zhou. High-performance nanostructured thermoelectric materials. *NPG Asia Materials*, January 2010.

[16] Kanishka Biswas, Jiaqing He, Ivan D. Blum, Chun-I Wu, Timothy P. Hogan, David N. Seidman, Vinayak P. Dravid, and Mercouri G. Kanatzidis. High-performance bulk thermoelectrics with all-scale hierarchical architectures. *Nature*, 489(7416):414–418, September 2012.

[17] JR Sootsman, DY Chung, and MG Kanatzidis. New and Old Concepts in Thermoelectric Materials. *Angewandte Chemie International Edition*, 48(46):8616–8639, November 2009.

[18] A. J. Minnich, M. S. Dresselhaus, Z. F. Ren, and G. Chen. Bulk nanostructured thermoelectric materials: current research and future prospects. *Energy & Environmental Science*, 2(5):466, January 2009.

[19] JP Heremans and B Wiendlocha. Resonant levels in bulk thermoelectric semiconductors. *Energy & Environmental*, January 2012.

[20] HI Chum and RA Osteryoung. Review of thermally regenerative electrochemical systems, volume 2. *Radio Engineering Radio*, January 1981.

[21] O Asakami, K Tsuchida, H Togawa, and A Kato. Material for the electrode of the alkali metal thermoelectric converter (AMTEC). *Journal of Materials Science*, January 1989.

[22] Shuang-Ying Wu, Lan Xiao, and Yi-Ding Cao. A review on advances in alkali metal thermal to electric converters (AMTECs). *International Journal of Energy Research*, 33(10):868–892, August 2009.

[23] RM Williams, ME Loveland, BJ Nakamura, ML Underwood, CP Bankston, H Leduc, and JT Kummer. Kinetics and Transport at AMTEC Electrodes I. The Interfacial Impedance Model. *Journal of the Electrochemical Society*, January 1990.

[24] T Cole. Thermoelectric energy conversion with solid electrolytes. *Science*, January 1983.

[25] TK Hunt, N Weber, and T Cole. High Efficiency Thermoelectric Conversion With Beta"-Alumina Electrolytes, The Sodium Heat Engine. *Solid State Ionics*, 5(OCT):263–266, 1981.

[26] JL Weininger. Thermogalvanic Cells With Silver Iodide As A Solid Electrolyte. *Journal of the Electrochemical Society*, 111(7):769–774, 1964.

[27] K Wada, A Suzuki, H Sato, and R Kikuchi. Soret effect in solids. *of Physics and Chemistry of Solids*, January 1985.

[28] SA Akbar, M Kaburagi, and H Sato. Soret effect in solid - II. *Journal of Physics and Chemistry of Solids*, January 1987.

[29] C Korte, J Janek, and H Timm. Transport processes in temperature gradients - Thermal diffusion and Soret effect in crystalline solids. *Solid State Ionics*, 101:465–470, November 1997.

[30] RW Christy. Electrical Conductivity and Thermoelectric Power in Ionic Crystals. *American Journal of Physics*, January 1960.

[31] C Wagner. The thermoelectric power of cells with ionic compounds involving ionic and electronic conduction. *Progress in Solid State Chemistry*, January 1972.

[32] RW Christy. Thermoelectric power of silver halides. *The Journal of Chemical Physics*, January 1961.

[33] YV Kuzminskii, VA Zasukha, and GY Kuzminskaya. Thermoelectric Effects In Electrochemical Systems - Nonconventional Thermogalvanic Cells. *Journal of Power Sources*, 52(2):231–242, December 1994.

[34] TI Quickenden and Y Mua. A review of power generation in aqueous thermogalvanic cells. *Journal of the Electrochemical Society*, January 1995.

[35] V Zinovyeva, S Nakamae, and M Bonetti. Enhanced Thermoelectric Power in Ionic Liquids. *ChemElectroChem*, 1(2):426–430, February 2014.

[36] Theodore J. Abraham, Douglas R. MacFarlane, and Jennifer M. Pringle. Seebeck coefficients in ionic liquids -prospects for thermo-electrochemical cells. *Chemical Communications*, 47(22):6260, January 2011.

[37] K. D. Sandbakk, A. Bentien, and S. Kjelstrup. Thermoelectric effects in ion conducting membranes and perspectives for thermoelectric energy conversion. *Journal of Membrane Science*, 434:10–17, May 2013.

[38] Nicholas S. Hudak and Glenn G. Amatucci. Energy Harvesting and Storage with Lithium-Ion Thermogalvanic Cells. *Journal of the Electrochemical Society*, 158(5):A572–A579, 2011.

[39] T. Motohashi, E. Naujalis, R. Ueda, K. Isawa, M. Karppinen, and H. Yamauchi. Simultaneously enhanced thermoelectric power and reduced resistivity of $Na_xCo_2O_4$ by controlling Na nonstoichiometry. *Applied Physics Letters*, 79(10):1480, January 2001.

[40] Alan Logéat, Thomas Köhler, Ulrich Eisele, Barbara Stiaszny, Andreas Harzer, Michael Tovar, Anatoliy Senyshyn, Helmut Ehrenberg, and Boris Kozinsky. From order to disorder: The structure of lithium-conducting garnets $Li_{7-x}La_3Ta_xZr_{2-x}O_{12}$ (x=0-2). *Solid State Ionics*, 206:33–38, January 2012.

[41] RA Huggins. Simple method to determine electronic and ionic components of the conductivity in mixed conductors a review. *Ionics*, January 2002.

[42] Ezhiyl Rangasamy, Jeff Wolfenstine, and Jeffrey Sakamoto. The role of Al and Li concentration on the formation of cubic garnet solid electrolyte of nominal composition $Li_7La_3Zr2O_{12}$. *Solid State Ionics*, 206:28–32, January 2012.

[43] Henrik Buschmann, Janis Dölle, Stefan Berendts, Alexander Kuhn, Patrick Bottke, Martin Wilkening, Paul Heitjans, Anatoliy Senyshyn, Helmut Ehrenberg, Andriy Lotnyk, Viola Duppel, Lorenz Kienle, and Jürgen Janek. Structure and dynamics of the fast lithium ion conductor "$Li_7La_3Zr_2O_{12}$". *Physical Chemistry Chemical Physics*, 13(43):19378, January 2011.

[44] Yiqiu Li, Yang Cao, and Xiangxin Guo. Influence of lithium oxide additives on densification and ionic conductivity of garnet-type Li6.75La3Zr1.75Ta0.25O12 solid electrolytes. *Solid State Ionics*, 253:76–80, December 2013.

[45] Travis Thompson, Jeff Wolfenstine, Jan L. Allen, Michelle Johannes, Ashfia Huq, Isabel N. David, and Jeff Sakamoto. Tetragonal vs. cubic phase stability in Al – free Ta doped $Li_7La_3Zr_2O_{12}$ (LLZO). *Journal of Materials Chemistry A*, 2(33):13431, January 2014.

[46] R Murugan, V Thangadurai, and W Weppner. Fast Lithium Ion Conduction in Garnet-Type $Li_7La_3Zr_2O_{12}$. *Angewandte Chemie*, January 2007.

[47] J Bisquert and A Compte. Theory of the electrochemical impedance of anomalous diffusion. *Journal of Electroanalytical Chemistry*, January 2001.

[48] AC Larson and RB Dreele. GSAS. *General Structure Analysis System*, January 1994.

[49] BH Toby. EXPGUI, a graphical user interface for GSAS. *Journal of Applied Crystallography*, January 2001.

[50] G. T. Hitz, E. D. Wachsman, and V. Thangadurai. Highly Li-Stuffed Garnet-Type $Li_{7+x}La_3Zr_{2-x}Y_xO_{12}$. *Journal of the Electrochemical Society*, 160(8):A1248–A1255, April 2013.

[51] Youhao Liao, Preetam Singh, Kyu-Sung Park, Weishan Li, and John B. Goodenough. $Li_6Zr_2O_7$ interstitial lithium-ion solid electrolyte. *Electrochimica acta*, 102:446–450, July 2013.

[52] AD Pelton. The Ag-Li (Silver-Lithium) system. *Bulletin of Alloy Phase Diagrams*, January 1986.

[53] M Ohtaki. Recent aspects of oxide thermoelectric materials for power generation from mid-to-high temperature heat source. *Journal of the Ceramic Society of Japan*, January 2011.

[54] Kunihito Koumoto, Yifeng Wang, Ruizhi Zhang, Atsuko Kosuga, and Ryoji Funahashi. Oxide Thermoelectric Materials: A Nanostructuring Approach. *Annual Review of Materials Research*, 40(1):363–394, June 2010.

[55] Minhyea Lee, Liliana Viciu, Lu Li, Yayu Wang, M. L. Foo, S. Watauchi, R. A. Pascal Jr, R. J. Cava, and N. P. Ong. Large enhancement of the thermopower in NaxCoO2 at high Na doping. *Nature Materials*, 5(7):537–540, June 2006.

[56] I Terasaki, Y Sasago, and K Uchinokura. Large thermoelectric power in $NaCo_2O_4$ single crystals. *Physical Review B*, January 1997.

[57] TY Wei, CH Chen, KH Chang, SY Lu, and CC Hu. Cobalt oxide aerogels of ideal supercapacitive properties prepared with an epoxide synthetic route. *Chemistry of Materials*, January 2009.

[58] AE Gash, TM Tillotson, JH Satcher Jr., LW Hrubesh, and RL Simpson. New sol-gel synthetic route to transition and main-group metal oxide aerogels using inorganic salt precursors. *Journal of Non-Crystalline Solids*, January 2001.

[59] Alexander E. Gash, Joe H. Satcher, and Randall L. Simpson. Monolithic nickel(II)-based aerogels using an organic epoxide: the importance of the counterion. *Journal of Non-Crystalline Solids*, 350:145–151, December 2004.

[60] Sumit Mehrotra, Daniel Lynam, Ryan Maloney, Kendell M. Pawelec, Mark H. Tuszynski, Ilsoon Lee, Christina Chan, and Jeffrey Sakamoto. Time Controlled Protein Release from Layer-by-Layer Assembled Multilayer Functionalized Agarose Hydrogels. *Advanced Functional Materials*, 20(2):247–258, January 2010.

[61] Daniel Lynam, Chelsea Peterson, Ryan Maloney, Dena Shahriari, Alexa Garrison, Sara Saleh, Sumit Mehrotra, Christina Chan, and Jeff Sakamoto. Augmenting protein release from layer-by-layer functionalized agarose hydrogels. *Carbohydrate Polymers*, 103:377–384, March 2014.

[62] H Ohtaki and T Radnai. Structure and dynamics of hydrated ions. *Chemical Reviews*, January 1993.

[63] BW Matthews and SJ Remington. The three dimensional structure of the lysozyme from bacteriophage T4. In *Proceedings of the National*, January 1974.

[64] Mikio Ito and Junji Sumiyoshi. Enhancement of thermoelectric performance of $Na_xCo_2O_4$ with Ag dispersion by precipitation from Ag^+ aqueous solution. *Journal of Sol-Gel Science and Technology*, 55(3):354–359, September 2010.

[65] Mikio Ito and Daisuke Furumoto. Effects of mechanical milling and Ag addition on thermoelectric properties of $Na_xCo_2O_4$. *Scripta Materialia*, 55(6):533–536, September 2006.

[66] Xiaoyuan Zhou, Guoyu Wang, Long Zhang, Hang Chi, Xianli Su, Jeff Sakamoto, and Ctirad Uher. Enhanced thermoelectric properties of Ba-filled skutterudites by grain size reduction and Ag nanoparticle inclusion. *Journal of Materials Chemistry*, 22(7):2958, January 2012.

[67] Hiroo Yamakawa, Soonil Lee, Hiroshi Takagi, and Clive A. Randall. Property-processing relations in developing thermoelectric ceramics: $Na_{1-x}Co_2O_4$. *Journal of Materials Science*, 46(7):2064–2070, April 2011.

[68] Mikio Ito, Tomoya Nagira, Daisuke Furumoto, Yoshimitsu Oda, and Shigeta Hara. Synthesis of $Na_xCo_2O_4$ thermoelectric oxide with crystallographic anisotropy by chemical solution process. *Science and Technology of Advanced Materials*, 5(1-2):125–131, January 2004.

[69] V Rouessac, J Wang, J Provost, and G Desgardin. Processing and superconducting properties of highly textured Bi (Pb)-2223 ceramics by sinter-forging. *Physica C:*, January 1996.

[70] T Minami, M Tatsumisago, M Wakihara, and C Iwakura. *Solid state ionics for batteries*. Springer, January 2005.

[71] J. L. Allen, J. Wolfenstine, E. Rangasamy, and J. Sakamoto. Effect of substitution (Ta, Al, Ga) on the conductivity of $Li_7La_3Zr_2O_{12}$. *Journal of Power Sources*, 206:315–319, May 2012.

[72] David T. Wong, Scott A. Mullin, Vincent S. Battaglia, and Nitash P. Balsara. Relationship between morphology and conductivity of block-copolymer based battery separators. *Journal of Membrane Science*, 394-395:175–183, March 2012.

[73] W. C West, J. F Whitacre, and J. R Lim. Chemical stability enhancement of lithium conducting solid electrolyte plates using sputtered LiPON thin films. *Journal of Power Sources*, 126(1-2):134–138, February 2004.

[74] RD Armstrong, T Dickinson, and J Turner. The breakdown of β-alumina ceramic electrolyte. *Electrochimica acta*, January 1974.

[75] P Arora and Z Zhang. Battery separators. *Chemical Reviews*, January 2004.

[76] Sheng Shui Zhang. A review on the separators of liquid electrolyte Li-ion batteries. *Journal of Power Sources*, 164(1):351–364, January 2007.

[77] Charles Monroe and John Newman. The Impact of Elastic Deformation on Deposition Kinetics at Lithium/Polymer Interfaces. *Journal of the Electrochemical Society*, 152(2):A396, January 2005.

[78] Sergiy Kalnaus, Adrian S. Sabau, Wyatt E. Tenhaeff, Nancy J. Dudney, and Claus Daniel. Design of composite polymer electrolytes for Li ion batteries based on mechanical stability criteria. *Journal of Power Sources*, 201:280–287, March 2012.

[79] DJ Rasky and F Milstein. Pseudopotential theoretical study of the alkali metals under arbitrary pressure: Density, bulk modulus, and shear moduli. *Physical Review B*, January 1986.

[80] Jennifer E. Ni, Eldon D. Case, Jeffrey S. Sakamoto, Ezhiyl Rangasamy, and Jeffrey B. Wolfenstine. Room temperature elastic moduli and Vickers hardness of hot-pressed LLZO cubic garnet. *Journal of Materials Science*, 47(23):7978–7985, December 2012.

[81] Shingo Ohta, Tetsuro Kobayashi, and Takahiko Asaoka. High lithium ionic conductivity in the garnet-type oxide $Li_{7-x}La_3(Zr_{2-x},Nb_x)O_{12}$ (x=0-2). *Journal of Power Sources*, 196(6):3342–3345, March 2011.

[82] Masashi Kotobuki, Hirokazu Munakata, Kiyoshi Kanamura, Yosuke Sato, and Toshihiro Yoshida. Compatibility of $Li_7La_3Zr_2O_{12}$ Solid Electrolyte to All-Solid-State Battery Using Li Metal Anode. *Journal of the Electrochemical Society*, 157(10):A1076, January 2010.

[83] Yuta Shimonishi, Akiharu Toda, Tao Zhang, Atsushi Hirano, Nobuyuki Imanishi, Osamu Yamamoto, and Yasuo Takeda. Synthesis of garnet-type $Li_{7-x}La_3Zr_2O_{12-1/2x}$ and its stability in aqueous solutions. *Solid State Ionics*, 183(1):48–53, February 2011.

[84] V Thangadurai and W Weppner. $Li_6ALa_2Ta_2O_{12}$ (A= Sr, Ba): Novel Garnet-Like Oxides for Fast Lithium Ion Conduction. *Advanced Functional Materials*, January 2005.

[85] Michael P. O'Callaghan, Danny R. Lynham, Edmund J. Cussen, and George Z. Chen. Structure and Ionic-Transport Properties of Lithium-Containing Garnets $Li_3Ln_3Te_2O_{12}$ (Ln = Y, Pr, Nd, Sm-Lu). *Chemistry of Materials*, 18(19):4681–4689, September 2006.

[86] Michael P. O'Callaghan, Andrew S. Powell, Jeremy J. Titman, George Z. Chen, and Edmund J. Cussen. Switching on Fast Lithium Ion Conductivity in Garnets: The Structure and Transport Properties of $Li_{3+x}Nd_3Te_{2-x}Sb_xO_{12}$. *Chemistry of Materials*, 20(6):2360–2369, March 2008.

[87] Edmund J. Cussen and Thomas W. S. Yip. A neutron diffraction study of the d^0 and d^{10} lithium garnets $Li_3Nd_3W_2O_{12}$ and $Li_5La_3Sb_2O_{12}$. *Journal of Solid State Chemistry*, 180(6):1832–1839, June 2007.

[88] Michael P. O'Callaghan and Edmund J. Cussen. The structure of the lithium-rich garnets $Li_6SrLa_2M_2O_{12}$ and $Li_{6.4}Sr_{1.4}La_{1.6}M_2O_{12}$ (M=Sb, Ta). *Solid State Sciences*, 10(4):390–395, April 2008.

[89] K. Saranya, C. Deviannapoorani, L. Dhivya, S. Ramakumar, N. Janani, and Ramaswamy Murugan. $Li_{7-x}La_3Sn_{2-x}Nb_xO_{12}$ (x=0.25 - 1) cubic lithium garnet. *Materials Letters*, 77:57–59, June 2012.

[90] Edmund J. Cussen. The structure of lithium garnets: cation disorder and clustering in a new family of fast Li^+ conductors. *Chemical Communications*, (4):412, January 2006.

[91] Y. Kihira, S. Ohta, H. Imagawa, and T. Asaoka. Effect of Simultaneous Substitution of Alkali Earth Metals and Nb in $Li_7La3Zr_2O_{12}$ on Lithium-Ion Conductivity. *ECS Electrochemistry Letters*, 2(7):A56–A59, April 2013.

[92] Michael P. O'Callaghan and Edmund J. Cussen. Lithium dimer formation in the Li-conducting garnets $Li_{5+x}Ba_xLa_{3-x}Ta_2O_{12}$ (0 . *Chemical Communications*, (20):2048, January 2007.

[93] Torsten Zaiss, Martin Ortner, Ramaswamy Murugan, and Werner Weppner. Fast ionic conduction in cubic hafnium garnet Li7La3Hf2O12. *Ionics*, 16(9):855–858, December 2010.

[94] H Xie, JA Alonso, Y Li, and MT Fernández-Díaz. Lithium Distribution in Aluminum-Free Cubic $Li_7La_3Zr_2O_{12}$. *Chemistry of*, January 2011.

[95] H Hyooma and K Hayashi. Crystal structures of $La_3Li_5M_2$ O_{12} (M = Nb, Ta). *Materials research bulletin*, January 1988.

[96] Venkataraman Thangadurai and Werner Weppner. Li6ALa2Nb2O12 (A=Ca, Sr, Ba): A New Class of Fast Lithium Ion Conductors with Garnet-Like Structure. *Journal of the American Ceramic Society*, 88(2):411–418, February 2005.

[97] V Thangadurai, H Kaack, and WJF Weppner. Novel Fast Lithium Ion Conduction in Garnet-Type $Li5La_3M_2O_{12}$ (M= Nb, Ta). *Journal of the American Ceramics Society*, January 2003.

[98] CA Geiger, E Alekseev, B Lazic, and M Fisch. Crystal chemistry and stability of "$Li_7La_3Zr_2O_{12}$" garnet: a fast lithium-ion conductor. *chemistry*, January 2010.

[99] N Bernstein, MD Johannes, and K Hoang. Origin of the structural phase transition in $Li_7La_3Zr_2O_{12}$. *Physical Review Letters*, January 2012.

[100] J Wolfenstine, E Rangasamy, JL Allen, and J Sakamoto. High conductivity of dense tetragonal $Li_7La_3Zr_2O_{12}$. *Journal of Power Sources*, January 2012.

[101] Yutao Li, Jian-Tao Han, Chang-An Wang, Hui Xie, and John B. Goodenough. Optimizing Li+ conductivity in a garnet framework. *Journal of Materials Chemistry*, 22(30):15357, January 2012.

[102] Jeff Wolfenstine, Joshua Ratchford, Ezhiyl Rangasamy, Jeffrey Sakamoto, and Jan L. Allen. Synthesis and high Li-ion conductivity of Ga-stabilized cubic $Li_7La_3Zr_2O_{12}$. *Materials Chemistry and Physics*, 134(2-3):571–575, June 2012.

[103] Daniel Rettenwander, Charles A. Geiger, and Georg Amthauer. Synthesis and Crystal Chemistry of the Fast Li-Ion Conductor $Li_7La_3Zr_2O_{12}$ Doped with Fe. *Inorganic Chemistry*, 52(14):8005–8009, July 2013.

[104] S Ramakumar, L Satyanarayana, S. V. Manorama, and R. Murugan. Structure and Li+ dynamics of Sb-doped $Li_7La_3Zr_2O_{12}$ fast lithium ion conductors. *Physical Chemistry Chemical Physics*, January 2013.

[105] D Rettenwander, P Blaha, R Laskowski, and C Geiger. DFT Study of the Role of Al^{3+} in the Fast Ion-Conductor Li_{7-3x} $Al^{3+}{}_x$ $La_3Zr_2O_{12}$ Garnet. *Chemistry of Materials*, January 2014.

[106] RD Shannon. Revised effective ionic radii and systematic studies of interatomic distances in halides and chalcogenides. *Acta Crystallographica Section A: Crystal Physics*, January 1976.

[107] F. Tietz, T. Wegener, M. T. Gerhards, M. Giarola, and G. Mariotto. Synthesis and Raman micro-spectroscopy investigation of $Li_7La_3Zr_2O_{12}$. *Solid State Ionics*, 230:77–82, January 2013.

[108] JTS Irvine, DC Sinclair, and AR West. Electroceramics: characterization by impedance spectroscopy. *Advanced Materials*, January 1990.

[109] AK Ivanov-Schitz and J Schoonman. Electrical and interfacial properties of a $Li_3Fe_2(PO_4)_3$ single crystal with silver electrodes. *Solid State Ionics*, January 1996.

[110] Tsang-Tse Fang and C. P. Liu. Evidence of the Internal Domains for Inducing the Anomalously High Dielectric Constant of $CaCu_3Ti_4O_{12}$. *Chemistry of Materials*, 17(20):5167–5171, October 2005.

[111] J. B. Goodenough. Review Lecture: Fast Ionic Conduction in Solids. *Proceedings of the Royal Society A: Mathematical, Physical and Engineering Sciences*, 393(1805):215–234, June 1984.

[112] R Inada, K Kusakabe, T Tanaka, S Kudo, and Y Sakurai. Synthesis and properties of Al-free $Li_{7-x}La_3Zr_{2-x}Ta_xO_{12}$ garnet related oxides. *Solid State Ionics*, January 2013.

[113] McCusker, L. B. McCusker, L.B., Von von Dreele, R.B., Cox, D.E., Louer, D., Scardi, P., R. B. von Dreele, D. E. Cox, D. Louër, and P. Scardi. Rietveld refinement guidelines. *Journal of Applied Crystallography*, 32(1):36–50, February 1999.

[114] Y Wang and W Lai. High Ionic Conductivity Lithium Garnet Oxides of $Li_{7-x}La_3Zr_{2-x}Ta_xO_{12}$ Compositions. *Electrochemical and Solid-State Letters*, January 2012.

[115] Aude A. Hubaud, David J. Schroeder, Baris Key, Brian J. Ingram, Fulya Dogan, and John T. Vaughey. Low temperature stabilization of cubic $(Li_{7-x}Al_{x/3})La_3Zr_2O_{12}$: role of aluminum during formation. *Journal of Materials Chemistry A*, 1(31):8813, January 2013.

[116] Junji Awaka, Akira Takashima, Kunimitsu Kataoka, Norihito Kijima, Yasushi Idemoto, and Junji Akimoto. Crystal Structure of Fast Lithium-ion-conducting Cubic $Li_7La_3Zr_2O_{12}$. *Chemistry Letters*, 40(1):60–62, January 2011.

[117] Ming Xu, Min Sik Park, Jae Myung Lee, Tae Young Kim, Young Sin Park, and Evan Ma. Mechanisms of Li^+ transport in garnet-type cubic $Li_{3+x}La_3M_2O_{12}$ (M = Te, Nb, Zr). *Physical Review B*, 85(5), February 2012.

[118] Leo van Wullen, Thomas Echelmeyer, Hinrich-Wilhelm Meyer, and Dirk Wilmer. The mechanism of Li-ion transport in the garnet Li5La3Nb2O12. *Physical Chemistry Chemical Physics*, 9(25):3298, January 2007.

[119] CHJ Stuhrmann, H Kreiterling, and K Funke. Ionic Hall effect measured in rubidium silver iodide. *Solid State Ionics*, January 2002.

[120] YJ Liou, RA Hudson, SK Wonnell, and LM Slifkin. Ionic Hall effect in crystals: Independent versus cooperative hopping in AgBr and α-AgI. *Physical Review B*, January 1990.

[121] Hiroshi Nozaki, Masashi Harada, Shingo Ohta, Isao Watanabe, Yasuhiro Miyake, Yutaka Ikedo, Niina H. Jalarvo, Eugene Mamontov, and Jun Sugiyama. Li diffusive behavior of garnet-type oxides studied by muon-spin relaxation and QENS. *Solid State Ionics*, November 2013.

[122] ACM Rodrigues and MLF Nascimento. Charge carrier mobility and concentration as a function of composition in $AgPO_3$ - AgI glasses. *The Journal of Chemical Physics*, January 2011.

[123] V Clement, D Ravaine, C Déportes, and R Billat. Measurement of Hall mobilites in $AgPO_3$-AgI glasses. *Solid State Ionics*, January 1988.

[124] Randy Jalem, Yoshihiro Yamamoto, Hiromasa Shiiba, Masanobu Nakayama, Hirokazu Munakata, Toshihiro Kasuga, and Kiyoshi Kanamura. Concerted Migration Mechanism in the Li Ion Dynamics of Garnet - Type $Li_7La_3Zr_2O_{12}$. *Chemistry of Materials*, 25(3):425–430, February 2013.

[125] Katharina Meier, Teodoro Laino, and Alessandro Curioni. Solid-State Electrolytes: Revealing the Mechanisms of Li-Ion Conduction in Tetragonal and Cubic LLZO by First-Principles Calculations. *The Journal of Physical Chemistry C*, 118(13):6668–6679, April 2014.

[126] Sabah K. Bux, Richard G. Blair, Pawan K. Gogna, Hohyun Lee, Gang Chen, Mildred S. Dresselhaus, Richard B. Kaner, and Jean-Pierre Fleurial. Nanostructured Bulk Silicon as an Effective Thermoelectric Material. *Advanced Functional Materials*, 19(15):2445–2452, August 2009.

[127] CB Vining. An inconvenient truth about thermoelectrics. *Nature Materials*, January 2009.